

QUANTUM DEGENERATE GASES NEAR A FESHBACH RESONANCE

A Dissertation

Presented to the Faculty of the Graduate School

of Cornell University

in Partial Fulfillment of the Requirements for the Degree of

Doctor of Philosophy

by

Sourish Basu

August 2009

© 2009 Sourish Basu
ALL RIGHTS RESERVED

QUANTUM DEGENERATE GASES NEAR A FESHBACH RESONANCE

Sourish Basu, Ph.D.

Cornell University 2009

This doctoral dissertation is concerned with the physics of strongly interacting cold alkali atoms at low temperatures near a Feshbach resonance. In **Chapter 1**, we establish a connection between superfluid ^4He and the BCS theory of superconductivity, and cold alkali atoms. We give the history of cold atoms, describing the significant achievements, pitfalls and challenges.

In **Chapter 2**, we explore the thermodynamics of strongly interacting Bosonic atoms. We explore the stability of atomic Bosonic condensates near a Feshbach resonance. We show that the experimentally attained atomic condensate is a saddle point of the free energy, but the kinetics of its decay is slow. We also show that there is a second, higher density condensate branch which has an Ising-like phase transition to a molecular (paired) condensate when ramped across the Feshbach resonance. We argue that due to the high density, inelastic 3-body processes possibly render this transition unobservable.

In **Chapter 3**, we explore the thermodynamics of Fermionic atoms near a Feshbach resonance. We determine the zero-temperature ($T \ll T_F$) pair propagator for a spin-imbalanced mixture of up and down spin Fermions, and use it to show that such a mixture becomes completely polarized at $\mu_{\downarrow} = -0.9\mu_{\uparrow}$. We also determine the Thouless criterion for superfluidity in a spin-imbalanced Fermi mixture, and construct a phase diagram of such a system at zero temperature. We then compare our results with experiments performed by two different groups. We find that interaction modifications to the minority spin self-energy inferred from our analysis is roughly double those observed in experiments. This discrepancy is consistent with the expected accuracy of the theory.

In **Chapter 4**, we extend our analysis of the preceding chapter to calculate the surface tension of an interface between spin-polarized Fermions in the normal and superfluid phases. We show that, as expected, this surface tension decreases with increasing temperature and vanishes at a tricritical temperature, above which the transition becomes continuous. We also calculate the thickness of the interface; at $T = 0$, this is a few interparticle spacings, but diverges at the tricritical temperature. To compare with a set of relevant experiments, we also develop a phenomenological model for surface tension, and conclude that experimental surface tensions are an order of magnitude higher than what our microscopic calculation yields. We hypothesize possible mechanisms.

In **Chapter 5**, we calculate the finite temperature phase diagram of a Bose-Fermi mixture produced from a spin-imbalanced two-component Fermi gas deep in the BEC phase. We show that there is a discontinuous transition between the superfluid and normal phase, with an entropy of mixing sufficient to cool the system down. We detail the construction of such a cooling scheme to cool a Fermi system below what is possible evaporatively, and find that the cooling efficiency is comparable to typical evaporative schemes.

In **Chapter 6**, we shift our focus from thermodynamics to dynamics. We calculate shifts in the energy spectrum of a spin-balanced Fermionic superfluid of Cooper pairs due to the presence of energetically close states coupled by a Feshbach resonance. These shifts manifest themselves as clock-shifts in the radio-frequency spectrum of the superfluid. In addition to a broad asymmetric peak coming from the break-up of Cooper pairs, we find (for certain parameter ranges) a sharp, symmetric “bound-bound” spectral line coming from the conversion of Cooper pairs in one channel to pairs or molecules in another channel. Our theory shows remarkable quantitative agreement with experiments performed by an experimental group.

BIOGRAPHICAL SKETCH

Sourish Basu was born to Amar Nath and Sumitra Basu on 10th September, 1980. Growing up in a house heavy with the musty smell of old books, he spent a significant portion of his childhood in the attic with his nose buried¹ in yellowed, moth-eaten, termite-ridden publications which he wasn't allowed to bring down for fear of infecting the non-decrepit volumes downstairs. Quite naturally, most of his worldly knowledge was derived from a combination of various Gold Key comics (which these days go by the fancier name of "graphic novels"), Arthur Conan Doyle, pre-WWI atlases and The Eagle Annual (the last issue came out in 1992). His present predilection for science stems partly from trying out various experiments from 19th century chemistry textbooks in his mom's kitchen (much to her chagrin, and yes, sometimes with messy results).

Growing up in a typical middle class family in India, the importance of academic achievement was drilled into his head at a very early age. This made him a diligent student in school, although he remembers being rather bored by it.² His parents were OK with him doing anything else so long as he maintained his grades, so he felt no guilt in hiding under the bed with a Russian fairy tale during his study hours.³ Sourish remembers his school years chiefly because of the close friends he made; he still maintains regular contact with some of them. It was also around this time that his allegiance switched from chemistry to physics, thanks largely to a set of "Physics for Everyone" books⁴ by L.D. Landau and A.I. Kitaigorodsky, given to him by his brother.

¹Literally. Even today, one of the first things Sourish does with a new book is to smell the pages, sometime surreptitiously.

²in particular, by Mathematics. He remembers receiving dismal grades, often because he didn't see the point of multiplying five digit numbers or finding square roots by hand, and therefore made up most of the answers. It wasn't until high school that he started enjoying mathematics, for which he freely credits his teachers Dipankar Sarkar and Pinaki Mitra, the latter possibly the best teacher he's had. Ever.

³Unlike typical American households, he didn't have a room of his own.

⁴Since the United States was Pakistan's sugar daddy at the time, India had allied with the U.S.S.R., and the Soviets used to supply India with really, really cheap Russian books.

Fast forward four years, and Sourish was off to study applied physics at the Indian Institute of Technology (IIT), Bombay.⁵ In college, besides learning physics, mathematics and electrical engineering, he also dabbled in acting and writing. One of his fondest memories from college involves staying up nights with a couple of friends, writing two-hours plays for a Performing Arts Festival.

In hindsight, he's not sure why he came to Cornell University for his Ph.D. He had wanted to go to University of Chicago, had received a handsome two-year fellowship, and had almost accepted it (he was about to mail in his acceptance). Then late one night in the computer lab, two of his friends – who had been accepted by Cornell – told him “forget Chicago, come with us to Cornell, we'll have fun.” And he came to Cornell.

Sourish often thinks that if he'd stuck to physics for the most part of his stay at Ithaca, he would have finished at least a year earlier. But he didn't, and thanks his friends, his university, and his adviser profusely for it.⁶ Instead, he took classes in photography, Spanish, science writing, wines, and regrets that he did not have time to take a course in cooking. Thanks to Ithaca's centrally isolated location, he also took up biking, backpacking and Nordic skiing. On his way out, he thinks that he'll probably miss *Gimme! Coffee* more than his office in Clark Hall.

While writing for the *Scientific American* during the summer of 2007, Sourish picked up an interest in climate modeling. That interest eventually led him to Utrecht, where he's going to incorporate satellite data from GOSAT into carbon cycle models for the Netherlands Space Agency. He's looking forward to wearing clogs and shoving raw Herring down his throat, while doing a bit of science in his spare time.

⁵He's quite sure that had he graduated high school a year later, he would have chosen to study mathematics instead. As it happens, the Indian Statistical Institute started their Bachelor of Mathematics program the year after he went off to IIT.

⁶When he wanted his adviser's permission (i.e., signature) to take a photography class, all his adviser said was “try not to inhale a lot of chemical fumes.” For the Spanish classes, he was told, “I think that's a useful language to learn.”

ACKNOWLEDGEMENTS

The ability to reduce everything to simple fundamental laws does not imply the ability to start from those laws and reconstruct the universe... The constructionist hypothesis breaks down when confronted with the twin difficulties of scale and complexity. At each level of complexity entirely new properties appear. Psychology is not applied biology, nor is biology applied chemistry. We can now see that the whole becomes not merely more, but very different from the sum of its parts.

— P.W. Anderson, *More is Different* [1]

Writing an acknowledgement is always ambiguous. It would be easy to thank everyone who has taught me physics during my six years at Cornell, and perhaps that's the thing to do in a Ph.D. thesis. But after six years of graduate school, I'm different from and not more than the sum of however much I've taken from others, and whatever, if anything, I've given to them. I should, therefore, try to acknowledge everyone who has lent a hand in crafting me – not just as a physicist, but as a person. And that is a much harder job.

First things first. I can hardly thank my adviser, Erich Mueller, enough. He has infinite patience, and has indulged my forays into all things outside physics with enthusiastic encouragement.⁷ He has also taught me that the only way of doing physics – indeed, any science – is by going to the board. Thanks mostly to him, I have learned never to assume that I know something unless I can, so to speak, do it on the board.⁸

I would also like to thank several other faculty members at Cornell: Piet Brouwer, Christopher Henley and James Sethna for teaching me how to think about physics, Vinay Ambegaokar for giving me things to think about when the moon is full (in his own words), Natalie Mahowald for encouraging me to take up climate science, Tarleton Gillespie for making me think about information and intellectual property, and Steve Mutkoski

⁷Told about my plan to go off on a science writing fellowship one summer, he said “Certainly. What kind of a life would it be if you couldn't take three months off to decide whether you liked what you're considering doing for the rest of your life?”

⁸He's also responsible for my fascination with Scotch whisky, but that's another story.

for infecting me with the wine bug. I especially want to thank Mukund Vengalattore for teaching me about experimental realities; having overlapped with him for only one semester, I wish he had come to our department sooner (or that I had come later). I would like to thank Randall Hulet's group at Rice University for sharing their experimental data with me, and John Shumway (Arizona State University) and Nikolai Prokof'ev (University of Massachusetts at Amherst) for many fruitful discussions. If I do not mention many others, it is only to avoid turning this into a faculty roster. Names aside, the one common feature that has characterized all professors I've met here has been their approachability. I hope wherever I go, I can knock on a door and walk in with a question, just like I could at Cornell.

Happy as I am to graduate, I'm also sad to leave the many excellent friends – both inside and outside the physics department – with whom I'm afraid I won't have frequent contact hereafter. I'm grateful to Saikat Ghosh for putting me up when I first came to the United States, and putting up with me ever since; he gave me the best introduction to a foreign country and culture I could ever hope for. I'm thankful to Jörn Kupferschmidt for many thought-provoking conversations – on economics, politics, ethics, physics, movies, literature, food, drinks – sometimes accompanied by the last two. I'm indebted to Kaden Hazzard for freely sharing with me his holistic view of physics, something I always admired in him and lacked myself.

I should also thank Ari Epstein and Rima Shamieh for many memorable moments both indoors and outdoors; Leslie Ackerman and Sarah Iams for teaching me to ski; Peggy Renwick and Ben Currens for taking me into caves; my housemate Akshay Kulkarni for putting up with me and my whims for six years; Jane Earl, Julie Nucci and Alexa Sabanagh for showing me the joys of science outreach; Steve Hicks for teaching me \LaTeX ; Jahan Dawlaty for hanging out with me and “bullshitting” for many, many hours; Ivan Daykov for sharing with me his tips on computer administration, movies, food and alco-

hol; Daniel Freedman for involving me in a number of things (and being confident that I could actually do those); Henry Hansteen for being a better landlord than anyone should expect (I know, that one doesn't get into a thesis very often); and René Hill for relentlessly asking me “but what is your physics good for?”

I would like to also thank, in no particular order, Stefan Baur, Shaffique Adam, Stephan Braig, Faisal Ahmed, Amar Bhagwat, Matt Stillerman, Sharvari Nadkarni, Paul Grabowski, Jennifer Salwen, Carlos Guerrero Bosagna, Arend van der Zande, Christian Villagra, Ben Arthur, Simon Gravel, Donald Barry, Kara Pivarski, Karen Slovin, Krista Kauppinen, Hasan Padamsee, Sophie Rittner, Thomas Dimiduk, Alex Barron, Svetoslav Dimov, Peter Onyisi, Pietrantonio Costrini, Amgad Squires, Denise di Capua, Nazmuz Jahangir and Josh Braun.

I am lucky to have made a few friends during my childhood who have stayed with me even today, and who are at the same time brutally critical and blindly supportive of anything I do. I am forever grateful to Ishani Roy for being my conscience and (unpaid) counselor, and for pulling me out of many a blue mood; to Pratyush Banerjee for picking up the threads as if we talked just yesterday, every time I go back to India; Jaydip Sen for a good deal of pragmatic advice and having more faith in me than I do myself; Vikram Pakrashi for teaching me not to take myself too seriously; and Bidisha Ghosal for understanding me intuitively, despite being scared of me on day one (or so she says).

For kindling my interest in science communication and keeping it alive, I would like to thank Nevjinder Singhota at CCMR; Stacey Pasco at AAAS; Philip Yam, Steve Ashley and Lisa Stein at Scientific American; Abby Vogel and Pender McCarter of IEEE-USA; Emilie Lorditch at AIP; and Bruce Lewenstein at Cornell University.

No good department can function without its staff, and LASSP and the physics department has an very efficient and friendly team. I'm grateful to Lisa Margosian for convincing me that Cornell would be a good place to come to, and to Deb Hatfield, Douglas

Milton, Judy Wilson, Larissa Vygran and Connie Wright for keeping up that image.

Thanks are also due to my long-suffering parents, who were always more surprised than happy when, on rare occasions, I did remember to call home timely, i.e., without driving them to the brink of desperation. I'm grateful that they've accepted my decisions and choices without too many questions. I would also like to thank my brother for bailing me out of trouble when I was a kid (and trying to do that even now).

If I have neglected to mention someone here who I should have mentioned, I plead guilty of being under the pressure of writing a thesis; a faulty memory and lack of time may be read in such omissions, but never malice.

Lastly, throughout my Ph.D., I was supported by a number of grants. NSF grants PHY-0456261 and PHY-0758104 supported the works in chapters 2, 3, 4 and 6. In addition, chapter 2 was supported by CCMR grant DMR-0079992, and chapter 4 was supported by the Alfred P. Sloan foundation.

TABLE OF CONTENTS

Biographical Sketch	iii
Acknowledgements	v
Table of Contents	ix
List of Tables	xi
List of Figures	xii
1 Introduction	1
1.1 The story of ultracold atoms	4
1.1.1 Bose condensates	5
1.1.2 Degenerate Fermi gases	10
1.1.3 BEC-BCS crossover	15
1.1.4 Future directions and parallels with other systems	22
2 Thermodynamics of Bose condensates near a Feshbach resonance	24
2.1 Phase diagram	26
2.2 Stationary States (fixed density)	30
2.3 Effect of non-zero λ_m and λ_{am}	33
2.4 Stationary States (fixed chemical potential)	34
2.5 Discussion	36
3 Equation of state of spin-polarized Fermions	38
3.1 Introduction	38
3.2 Formulation of the free energy	39
3.3 Calculating the scattering matrix	40
3.4 Calculating the self energies	42
3.5 Calculating the $T = 0$ free energy	43
3.6 Concluding remarks	46
4 Surface tension at a superfluid-normal interface	48
4.1 Introduction	48
4.2 Experimental data	49
4.3 Phenomenological model	50
4.4 Microscopic theory	56
5 A “dilution fridge” of cold atomic vapors	61
5.1 Motivation	61
5.2 Phase diagram	64
5.2.1 Zero temperature	67
5.2.2 Finite temperature	67
5.3 Latent heat	68
5.4 Cooling efficiency	71
5.5 Cooling geometry	73
5.5.1 Background loss	77

5.5.2	Three-body collisions	77
5.5.3	Two-body collisions	78
6	Final-state effects in the RF spectrum of strongly interacting fermions	79
6.1	Introduction	81
6.2	The model	82
6.3	Spectral density	85
6.4	Quantitative accuracy	89
A	Evaluation of the phenomenological free energy	92
B	BCS theory	94
C	The Hubbard-Stratonovich transformation	97
D	Cooling and trapping of atoms	100
D.1	Laser cooling	100
D.1.1	Magneto-optic trapping	102
D.1.2	Temperature limits	104
D.2	Evaporative cooling	105
E	Partial derivatives at constant pressure	109
E.1	A general “chain rule”	109
E.2	Latent heat	109
E.3	Specific heat	113
F	“Steady-state” pumping rate from a trap center	115
G	Feshbach resonance	118
G.1	Scattering theory	120
G.2	Effect of a magnetic field	122
H	Evaluation of the self energy	125
	Bibliography	139

LIST OF TABLES

6.1	Final state interactions for different initial pairs	89
-----	--	----

LIST OF FIGURES

1.1	Cloud energy as a function of cloud radius	7
1.2	Onset of Pauli blocking (schematic)	14
1.3	Onset of phase separation	20
1.4	BEC-BCS crossover	22
2.1	Phase diagrams for the ASF-MSF transition in terms of the binding energy, chemical potential and density	27
2.2	Scaled energy versus molecular condensate order parameter	31
2.3	Stationary points of energy as a function of chemical potential	35
3.1	Self energies as functions of $k_F^\downarrow/k_F^\uparrow$	42
3.2	Free energy of interacting superfluid and normal phases	44
3.3	Free energy of non-interacting superfluid and normal phases	45
3.4	Compressibility vs polarization	46
4.1	High polarization data from Rice[2]	49
4.2	Low polarization data from Rice[2]	50
4.3	Experimental two-dimensional particle densities with theoretical boundaries	53
4.4	χ^2 fitting to determine η	54
4.5	Axial particle densities with theoretical predictions	55
4.6	Width of domain wall as a function of temperature	58
4.7	Surface tension as a function of temperature	59
5.1	^3He - ^4He phase diagram and dilution refrigerator	62
5.2	Phase diagram of a spin-polarized fermi gas[3]	63
5.3	$T = 0$ bose-fermi phase diagram	68
5.4	$T > 0$ bose-fermi phase diagram	69
5.5	Latent heat per particle	70
5.6	Cooling efficiency	72
5.7	Pumping scheme for a dilution refrigerator	73
6.1	Phase space for a bound-bound transition	84
6.2	Emergence of a bound-bound transition	85
6.3	Spectral density as a function of detuning and scattering lengths	88
6.4	Spectral weight in the bound-bound peak	89
6.5	Peak-continuum separation from theory and experiment	90
B.1	The BCS phase transition	96
D.1	Doppler cooling: energetics	101
D.2	Doppler cooling: geometry	101
D.3	Schematic of a MOT in 1-D	103
D.4	Evaporative cooling: energetics	106

F.1	Depleted density profile	115
F.2	Recovering density profile	117
G.1	Feshbach resonance	118
H.1	Matsubara sums to contour integrals	126
H.2	Original contour for evaluating self energy	127
H.3	Modified contour for evaluating self energy	127

CHAPTER 1

INTRODUCTION

It's not everyday that you see a new state of matter. While we can be reasonably certain that people were aware of the three classical states of matter – solid, liquid and gas – several thousand years ago, it wasn't until 1879 that the fourth phase – plasma – was identified by William Crookes in his now-famous vacuum tube. Why did plasma have to wait so long to be discovered, despite being the most common phase of matter in the universe [4]? Quite simply, the earth is just too cold, and Thales could never produce a strong enough electric field with his fur and amber to produce plasma.¹ So man had to wait many centuries before he had the technology to generate thousands of volts in the laboratory and see a plasma.

If the earth is too cold to see swirling tongues of plasma all around us,² could it also be too warm to see a few other phases of matter? Yes, said London and Tisza in 1937 [5], in tying the strange properties of superfluid ^4He to Bose and Einstein's statistics for integral-spin particles [6]. Liquid ^4He , cooled below 2.17 K, transforms into a new (fifth?) phase of matter – a so-called Bose condensate – with unusual properties such as zero viscosity, infinite thermal conductivity, and propagating temperature waves.³

¹There was plasma on earth, of course, and quite visible, too; but the mysteries of lightning and St. Elmo's fire could only be deciphered *after* Crooke's experiment.

²The temperature at which hydrogen is completely ionized into plasma, for example, is about 200,000 K, unheard of on earth, but completely commonplace in the solar corona.

³In this context, I'm reminded of one of Wolfgang Ketterle's stories on how he explains his work to kindergarten kids.

"Suppose you were all living on the sun. Since everything on the sun is gaseous," he explains (omitting the plasma for the kids' benefit), "you, your friends and your family would all be made of gas. In fact, you wouldn't even know that solids or liquids even existed! Now say one of you got real smart, and built a refrigerator. You took some of the gas around you and stuck it into the fridge. If your fridge was good, some time later you'd open the fridge and find – lo and behold – a liquid! Now, if you'd built a *really* good fridge, after some more time, you'd see a solid! So just by building a good fridge, you'd discover matter in new forms that you had never seen before because you lived in a warm place. I do something very similar; I build really good fridges, stick some things in, and watch them change into newer forms of matter which we can't see around us simply because the earth is too warm!"

"Inevitably," he says, "one of them asks, 'If you live on the sun, don't you have to wear a lot of sunscreen?'"

While liquid ^4He provided the earliest example of a Bose condensate, it was quite far from an ideal Bose gas. Interactions between ^4He atoms were quite strong (it was, after all, a liquid), to the point where many physicists – including such giants as Lev Landau and George Uhlenbeck – were not convinced that the phenomenon observed in ^4He was really Bose condensation [7]. Contrary to what happens in a noninteracting Bose gas, a finite fraction of atoms were non-condensed even at $T = 0$, an interaction effect we today call “condensate depletion.” Most importantly, the superfluid density from Landau’s two-fluid model of ^4He is not equal to the condensate density, which itself is only about 10% of the Boson density [8]. For all these reasons, even as early as the 1950s, there was considerable interest in producing an “ideal” Bose gas at low temperatures.

To bridge the gap between BEC in an ideal Bose gas and superfluidity in ^4He , Bogoliubov attacked the problem of excitations in an interacting Bose condensate [9]. He showed that BEC was not significantly altered by weak interactions in a dilute Bose gas, and derived the long-wavelength phonon spectrum that was *assumed* by Landau to explain dissipationless flow within his two-fluid model [10]. When Bardeen, Cooper and Schrieffer used Bogoliubov’s formulation to explain dissipationless flow of electric current in conventional superconductors as well [11], scientists realized that superconductivity in metals was somehow the result of a Bose condensation [12]. Over the next 25 years, it became clear that the BCS theory of superconductivity really involved a “BEC of Cooper pairs” [13]; two (Fermionic) electrons formed a (Bosonic) Cooper pair, which made up a dilute non-overlapping Bose gas. A Bose condensation of this gas below its critical temperature resulted in the superflow of (charged) Cooper pairs, and hence in resistance-less conduction [14].

Since physicists were already thinking of ways to produce an ideal Bose gas, it was natural to ask whether an “ideal” composite Bose gas made up of Fermions could be pro-

duced as well. Such an idea was alluring for quite a few reasons. First, while Cooper pairing between two Fermions did not require them to be charged,⁴ the only Cooper pairing known for a long time was between two electrons. Thus, there was some interest in producing Cooper pairs out of neutral Fermions, to study them without the added complication of charge.⁵ Secondly, scientists realized in 1965 that while the original BCS theory only considered pairs with zero total momentum because of phase space arguments, in theory pairs with a finite total momentum were also possible [17, 18]. Such pairs could be formed as a consequence of mismatched Fermi surfaces between up and down spins, i.e., different densities of the two spins. In conventional superconductors, the Meissner effect forbids such a mismatch in superconductors – yet another consequence of electronic charge. Once scientists had succeeded in producing a Bose gas of composite neutral fermions, it was natural to try to explore the physics posited by [17] and [18] by creating a Cooper paired Bose gas out of mismatched fermions. Thirdly, and perhaps most importantly, both for interacting Bosons as well as interacting Fermions, the interaction strengths were not tunable. Interaction effects for liquid ^4He were fixed by its atomic parameters, and the “pairing potential” between electrons could only be varied over small ranges by changing, for example, dopant concentration.

With the successful production of a BEC from an “ideal” Bose gas in 1995 [19–21], and later, the Bose condensation of Fermion pairs with tunable interaction strength [22, 23], cold atomic vapors have opened up new possibilities along each of those lines. Moreover, they have presented us with an extremely malleable experimental system that can mimic a wide variety of interacting Hamiltonians, providing parallels to many traditional condensed-matter systems [24].

⁴In fact, electrons being charged made it harder for them to pair up, requiring lattice-mediated attraction that only won over Coulombic repulsion at low temperatures.

⁵This was realized in 1972 with the discovery of superfluid ^3He [15, 16], although the pairing (p-wave) had a different symmetry than electron-electron (s-wave) pairing in a conventional superconductor.

This thesis is a rather sparse sampling of everything that is interesting about cold atomic vapors. In chapters 2 to 5, we'll mostly be concerned with the thermodynamic properties of cold atoms; bosons near a Feshbach resonance will be covered in chapter 2, while fermions near a Feshbach resonance will be discussed in chapters 3 and 4. The thermodynamics of Bose-Fermi mixtures will be the subject of chapter 5. Chapter 6, the last chapter, will calculate a dynamic property of fermions near a Feshbach resonance, namely their radio-frequency spectrum.

What will not be covered in this thesis is at least as interesting as what will be, and it would be unfair not to tell the reader what they would be missing out on, and why this field has generated so much interest over the past decade and half. While a practitioner of cold atomic physics should be able to jump to the next chapter without any difficulty, an interested outsider might find the story of ultracold atoms fascinating. The rest of this chapter tries to summarize the history and excitement of this “revolution that has not stopped” [25].

A good part of that revolution has been made possible by advances in techniques for trapping and cooling atoms. This thesis is not about those techniques, and there are many excellent texts such as [26] on the subject. However, for the sake of completeness, we've briefly summarized a few common cooling and trapping techniques in appendix D.

1.1 The story of ultracold atoms

Our story has its beginning in the 1980s, with most of the chapters being added over the last fourteen years. A familiarity with this story is not necessary for following the rest of the thesis, but may embed the remaining chapters in their proper contexts. With the aid of copious footnotes, we'll try to indicate the relevance of those chapters at appropriate

points during the narrative.

1.1.1 Bose condensates

Bose condensation is a consequence of Bose-Einstein statistics. At a temperature T , the total number of (ideal) Bosons in a uniform system of volume V is

$$\begin{aligned}
 N &= \sum_{\mathbf{k}} \frac{1}{e^{\beta(\epsilon_{\mathbf{k}} - \mu)} - 1} \\
 \Rightarrow n &= \frac{1}{2\pi^2} \int_0^\infty \frac{k^2 dk}{e^{\beta(\hbar^2 k^2/2m - \mu)} - 1} \\
 &= \frac{1}{4\pi^2} \left(\frac{2m}{\hbar^2} \right)^{3/2} \int_0^\infty \frac{\epsilon^{1/2} d\epsilon}{e^{\beta(\epsilon - \mu)} - 1} = \int_0^\infty \frac{g(\epsilon) d\epsilon}{e^{\beta(\epsilon - \mu)} - 1}
 \end{aligned} \tag{1.1}$$

where $g(\epsilon) \propto \epsilon^{1/2}$ is the density of states per unit volume at energy ϵ in three dimensions. The integral above is finite for $\mu \leq 0$, and increases as $\mu \rightarrow 0^-$. So it seems that the density of bosons in three dimensions is limited by the value of the above integral for $\mu = 0$. Bose condensation offers a way out of such an unphysical quandry; the above integral gives the density of *uncondensed* Bosons, while the $\epsilon = 0$ (or $\mathbf{k} = 0$) state is occupied by a finite density of particles n_0 . Mathematically, after μ hits zero,

$$\begin{aligned}
 n &= n_0 + \frac{1}{4\pi^2} \left(\frac{2m}{\hbar^2} \right)^{3/2} \int_0^\infty \frac{\epsilon^{1/2} d\epsilon}{e^{\beta\epsilon} - 1} = n_0 + \zeta(3/2) \left[\frac{mk_B T}{2\pi\hbar^2} \right]^{3/2} \\
 \Rightarrow \frac{n_0}{n} &= 1 - \left[\frac{T}{T_{\text{BEC}}} \right]^{3/2}
 \end{aligned} \tag{1.2}$$

where $T_{\text{BEC}} = (2\pi\hbar^2/mk_B)[n/\zeta(3/2)]^{2/3}$. In words, as T drops below T_{BEC} the lowest energy state is occupied by a macroscopic number of particles.⁶ In terms of the phase space density $n\lambda_T^3$, where $\lambda_T = (2\pi\hbar^2/mk_B T)^{1/2}$ is the thermal de Broglie wavelength, Bose-Einstein condensation happens when $n\lambda_T^3$ becomes of order unity⁷ ($n\lambda_{T_{\text{BEC}}}^3 = \zeta(3/2)$), to

⁶It's interesting to note that while interactions in ^4He deplete the condensate fraction to 10% even at $T = 0$, the superfluid transition temperature of 2.17 K is quite close to $T_{\text{BEC}} = 3.87$ K predicted from this formula for non-interacting Bosons.

⁷It's noteworthy that a consequence of (1.1) is that a homogenous 1D ($g(\epsilon) \propto \epsilon^{-1/2}$) or 2D ($g(\epsilon) \propto \epsilon^0$) system cannot Bose condense, because the energy integral in (1.1) is divergent at $\mu = 0$ (which is to say

be exact). Since λ_T is the length scale over which a particle is spatially “spread out” due to the uncertainty principle, $n\lambda_T^3 \sim 1$ is the density at which bosons become “aware” of neighboring bosons, qualitatively speaking.

For early experimentalists on the quest for an ideal Bose gas, it was quite logical to choose the lightest Bosonic atom, ^1H , to maximize T_{BEC} . Unfortunately, hydrogen proved to be a rather unwilling candidate for Bose condensation [27], and only deigned to condense after more than 20 years of concerted effort at MIT and elsewhere [28]. Meanwhile, alkali atoms emerged as strong contenders for Bose-Einstein condensation, thanks to the new technique of laser cooling [29–31].

As detailed in appendix D, atoms in the path of two red-detuned counterpropagating lasers can be cooled down to μK temperatures due to photon recoil. This technique, which required the atoms to have fairly well-separated, clean spectral lines in the optical wavelengths, was ideally suited for alkali atoms because of their sharp $n\text{S} \rightarrow n+1\text{P}$ lines.⁸ The final stage of cooling to achieve $n\lambda_T^3 \sim 1$ is evaporative, expelling the more energetic atoms and allowing the rest of them to thermalize (see appendix D.2 for a discussion).

Thermalization is achieved by interparticle interaction, which has qualitative effects even in a weakly interacting gas, for example in fixing the size of a Bose-condensed cloud in a trap. A bosonic cloud of size R in a harmonic trap will in general have three contributions to its energy per particle, (i) the kinetic energy $K \propto 1/R^2$, (ii) the interaction energy $U \propto n \propto N/R^3$, and (iii) the harmonic energy $V \propto R^2$. Since U scales with μ never hits zero). However, Bosons in a 2D harmonic trap can condense, because $g(\epsilon) \propto \epsilon$. By the same mathematics, in a 3D harmonic trap the condensate density is given by

$$\frac{n_0}{n} = 1 - \left[\frac{T}{T_{\text{BEC}}} \right]^3$$

instead of (1.2) because $g(\epsilon) \propto \epsilon^2$.

⁸For sodium, for example, this transition gives the well-known yellow doublet at 5890 Å and 5896 Å, and consequently the yellow color of sodium vapor lamps.

N , it becomes large in the thermodynamic limit, and for $U > 0$ (repulsive atom-atom interaction, such as ^{23}Na) a competition between U and V sets the cloud size (figure 1.1 left). For an attractive atom-atom interaction such as ^7Li (figure 1.1 right), $U < 0$ and the situation is different. For small N , the total energy has a *local* minimum and a metastable cloud can be formed, but after a critical number of atoms the cloud implodes. This is why Wolfgang Ketterle's group at MIT could make a BEC out of almost a million ^{23}Na atoms, but Randall Hulet's team at Rice University could only put $\sim 1,500$ ^7Li atoms into their BEC before the cloud imploded [21].

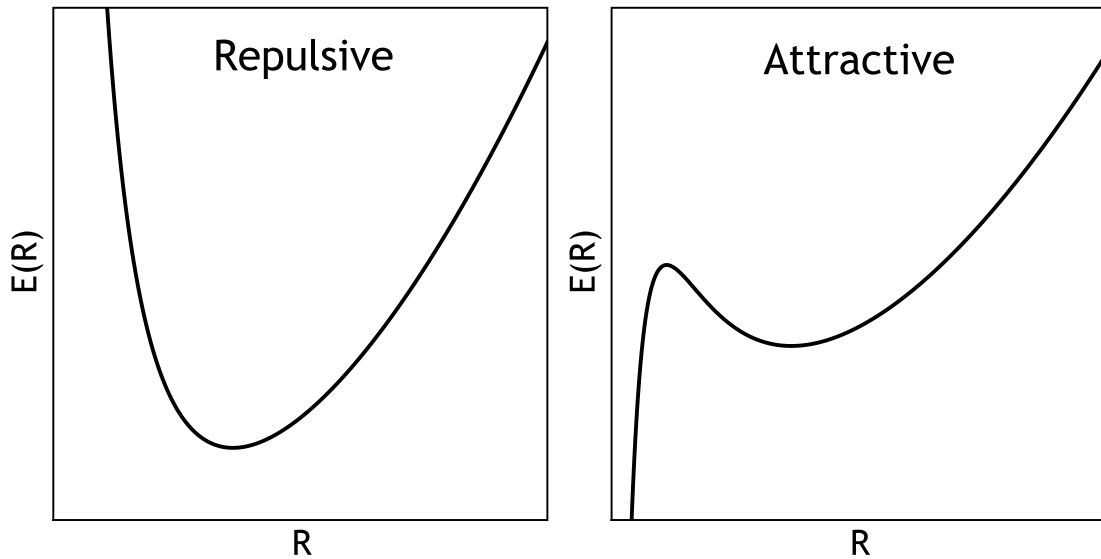


FIGURE 1.1: For a repulsive atom-atom interaction (left), there is always an equilibrium size of the cloud. For an attractive atom-atom interaction, the cloud can implode ($R \rightarrow 0$) beyond a critical particle number.

Unstable condensates such as ^7Li can be stabilized by tuning the interaction energy using a Feshbach resonance. The interaction energy per unit volume for a dilute gas at low temperatures depends on the two-body scattering length a and the density n (see, e.g., [32] or appendix G),

$$E_{\text{int}} = \frac{2\pi\hbar^2 a}{m} n^2$$

Near a resonance magnetic field B_0 , the scattering length a gets renormalized to

$$a = a_{\text{bg}} \left(1 + \frac{\Delta B}{B - B_0} \right)$$

due to the appearance of a bound state (with binding energy $E_b = \hbar^2/ma^2$) on the $a > 0$ side; a_{bg} is the scattering length in the absence of a magnetic field (see, e.g., [33] or appendix G). On either side of the field B_0 , the scattering length and consequently the two-particle interaction energy has different signs.

Irrespective of the sign of a_{bg} , the effective two-particle interaction can be tuned to be attractive or repulsive by bringing the cloud close to a Feshbach resonance. Such a knob, for example, has been used to stabilize condensates where the inherent atomic interaction is attractive, such as⁹ ^{85}Rb . Since 1995, using a combination of such techniques, scientists have Bose condensed ^{87}Rb [19], ^{23}Na [20], ^7Li [21], ^1H [28], ^{85}Rb [35], ^{41}K [36], metastable ^4He [37, 38], ^{133}Cs [39], ^{174}Yb [40], and ^{52}Cr [41].¹⁰

The proximity to a Feshbach resonance opens up experimental possibilities not available in superfluid ^4He . On the $a > 0$ side of Feshbach resonance, the molecular state has a lower energy than the atomic state. However, close to resonance the thermodynamic equilibrium state is not a pure molecular state but rather a mixture of atoms and molecules. Experimentalists used this coexistence to create a coherent mixture of atoms and molecules on the $a > 0$ side, in which the composition of the condensate oscillated between mostly atomic and mostly molecular at a frequency determined by the binding

⁹Interestingly, the ^7Li experiments [21, 34] never used this stabilization and were thus restricted to really small condensates.

¹⁰ ^{52}Cr is particularly interesting; because of the six electrons in its outer shell, its magnetic dipole-dipole interaction energy is 36 times stronger than typical alkali atom condensates which are dominated by contact interaction. By tuning the magnetic field to $a = 0$, a condensate with purely long-range anisotropic dipole-dipole interaction can be created, with signatures in the expansion [42], ground state [43] and low energy excitations [44] of the cloud. The anisotropic (dipolar) interaction can also be tuned, by time-varying magnetic fields [45], resulting in a condensate with arbitrarily tunable isotropic *and* anisotropic interactions. It's also worth noting that compared to most other species mentioned here, ^{52}Cr has extremely narrow resonances, with the broadest one being a $\Delta B = 96 \mu\text{T}$ resonance at $B = 60 \text{ mT}$ [46].

energy [47].¹¹

Novel experimental systems involving cold atomic condensates are not just restricted to those close to a Feshbach resonance. Alkali atom condensates have also been used to mimic behavior of superfluid ^4He as well as observe behavior theoretically possible for bosons but never observed in ^4He . For example, while arrays of quantized vortex lines have been observed in rotating superfluid ^4He [51], the high cost of vortex formation in three dimensions precluded the observation of a triangular flux lattice *à la* type-II superconductors [52]. Cold atomic vapors have weaker interactions and thus a lower cost to vortex formation than liquid ^4He , and in 2001 a triangular lattice of vortices was observed by spinning a 3D condensate of ^{23}Na atoms [53]. In the same year, another group did a detailed study on the nucleation of a single vortex by slowly spinning up a ^{87}Rb condensate [54], again exploiting the high degree of control in these systems. Some years later, yet another group observed the destruction of superfluidity by Kosterlitz-Thouless transition in a 2D atomic condensate [55], analogous to 2D films of superfluid ^4He .¹²

¹¹On the $a < 0$ side of Feshbach resonance, the interaction energy is negative and, not surprisingly, leads to a collapse of the condensate and the expulsion of atoms in a *Bosenova*. The critical numbers and (negative) scattering lengths required for a Bosenova were studied in detail by scientists at JILA through a series of controlled experiments [48]. They also observed that even on the $a > 0$ side of a resonance, an atomic condensate became unstable close to the resonance [49], and collapsed at a rate faster than predicted by the dominant loss mechanism of three-body recombination [50]. In chapter 2, we explain this collapse as being due a negative compressibility of the atomic cloud, which is only stabilized at much higher densities than those experimentally achieved. This instability also explains why atomic Bose condensates created by gradually sweeping a molecular phase close to resonance are never stable.

We also explain in chapter 2 why this instability is not manifested in experiments such as [47], where a coherent superposition of the atomic and molecular states is observed for $\sim 100 \mu\text{s}$. We show that the atomic state observed in [47] is not a thermodynamically stable energy minimum, but a metastable energy maximum that is stable over $100 \mu\text{s}$ timescales due to conservative Hamiltonian dynamics. This metastability also explains why adiabatic ramps close to resonance from the molecular side create atomic states that are longer lived than [49] but can't be maintained for more than $\sim 10 \text{ms}$.

¹²Since a trapped 2D ideal gas allows Bose-Einstein condensation, it's in fact not completely analogous to 2D ^4He films, which exhibit superfluidity without Bose condensation. In a 2D harmonically trapped Bose gas, superfluidity could be either due to a Kosterlitz-Thouless (KT) transition or due to Bose condensation, and only recently have matter wave interference experiments confirmed the former mechanism [56].

The overarching theme that connects all experiments with cold atomic Bose condensates is that atoms interact, and condensate collapse (or growth) and vortex formation are just two of the many possible consequences. Other consequences include soliton propagation [57, 58], zero, first and second sound [59], squeezed states [60], Tonks-Girardeau gas [61], atom lasers [62], Mott insulator-superfluid transition [63] and Anderson localization [64, 65]. While a review of each one of them is beyond the scope of this document, the interested reader is referred to [66] and references therein.

1.1.2 Degenerate Fermi gases

At phase space densities of order unity, the aforementioned phenomenon of Bose-Einstein condensation (BEC) reveals the quantum nature of bosons. By extension, we expect Fermions to exhibit their quantum nature as well when *their* phase space density reaches unity. However, due to the Pauli exclusion principle, their density cannot rise arbitrarily, and fermions do not “condense” in the sense of macroscopically occupying a single state. Instead, a Fermi surface develops below the Fermi temperature.

For an ideal Fermi gas of spinless Fermions at temperature $T = 1/k_B\beta$, the equation of state reads

$$\begin{aligned}
 n &= \frac{1}{4\pi^2} \left[\frac{2m}{\hbar^2} \right]^{3/2} \int_0^\infty \frac{\epsilon^{1/2} d\epsilon}{e^{\beta(\epsilon-\mu)} + 1} = \frac{1}{6\pi^2} \left[\frac{2m\mu}{\hbar^2} \right]^{3/2} \left[1 + \frac{\pi^2}{8(\beta\mu)^2} + O\left(\frac{1}{\beta\mu}\right)^4 \right] \\
 \epsilon = \frac{E}{V} &= \frac{1}{4\pi^2} \left[\frac{2m}{\hbar^2} \right]^{3/2} \int_0^\infty \frac{\epsilon^{3/2} d\epsilon}{e^{\beta(\epsilon-\mu)} + 1} = \frac{\mu}{10\pi^2} \left[\frac{2m\mu}{\hbar^2} \right]^{3/2} \left[1 + \frac{5\pi^2}{8(\beta\mu)^2} + O\left(\frac{1}{\beta\mu}\right)^4 \right] \quad (1.3) \\
 \frac{E}{N} &= \frac{3\mu}{5} \left[1 + \frac{\pi^2}{2(\beta\mu)^2} + O\left(\frac{1}{\beta\mu}\right)^4 \right]
 \end{aligned}$$

where the expansions to the right hold for low temperatures ($\beta\mu \gg 1$) compared to μ/k_B . At high temperatures ($\beta\mu \ll 1$), the energy per particle goes to its classical equipartition value $E/N = 3k_B T/2$, while at low temperatures ($\beta\mu \gg 1$) it goes to a constant

$3\mu/5$, reflecting the fact that the fermions must fill up all states up to the Fermi energy $\epsilon_F = \mu(T = 0)$, and cannot have arbitrarily low energies even at zero temperature. The temperature at which this crossover from classical to quantum behavior occurs ($\beta\mu = 1$) can be considered to be the temperature for the onset of Fermi degeneracy. At temperatures below $T_F = \epsilon_F/k_B$, we can expect the consequences of Fermi statistics to dominate.¹³

Unlike Bose condensates, degenerate Fermi gases are fairly common in everyday life. Valence electrons of metals form a Fermi liquid with $T_F \sim 10^5$ K, so at room temperature (300 K) they are highly degenerate. However, an atomic gas of degenerate fermions has some unique properties not exhibited by a degenerate electron gas in metals. First, interatomic interaction can be tuned by a Feshbach resonance, and consequently energy scales arising out of that interaction can be varied over a wide range with respect to the Fermi energy. For example, in normal metals, although the Fermi temperature is $\sim 10^5$ K, the superconducting transition temperature is a few Kelvins, a consequence of the weak lattice mediated electron-electron interaction.¹⁴ In a cold atomic system, the transition temperature can be tuned to be of the same order of magnitude as the Fermi temperature. Second, the charge on electrons precludes certain states such as magnetized superconductors (or Cooper pairing between spin-imbalanced electrons), because magnetic fields are completely screened by supercurrent eddies. Since cold fermionic atoms are neutral, they can undergo Cooper pairing in the presence of a spin imbalance and display a whole slew of behaviors not observed in degenerate electrons. Third, electron-electron interaction is always monopolar. Cold fermionic atoms, on the other hand, can display dipole-dipole

¹³The chemical potential itself is equal to the Fermi energy only at zero temperature, while at finite temperature it is given by [67]

$$\mu = \epsilon_F \left[1 - \frac{\pi^2}{12} \left(\frac{k_B T}{\epsilon_F} \right)^2 - \frac{\pi^4}{80} \left(\frac{k_B T}{\epsilon_F} \right)^4 + O \left(\frac{k_B T}{\epsilon_F} \right)^6 \right]$$

¹⁴For example Mercury, the first known superconductor, has $T_F \approx 79,600$ K and $T_c = 4.2$ K, while Tin, another well-known superconductor, has $T_F \approx 74,500$ K and $T_c = 3.7$ K.

interaction (e.g., ^{52}Cr), exhibiting physical phenomena not observed in metals.

Fermi pressure, rather than interactions, sets the size of clouds of trapped Fermi gases by placing upper limits on the real and momentum space densities. This can be used to detect the onset of Fermi degeneracy, as demonstrated by scientists at Rice University and JILA. When the Rice group cooled down a mixture of ^7Li and ^6Li atoms to $T = T_F/4$, they saw that the bosonic ^7Li atoms shrunk to a cloud a third of the size at $T = T_F$, while the fermionic ^6Li cloud stayed at the same size as at $T = T_F$ [68]. Since the interatomic potentials between all the atoms in the mixture were identical, this difference in behaviors was a dramatic visually obvious consequence of Fermi statistics. The JILA group looked at the momentum and energy distribution in a cloud of fermionic ^{40}K cooled to $T = T_F/2$. They observed the energy per particle cross over from $3k_B T/2$ for $T > T_F$ to $3k_B T_F/5$ for $T < T_F$, and the momentum distribution go from a gaussian ($T > T_F$) to a parabola ($T < T_F$) [69], complementing [68]’s observations in momentum space.

The Pauli exclusion principle, which is behind Fermi pressure, makes fermionic clouds stable against collapse even for attractive interactions, but also makes it harder to achieve degeneracy. The final cooling step to achieve either Bose or Fermi condensation is always evaporative (see appendix D.2 for a discussion), where the trap is lowered to leak out the more energetic atoms. The rest of the cloud, which now has a lower average energy per particle, thermalizes to a lower equilibrium temperature. Thermalization in a fermionic cloud is hindered at low temperatures due to two effects, which are consequences of Pauli exclusion in real and momentum space.

First, thermalization requires elastic collisions between atoms. For a collision with center of mass angular momentum¹⁵ ℓ , the distance of closest approach d and the relative momentum p must be related by $d \times p = \ell \hbar$. At low temperatures, p is bounded above

¹⁵For $\ell = 1, 2, 3 \dots$, these collisions are called s-wave, p-wave, d-wave and so on and so forth

by the Fermi momentum $p_F = \hbar(6\pi^2n)^{1/3}$. Thus for a $\ell > 0$ collision, d must satisfy $nd^3 > 1/6\pi^2$, or $d \gtrsim r$, where $r \propto n^{-1/3}$ is the interparticle spacing. Elastic collisions between neutral alkali atoms are mediated by short-range van der Waals potentials. The typical range of these potentials is about $5 a_0$ [70], which is also the atomic size, and much less than r . So at $d \gtrsim r$, the interatomic potential is too weak to cause a collision, and the only elastic collisions possible at low temperatures are $\ell = 0$ (s-wave). But an s-wave collision with a $5 a_0$ -range potential requires two identical fermions to spatially overlap, which is forbidden by the Pauli exclusion principle [71]. Thus thermalizing collisions between identical fermions are suppressed at low temperatures.

Second, in the energy-momentum space, cooling by thermalization involves high energy atoms being scattered into low energy states (figure 1.2, left), reducing the average energy per particle. However, as the temperature is lowered, states below the Fermi energy start filling up (figure 1.2, center), reducing thermalizing collisions until for $T \ll T_F$ (figure 1.2, center) thermalizing stops altogether, effectively blocking evaporative cooling [69].

To get around the first problem, experimentalists utilize thermalizing collisions either between two different spin states of the same fermionic atom, or collisions between two different atomic species. For example, [69] and [72] trapped two different spin states of the same fermionic atom. Since s-wave collisions between non-identical fermions are not suppressed, they can cool the fermions to degeneracy. This, however, does not counter Pauli blocking, since each of the fermionic species freezes into its own Fermi sea. Consequently, [69] and [72] could not reach temperatures below $T_F/2$ (roughly).

To get around Pauli blocking, [68] and [73] cooled fermionic ${}^6\text{Li}$ by placing it in contact with a Bose condensate of ${}^7\text{Li}$, by a technique known as sympathetic cooling. Since only some of the atoms are now Pauli blocked, collisions are not completely suppressed.

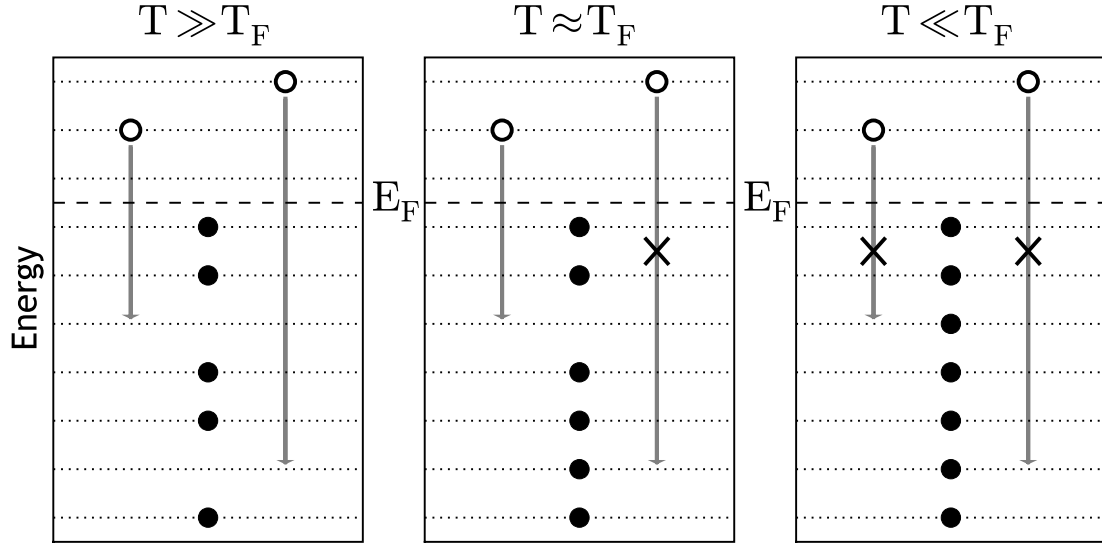


FIGURE 1.2: Solid circles denote atoms below the Fermi energy E_F , while hollow circles denote high energy atoms that need to lose energy during thermalization. At $T \gg T_F$ (left), there are unoccupied states below E_F where high energy atoms can scatter into, thereby lowering the average energy per particle. At $T \approx T_F$ (center), there are very few vacant states left below E_F , so scattering events that would lead to cooling are reduced. At $T \ll T_F$ (right), all states below E_F are occupied, so the high energy atoms cannot lose their energy, and cooling stops.

Since then, temperatures as low as $0.1T_F$ have been achieved by sympathetic cooling of Fermi gases [74].

While Pauli blocking makes it hard to cool fermi gases evaporatively, it is also one of the signatures of Fermi degeneracy, the threshold at which quantum effects become apparent in macroscopic properties. Besides affecting thermalizing time scales [75], Pauli blocking also changes mechanical collective modes in a gas, such as sound propagation. Sound waves in a fluid are pressure and density waves that propagate by collisional relaxation between adjacent regions of space. A suppression of collisions therefore leads to a suppression of sound propagation, observed as rapidly damped sound waves in a ^{40}K cloud [76].

In the days since the first degenerate Fermi gases, experimentalists have explored a

whole host of novel systems, including unequal-mass Fermi mixtures [77], p-wave pairing [78, 79], three strongly interacting Fermi states [80] and fermions in optical lattices [81, 82]. Without a doubt, however, the most important consequence of our ability to cool and manipulate Fermions is the revival and validation of the concept, developed in the 1980s, of a *BEC-BCS crossover* [13, 83, 84].

1.1.3 BEC-BCS crossover

At low temperatures, as John Bardeen, Leon Neil Cooper and John Robert Schrieffer explained in 1957, the Fermi sea of electrons in some metals is unstable to a lower energy ground state. In this ground state, electrons of opposite spins and momenta are paired into singlets due to a phonon-mediated attractive interaction. There is an energy cost to breaking a pair, and as a result at $T \rightarrow 0$ electron-hole excitations are suppressed. This blocks scattering events that give rise to resistivity in regular metals, and an electric current can flow without resistance [11]. For a summary of the BCS theory, see appendix B.

The BCS theory was accepted as the explanation of superconductivity, primarily because of the accuracy of its quantitative predictions, such as the Meissner effect [85], specific heat [86, 87], radio-frequency absorption [88, 89], superconducting transition temperature and critical magnetic field [90], isotope effect [91, 92], tunneling density of states [93], Josephson tunneling [94, 95] and Aharonov-Bohm effect in superconducting loops [96]. With the discovery of superfluidity in ^3He below 2.5 mK [15, 97], the BCS theory was generalized to spin-triplet (p-wave) Cooper pairs, using interatomic potentials as a pairing mechanism between neutral fermions [16]. In a sense, the acceptance of BCS theory was helped by the fact that high- T_c superconductors – which are not well-explained by BCS theory – were not discovered until 1986 [98–101].

Even before the unveiling of high- T_c cuprates, the success of BCS theory in explaining the superfluidity of ^3He raised a natural question: was the BCS pairing related in any way to the pairing between two ^3He atoms that formed a bona-fide $^3\text{He}_2$ molecule [102]? And was there a mathematical relation between the BE condensation of such molecules and emergence of a BCS order below some temperature? These were not far-fetched ideas, since there was no symmetry difference between a Cooper pair of weakly bound fermions and a tightly bound difermionic molecule; all the differences, such as binding energy and size, were quantitative.

Schafroth in 1954 had the right idea when he postulated that conduction band electrons in metals paired up to form charged bosons [103] which underwent superfluid motion below their BEC temperature, giving rise to a supercurrent [104]. However, his ideas were shelved due to lack of quantitative agreement with experiments. The pairing of neutral fermionic ^3He atoms brought back into focus the possibility that BCS superconductivity was really the same phenomenon as the BE condensation of difermionic molecules – albeit in very different parameter regimes. To explore that possibility, two questions needed to be answered: was the BCS theory the weak-coupling limit of a more general theory of paired fermions, which in the strong-coupling limit yielded tightly bound bosonic molecules? If so, then was the BEC transition temperature of the bosonic molecules the strong-coupling limit of a more general temperature scale, which in the weak-coupling limit reduced to the BCS superconducting transition temperature?

In 1980, Tony Leggett presented a model by which he could answer the first of the two questions [83, 84]. Considering s-wave contact interaction between two fermions at $T = 0$, he showed that for weak attractive interaction a BCS superfluid appeared, whereas for strong attractive interaction the ground state was a BEC of di-fermionic molecules. In 1985, Nozières and Schmitt-Rink, using a diagrammatic approach, extended this picture

to $T > 0$, and proved that indeed, T_{BCS} and T_{BEC} were the weak and strong coupling limits of a pairing transition temperature. The coupling strength for a contact interaction can be quantified by the two-body scattering length a ; $a \rightarrow 0^-$ yields the BCS limit of weak attractive interactions, whereas $a \rightarrow 0^+$ reduces to the limit of tightly bound molecules. The connection between the two can be summarized by a phase diagram such as figure 1.4 (left) [105].

On the BCS side, the phase diagram shows that Cooper pairs form and condense at the same temperature, reflecting the well-known fact that current carriers have been observed to have a charge $2e$ only in the superconducting phase. On the BEC side, however, molecules remain non-condensed but paired above their BEC transition temperature. Further, as we saw in § 1.1.1, even interactions as strong as in ^4He have a relatively small effect on T_{BEC} , therefore the transition temperature on the BEC side is more-or-less constant as a function of interaction strength. Above the transition temperature on the BCS side, the normal state is a Fermi liquid of unbound fermions, which forms molecules at a characteristic crossover temperature (dashed curve in figure 1.4, left) set by the interaction strength [105]. The two limits are separated by the so-called unitarity limit, where the two-body scattering length diverges.¹⁶The chief significance of this point is that the only remaining finite length scale is the interparticle spacing $n^{-1/3}$, so all other intensive physical quantities of the system must be *universal* functions of that length scale. In other words, ratios such as T_c/T_F , μ/ϵ_F and Δ/ϵ_F must be the same for all systems at unitarity.

Although appealing to theorists because of its simplicity, this framework of a crossover between the BEC and BCS limits remained of purely academic interest throughout the 80s, since there were no experimental systems that could mimic or observe this crossover.¹⁷ Interest in crossover physics was revived in the 1990s by theorists who argued that the

¹⁶see appendix G for a presentation in terms of the scattering matrix

¹⁷If, for example, we could bring the electron gas in a typical metal to unitarity, we would have superconductivity at 10,000 K.

weak-coupling BCS theory was insufficient to account for the high transition temperatures of the cuprate superconductors [105]. But this field really took off with the realization of Fermi degenerate cold gases, whose tunable interactions, unlike superconductors and superfluid ^3He , could be used to explore both the limits as well as the crossover region in between.

Creation of diatomic molecules out of two different spin states of a fermion followed close on the heels of cooling a Fermi gas to degeneracy. Randy Hulet's group at Rice, Christophe Salomon's group at ENS and Rudy Grimm's group at Innsbruck almost simultaneously created long-lived diatomic $^6\text{Li}_2$ molecules by subjecting them to a magnetic field on the BEC side of their Feshbach resonance [106–108]. Simultaneously, Debbie Jin's group at JILA performed the same feat with $^{40}\text{K}_2$ molecules [109]. Although these molecules were too warm to Bose condense (yet), no one doubted that a BEC of di-fermionic molecules was on the horizon. The wait period was rather short, and in the same year scientists at MIT [110], Innsbruck [22] and JILA [111] reported the Bose-Einstein condensation of $^6\text{Li}_2$ and $^{40}\text{K}_2$ on the BEC side of their respective resonances. One half of the phase diagram (figure 1.4, left), the BEC limit of tightly bound molecules, was explored.

Detecting a condensate of Cooper pairs at the other limit of the crossover was not as straightforward as observing a BEC of bosonic pairs. For bosonic molecules, a peaked distribution in real and momentum space is an infallible signature of Bose condensation. However, the size of Cooper pairs on the BCS side is comparable to the cloud size, and the similar shape and size of the condensed and the normal gases makes it difficult to detect condensation in the BCS limit. Techniques to indirectly detect BCS condensation were therefore developed.

The expansion of a spin-balanced Fermi gas near resonance at low temperatures was

found to be hydrodynamic, similar to the expansion of a superfluid, suggesting the presence of superfluid order on the BCS side [112]. Collective breathing mode frequencies and damping parameters close to resonance on the BCS side were also inconsistent with Fermi liquid predictions [113, 114]. A signature of superfluid transition was also observed in the specific heat [115]. A pairing gap, analogous to the BCS order parameter, was observed spectroscopically in a two-component ${}^6\text{Li}$ gas [116]. Some experimentalists adiabatically ramped a magnetic field from the BCS to the BEC side and saw a condensate of molecules [23, 117]. Since the ramps were faster than molecular condensation times, the existence of a molecular condensate was considered proof positive for the existence of a condensate on the BCS side [118].

The most visually stunning proof of the existence of a condensate throughout the crossover region came in 2005, when Ketterle’s group loaded a 50-50 mixture of $|m_F = \pm 1/2\rangle$ spin states of ${}^6\text{Li}$ in an optical trap, stirred the cloud for a second, and observed long-lived vortices *persisting throughout the crossover region* from $1/k_F a = -0.37$ to $1/k_F a = 2$ [119]. The formation of vortices is a sure signature of superfluidity, and their experiment finally connected the BEC and BCS limits below the Bose-Einstein condensation temperature.¹⁸

With the experimental realization of the BEC-BCS crossover, considerable interest has emerged in studying crossover physics in spin-imbalanced Fermi systems. While pairing between fermions with different chemical potentials is possible [17, 18], the phase space for such a pairing is extremely small in three dimensions [121] and would require careful tuning of the individual chemical potentials. More generically, a spin-imbalanced system at $T = 0$ can have at least three different phases (figure 1.3). A normal phase, without any pairing order, will form when the pairing energy is small compared to the

¹⁸I have been somewhat glib about alternately using the terms superfluidity and Bose-Einstein condensation. For a 3D system without disorder such as [119], the two are indeed interchangeable. However, in general it is possible to have superfluidity without BEC in lower dimensions, and BEC without superflow in disordered systems [120].

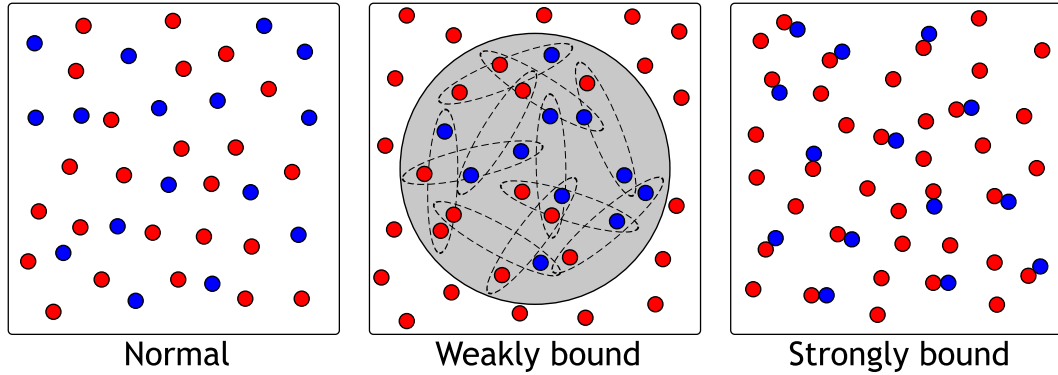


FIGURE 1.3: For either non-interacting fermions or for fermions mismatched above the CC limit, there is no pairing and the stable phase is a “normal” Fermi liquid. For weakly bound pairs *a la* Cooper pairs, there is a phase separation between the gray superfluid core and the excess fermions, because the transition is discontinuous. Once the pairs are tightly bound into molecules, the system is a Bose-Fermi mixture, and may or may not be phase separated. Red circles are the majority species.

chemical potential mismatch (see, e.g., figure B.1, left, $h > h_c$). In that case, the chemical potential mismatch is said to be greater than the so-called Chandrasekhar-Clogston (CC) limit [122, 123]. When the pairing energy barely beats the mismatch (figure B.1, left, $h < h_c$), large delocalized Cooper pairs form. Since the transition to a paired superfluid is first order, the two phases are separated spatially. As the pairs become more tightly bound (and, as a result, smaller), the fact that the bosons are composite objects become less and less important, and eventually the systems acts like a mixture of bosons and fermions. Whether there is phase separation or not depends on the details of the atom-atom, atom-molecule and molecule-molecule interactions.¹⁹

¹⁹As we will see in chapter 5, for cold gases, although there is phase separation in this regime, the two phases are not necessarily pure fermions and pure bosons. In general, a partially polarized normal phase could also coexist with a superfluid phase [124], and which of these phases coexists with which will be determined by the nature of the transition between them.

In chapters 3 and 4, we study these spin-polarized Fermi systems near unitarity in some detail. In 2006, two different groups subjected spin-polarized mixtures of ${}^6\text{Li}$ in its two lowest hyperfine states to unitarity [74, 125]. At $T = 0$, both groups obtained superfluidity at the trap center. Working with an extremely elongated cigar-shaped trap, [2, 74] observed two shells in their density profile; a superfluid core surrounded by a fully polarized normal shell. However, working with a less elongated trap, [125, 126] observed *three* shells in their density profile, which they interpreted as due to a superfluid core, a fully polarized normal outer shell, and a middle shell of indeterminate origin – which they claimed was a “partially paired superfluid” phase (an unfortunate misnomer, since this phase was above the CC limit and

Recently, putting these crossover systems on optical lattices has become another direction of research. By tuning the lattice depth and interatomic interaction, the on-site and hopping interactions can be simultaneously tuned, providing an ideal model of solid-state systems. Researchers have managed to achieve both a condensate of molecules [81] as well as a superfluid across the BEC-BCS crossover region [82] for fermions in an optical trap. Current research is focused on using cold atoms to simulate solid state systems [127].

Deep in the BEC side of resonance, a spin-imbalanced system can be described as a Bose-Fermi mixture of molecules and atoms [128]. This is a very specific case of a more general interacting heteronuclear Bose-Fermi mixture. Feshbach resonances have been observed in such mixtures of ^{87}Rb and ^{40}K [129]. Using enhanced collisions near such a resonance, scientists in Florence and JILA have simultaneously cooled a Bose-Fermi mixture to degeneracy [130, 131]:²⁰

While a Feshbach resonance can tune the interaction between two species, or two hyperfine states of a Fermion, some atoms have multiple hyperfine states with multiple closely-spaced Feshbach resonances between the different possible pairs. This leads to a mixture of more than two strongly interacting species. Recent spectroscopic measurements have observed signatures of two nearby Feshbach resonances in three-fermion

hence normal). We devote chapter 3 calculating the phase diagram of a vanishingly small fraction of down spins in a Fermi sea of up spins, in particular the ratio of their chemical potentials at which the density of down spins goes to zero. We see that the Nozières-Schmitt Rink (NSR) formulation overestimates the interaction at unitarity; while the NSR prescription correctly interpolates between the BEC and BCS limits, *at* unitarity, it fails due to strong interactions.

The elongated trap [2, 74], on the other hand, observed an effect absent in [125, 126]. Although the oscillator lengths were much larger than the interparticle spacing, there was an apparent LDA violation; the boundary between the two shells in [2, 74] did not follow an isopotential contour. In chapter 4, we explain this as being due to surface tension between the two shells, arising from a first order phase transition. We calculate the coefficients of a Landau-Ginzburg free energy to estimate the surface tension at a superfluid-normal interface, and compare it to empirical fits to experimental data.

²⁰This has strong parallels with a ^3He - ^4He mixture, and in chapter 5, we show how an interacting Bose-Fermi mixture can be used to construct a “dilution fridge” in a cold atomic system, analogous to a ^3He - ^4He dilution refrigerator.

systems.²¹

1.1.4 Future directions and parallels with other systems

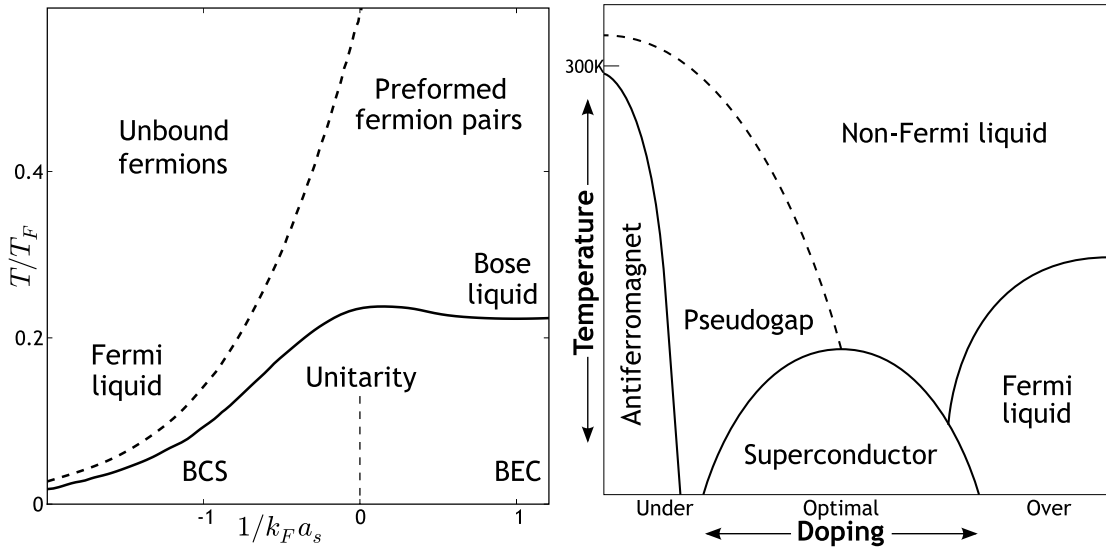


FIGURE 1.4: Analogy between BEC-BCS crossover for cold gases and high- T_c superconductors. **Left:** (Schematic) phase diagram for cold gases near unitarity, according to [105]. Deep in the BCS side (conventional superconductors), Cooper pairs form and condense at the same T , while deep in the BEC side, molecules that form do not necessarily condense until sufficiently cooled. **Right:** Well-known phase diagram for cuprate superconductors. The area below the dashed curve displays a *pseudogap* phase, which is characterised by a suppression of the density of states near the Fermi energy without a superconducting gap.

The unprecedented control available for cold atomic gases has brought a little known concept from 20 years ago to the forefront of theoretical physics. While any theory that successfully connects widely disparate phenomena such as molecule formation and su-

²¹For example, the three lowest hyperfine states of ${}^6\text{Li}$ ($|1/2, 1/2\rangle$, $|1/2, -1/2\rangle$ and $|3/2, -3/2\rangle$, respectively called $|1\rangle$, $|2\rangle$ and $|3\rangle$) have pairwise resonances at 834 G, 811 G and 690 G, even the narrowest of which is 122 G wide. This means that at a field of, say, 760 G and Fermi energy of 13 KHz, all three pairs will be close to unitarity, with $1/k_F a$ of 1.15, 0.98 and -0.99. A group at MIT [80, 132] observed the RF spectra of a paired $|1\rangle$ - $|2\rangle$ state at unitarity to be very different from what a pairing gap picture would suggest [116]. In chapter 6, we will calculate how the presence of a $|1\rangle$ - $|3\rangle$ resonance near the unitarity of $|1\rangle$ - $|2\rangle$ changes the RF spectrum due to strong $|1\rangle$ - $|3\rangle$ interactions. We will also show that generically such a spectrum can be of two types, and will classify existing RF spectroscopy experiments accordingly.

perconductivity is exciting in its own right, some scientists are hopeful that crossover physics might also explain the as-yet unexplained phenomenon of high- T_c superconductivity in cuprates. The optimism stems from the fact that the phase diagram of a cuprate superconductor (figure 1.4, right) looks topologically similar to the BEC-BCS phase diagram for cold gases (figure 1.4, left). The low (high) impurity limit for cuprates corresponds to the BEC (BCS) limit of cold gases. For low hole doping, before the onset of superconductivity, cuprate superconductors display a pseudogap state, where the tunneling density of states at the Fermi level is partially suppressed, signaling the onset of some kind of order [133–135]. If this were due to pre-formed electron pairs, it would be analogous to the BEC side of the cold gas phase diagram, where pairs form at a much higher temperature than their condensation temperature. On the highly doped side, cuprates do not display a pseudogap, much like Cooper pairs form and condense simultaneously in the BCS limit. If the pseudogap were due to some sort of pairing order, then understanding crossover physics could give us clues to high- T_c superconductivity.

While it is easy to get carried away by these analogies, it should be kept in mind that till date, no experiment on high- T_c superconductors has conclusively proved the existence of pre-formed pairs, despite promising forays [136]. On the other hand, no cold gas experiment has ever demonstrated the existence of a pseudo-gap, although successful theories to explain spectroscopic experiments include theories involving a pseudogap [137]. More investigation is needed on both fronts, but there is room for cautious optimism [138].

Attempts are also underway to draw parallels between cold atoms and degenerate fermions at a different energy scale, – quark-gluon plasma, neutron stars and white dwarfs. While the energy scales are different, due to the universality of the physics at unitarity, measurements of viscosity and three-species pairing in cold gases could provide insight into the behavior of the higher energy systems [139].

CHAPTER 2
THERMODYNAMICS OF BOSE CONDENSATES NEAR A FESHBACH
RESONANCE

This chapter was adapted from “Stability of bosonic atomic and molecular condensates near a Feshbach resonance” by Sourish Basu and Erich J. Mueller, published in Physical Review A 78, 053603 (2008) [140].

Using Feshbach resonances [141], experimentalists can tune the interactions in atomic clouds [47, 106, 111, 112, 116, 142, 143]. For a system of Fermi atoms, this technique has allowed the study of a crossover between a BCS superfluid of Cooper pairs to a BEC superfluid of molecules [111, 112, 116, 143]. Recently three separate theoretical groups [144–146] have proposed that for Bosonic atoms the same technique can produce a phase transition between an atomic and a molecular superfluid (respectively called ASF and MSF henceforth, after [145]). If, as suggested by Romans *et al* [144] and Radzihovsky *et al* [145], this quantum transition is continuous, then it would be in the Ising universality class, with dramatic signatures in the properties of vortices. The topological character of this phase transition makes it of intense interest to a large community of physicists.

Here we show that in the limit of vanishing molecule-molecule and atom-molecule interaction (the same limit considered in [144] for constructing their phase diagram), no ASF \leftrightarrow MSF phase transition can occur near a Feshbach resonance (defined as where the molecular binding energy approaches zero). Previous work [144, 145] showed that as one decreases the magnitude of the molecular binding energy, but before reaching resonance, the MSF becomes unstable. In those works it was *assumed* that the instability leads to a phase containing atomic superfluid order. We demonstrate that without the stabilizing influence of molecule-molecule interaction the system has a negative compressibility and this instability actually leads to a mechanical collapse of the cloud, and adding repulsive

molecule-molecule interaction only stabilizes the cloud at sufficiently high density (estimated at least three orders of magnitude higher than current experiments [47, 49, 147]). Three-body losses are therefore likely to make the phase transition unobservable.

Experiments are routinely performed [47, 49] on dilute atomic clouds on the molecular side of a resonance (i.e., the side on which a bound molecule exists), so this instability cannot be the whole story. Indeed, we verify the existence of a mechanically stable ASF in this region and show that it always has a larger energy than the molecular condensate, precluding the possibility of a phase transition (even a first order one). Furthermore, we demonstrate that this ASF is a saddle point of the free energy, and it is always energetically favorable for atoms to recombine into molecules. It is only the slow kinetics of this recombination, which relies upon three-body collisions, which allows experiments to be performed on atomic condensates. A simple model of these kinetics was presented by Cragg and Kerman [148].

Most of our points about the properties of the atoms were made by Timmermans, Tommasini, Hussein, and Kerman [149] several years before the publication of refs. [144–146]. In particular, Timmermans et al. were aware of both the topography of the energy landscape and the mechanical instability which precludes a pairing transition. The main new contribution of this work is that we perform a detailed analysis of interactions. This is particularly important given the potential of these terms to stabilize the cloud.

2.1 Phase diagram

We model the Hamiltonian for a mixture of atoms and molecules near a one-channel Feshbach resonance as

$$\begin{aligned}
 \mathcal{F} &= \int [F_m(x) + F_a(x) + F_{am}(x)] d^3x \quad (2.1) \\
 F_a &= \frac{\nabla \psi_a^\dagger \nabla \psi_a}{2m} - \mu \psi_a^\dagger \psi_a + \frac{\lambda_a}{2} \psi_a^\dagger \psi_a^\dagger \psi_a \psi_a \\
 F_{am} &= g [\psi_m^\dagger \psi_a \psi_a + \psi_a^\dagger \psi_a^\dagger \psi_m] + \lambda_{am} \psi_m^\dagger \psi_a^\dagger \psi_a \psi_m \\
 F_m &= \frac{\nabla \psi_m^\dagger \nabla \psi_m}{4m} + (\epsilon - 2\mu) \psi_m^\dagger \psi_m + \frac{\lambda_m}{2} \psi_m^\dagger \psi_m^\dagger \psi_m \psi_m
 \end{aligned}$$

where F_a and F_m represent the pure atomic and molecular contributions, and F_{am} the coupling between them. Field operators $\psi_a(x)$ and $\psi_m(x)$ respectively annihilate atoms and molecules at position x (which is suppressed in these equations). Parameters λ represent the strengths of elastic scattering, while g represents the strength of conversion between atoms and molecules, μ is the chemical potential, and $\epsilon < 0$ is the binding energy of a molecule, which can be controlled by tuning an external magnetic field. To treat this Hamiltonian within mean field theory one must renormalize the coupling constants from their bare values. For example, Duine and Stoof [150] have derived a simple renormalization scheme which connects these quantities with their bare values, providing their magnetic field dependence. We emphasize however that for bosons near a Feshbach resonance there is no simple expression relating the various λ 's.

In this paper, we find the stationary points of (2.1), and analyze their stability. We discuss two types of stability: dynamic, where small fluctuations do not grow in time; and thermodynamic, where small fluctuations cannot reduce the free energy. Although a thermodynamic instability implies that the system will eventually decay, the timescale, which is governed by kinetics and dissipation, may be long enough that the system appears stable. (In fact, since the ground state of alkali atoms at nano-Kelvin temperatures

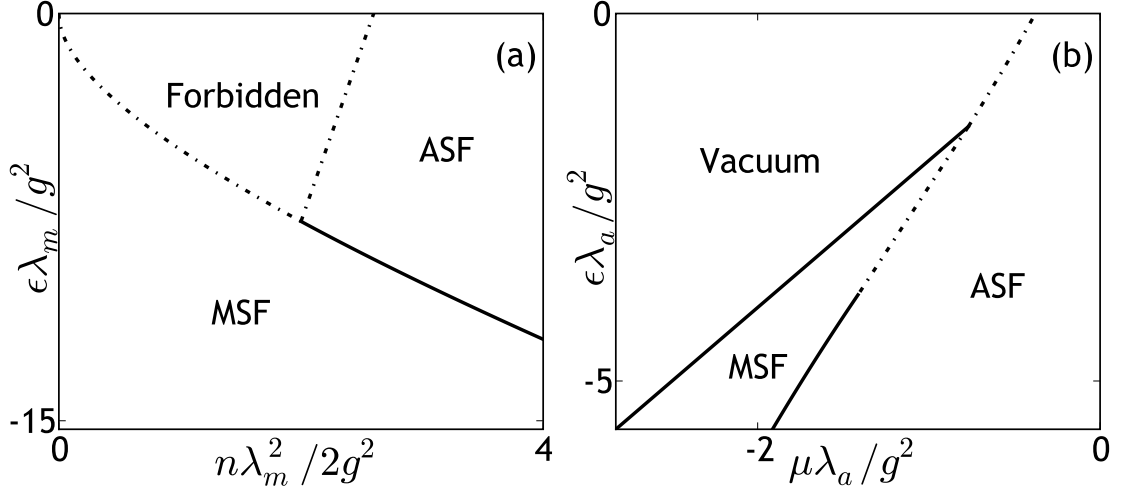


FIGURE 2.1: Phase diagrams of Eq. (2.1) without background atom-molecule scattering ($\lambda_{am} = 0$) in the parameter space of binding energy ϵ and density n (a) or chemical potential μ (b), at $\lambda_m = 2\lambda_a$. As quantitatively discussed in the text, similar results hold for more general values of λ_m . The various dotted lines separate phases with a discontinuous transition, while the solid lines denote a continuous transition. The tricritical point between MSF and ASF in the two figures, at $n\lambda_a\lambda_m = 2g^2$, corresponds to the lowest density for which a stable ASF exists. The forbidden region in figure (a) corresponds to a coexistence region where the system phase separates.

is a solid, all experiments on ultracold atoms involve states which are thermodynamically unstable.) Following convention, we describe a thermodynamically unstable (but dynamically stable) phase as metastable. In determining the stability of the system we will only consider long wavelength modes, hence it is possible that some of the metastable states we report are actually dynamically unstable.

As shown by previous authors [144, 145], for $g \neq 0$, there are two possible superfluid orders: (a) a pure molecular condensate $\phi_m = \langle \psi_m \rangle \neq 0$, $\phi_a = \langle \psi_a \rangle = 0$; and (b) a mixed atomic/molecular condensate $\phi_a \neq 0$, $\phi_m \neq 0$. States with these respective orders will be called a molecular superfluid (MSF) and an atomic superfluid (ASF).

Generically there are two classes of modes that can destabilize these states: density fluctuations, and pairing fluctuations. The latter modes change the relative population of

atomic and molecular states without changing the total density. Mueller and Baym [151] characterized both types of modes within a random phase approximation, showing that in the absence of a molecular bound state there is no phase transition between an atomic and paired superfluid. Our current calculation extends this result to the case where a true molecular bound state exists.

Our primary results are the phase diagrams in figure 2.1, shown for $\lambda_{am} = 0$ and $\lambda_m/\lambda_a = 2$. Due to the presence of metastable states in experiments involving ultracold alkali atomic vapors, we do not limit our discussion to the thermodynamic ground state in each region, but also analyze the stability of other stationary points of the energy, which can have either ASF or MSF character. These stationary points, hereafter called solutions, can be found by working at either fixed density or fixed chemical potential. All ASF states share the same symmetry. When we find multiple ASF states at the same parameter, they will have varying molecular contribution.

Fixing the density (figure 2.1(a)), the “forbidden” region contains three or four solutions, all of which are unstable: A_1 , an ASF thermodynamically unstable to pairing; A_2 , an ASF dynamically unstable to density fluctuations; M , an MSF unstable to pairing; and optionally A_3 , an ASF dynamically unstable to relative phase fluctuations. Such forbidden regions, where there are no stable bulk phases, are generic features of first-order phase transitions. They correspond to coexistence of two bulk phases: a system taken to the forbidden region will spontaneously phase separate into an MSF and a much higher density ASF, much as a thermos flask filled with water molecules can spontaneously separate into liquid and vapor. The “MSF” region contains a stable MSF, and either one (A_1) or three (A_0, A_1, A_2) ASF solutions, two of which (A_0, A_1) are thermodynamically unstable to pairing while the other (A_2) is dynamically unstable to density fluctuations. A_1 , however, is *dynamically* stable against all fluctuations if $\epsilon\lambda_a < 2g^2$. That is, under these

conditions, A_1 is metastable. The “ASF” region contains two (A_1, A_2) or three (A_1, A_2, A_3) ASF solutions, one (A_2) of which is stable. In this region the MSF (M) is unstable to pairing.

Fixing the chemical potential (figure 2.1(b)), the “vacuum”, where the ground state contains no particles, has an unphysical ASF solution with negative density. The “MSF” region contains a stable MSF solution, an unphysical ASF solution, and possibly two more ASF solutions, one unstable and the other metastable, possessing a higher free energy than the MSF. The unphysical solution has negative density. The “ASF” region contains three ASF solutions, one of which is unphysical, one unstable, and one stable. The unphysical solution corresponds to negative density, and the unstable one becomes stable when $\mu > 0$. In this region, the MSF is either unstable to pairing or has a higher free energy than the stable ASF solution.

In the remainder of this paper, we derive those results; we find the stationary states of the Hamiltonian (2.1) and analyze their dynamic and thermodynamic stability against density and pairing fluctuations at $\lambda_m = \lambda_{am} = 0$. We then explore the role of finite λ_m and λ_{am} . We give full details for the calculation at fixed density, and briefly sketch the procedure for fixed chemical potential.

Given that we are using a mean field approach it is important to address the point that the model in (2.1) is often quoted as an example of a Hamiltonian with a “fluctuation driven” first order phase transition [144, 146], where taking into account quantum fluctuations turns a second order phase transition into a first order one. This standard nomenclature can be slightly confusing: what it physically corresponds to is the fact that the mean-field prediction of the location of the tricritical point is shifted by quantum fluctuations. This shift results in a parameter range for which the mean-field theory predicts a second order phase transition, but for which the actual system displays a first order

transition. The topology of figure 2.1 is generic and, aside from a small critical region, one expects that the effects of quantum fluctuations can be incorporated into a renormalization of the parameters. We feel that our estimates of the feasibility of observing the pairing phase transition transcend the mean-field approximation.

2.2 Stationary States (fixed density)

Assuming a uniform condensate exists, we replace the field operators in Eq. (2.1) by their expectation values, $\phi_m = \langle \psi_m \rangle = \sqrt{n_m} e^{i\theta_m}$ and $\phi_a = \langle \psi_a \rangle = \sqrt{n_a} e^{i\theta_a}$, where $n_{a/m}$ and $\theta_{a/m}$ are the number of condensed atoms/molecules and their phase. The energy only depends upon the phase difference $4\xi = \theta_m - 2\theta_a$, so without any loss of generality we will take ϕ_a to be real and positive. Setting $\partial \langle \mathcal{F} \rangle / \partial \xi = 0$ shows that ϕ_m must also be real, but not necessarily positive. We work at fixed density, $n = n_a + 2n_m$, writing $\phi_m = \sqrt{n/2}x$, and $\phi_a = \sqrt{n}\sqrt{1-x^2}$ with $-1 \leq x \leq 1$. The points $x = \pm 1$ represent the same state. The shifted energy $\mathcal{E} = \langle \mathcal{F} \rangle + (\mu - \epsilon/2)n$ is then

$$\mathcal{E} = \frac{\lambda_a n^2}{2}(1-x^2)^2 + \frac{\epsilon n}{2}(x^2-1) + \sqrt{2n^3}gx(1-x^2) \quad (2.2)$$

We define the dimensionless parameters $\alpha = \lambda_a n^{1/2}/2g\sqrt{2}$ and $\beta = \epsilon/2g\sqrt{2n} \leq 0$. For $\beta < -1$, as long as α is not too negative, there are two extrema as a function of x : the boundaries $x = \pm 1$ are local minima (M) and a maximum (A_1) lies between $x = 0$ and $x = 1$. However, if α is reduced until $(3 + 16\alpha^2 - 8\alpha\beta)^3 = 27(1 - 4\alpha\beta)^2$, we find two additional local extrema; a minimum at A_2 and a maximum at A_0 . At $\beta = -1$, the $x = -1$ point bifurcates, and for $\beta > -1$ it is a local maximum and the local minimum (A_2) is found in the region $-1 < x < 0$. Illustrative plots are shown in figure 2.2(a).

Previous analyses [144, 145] show that the MC state M is always stable against density fluctuation, and is (thermodynamically and dynamically) stable against pairing fluctua-

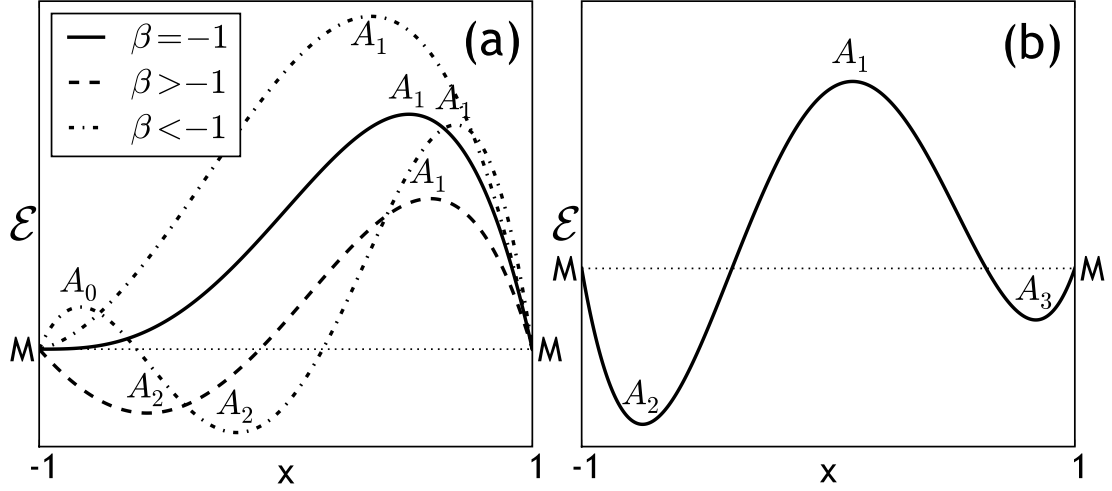


FIGURE 2.2: Scaled energy $\mathcal{E} = \langle F \rangle + (\mu - \epsilon/2)n$ versus molecular condensate order parameter $x = \phi_m \sqrt{2/n}$ for fixed n . The energy has been shifted so that the molecular state M has $\mathcal{E} = 0$. (a) $\lambda_m = \lambda_{am} = 0$: curves show $-\epsilon > 2g\sqrt{2n}$ ($\beta < -1$), $-\epsilon < 2g\sqrt{2n}$ ($\beta > -1$), and $-\epsilon = 2g\sqrt{2n}$ ($\beta = -1$). For $\beta < -1$ there are two sub-cases: either a single stationary point (A_1) or three stationary points (A_0 , A_1 and A_2). (b) $\lambda_m, \lambda_{am} \neq 0$: A_3 does not exist if both of them are zero.

tions if and only if $\beta < -1$.

Thermodynamic stability of the ASF is explored by calculating the Hessian $H_{ij} = \partial^2 \mathcal{E} / \partial i \partial j$, where $i, j = x, n$. Using the condition $\partial \mathcal{E} / \partial x = 0$, these derivatives can be written as $H_{xx} = n[\epsilon + 2\lambda_a(4n_m - n_a) - 12g\phi_m]$, $H_{xn} = H_{nx} = [g(4n_m - n_a) - 2\epsilon\phi_m] / \sqrt{2n}$, $H_{nn} = n_a(2n_a\lambda_a + 3g\phi_m) / (2n^2)$. The determinant of the Hessian (the discriminant) is related to the compressibility, $\partial\mu/\partial n = (H_{nn}H_{xx} - H_{nx}^2) / H_{xx}$. For A_2 the discriminant is always negative, while for A_1 and A_0 it is negative for $\lambda\epsilon > 2g^2$ and otherwise positive. Thus A_2 , which is always stable against pairing fluctuations ($H_{xx} > 0$), is always thermodynamically unstable towards density fluctuations (i.e. has a negative compressibility). Similarly A_1 and A_0 are always thermodynamically unstable against pairing fluctuations ($H_{xx} < 0$), and are thermodynamically unstable against density fluctuations if and only if $\lambda\epsilon > 2g^2$.

Dynamical stability is explored by calculating the equations of motion for the fluctua-

tions. We write the field operators in terms of density fluctuation $\hat{\rho}(r)$, pairing fluctuation $\hat{y}(r)$, relative phase fluctuation $\hat{\chi}(r)$, and total phase fluctuation $\hat{\theta}(r)$.

$$\begin{aligned}\hat{\psi}_m(r) &= \sqrt{\frac{n + \hat{\rho}(r)}{2}} [x + \hat{y}(r)] e^{2i[\hat{\theta}(r) + \xi + \hat{\chi}(r)]} \\ \hat{\psi}_a(r) &= \sqrt{n + \hat{\rho}(r)} \sqrt{1 - (x + \hat{y}(r))^2} e^{i[\hat{\theta}(r) - \xi - \hat{\chi}(r)]}\end{aligned}\quad (2.3)$$

The equations of motion are found by making stationary the action

$$S = \int i\hat{\psi}_a^\dagger \partial_t \hat{\psi}_a + i\hat{\psi}_m^\dagger \partial_t \hat{\psi}_m - \mathcal{F} \quad (2.4)$$

Working to quadratic order in the fluctuations, we find

$$\begin{aligned}\dot{\rho}_k &= \frac{n}{m} k^2 \theta_k - \frac{nu}{m} k^2 \chi_k \\ u\dot{\rho}_k - 4nx\dot{y}_k &= \frac{nu}{m} k^2 \theta_k - \left[\frac{n}{m} k^2 + H_{\xi\xi} \right] \chi_k \\ nx\dot{\chi}_k &= [vk^2 - H_{nx}] \frac{\rho_k}{4} - \left[\frac{n(3x^2 + 1)}{4m(1 - x^2)} k^2 + H_{xx} \right] \frac{y_k}{4} \\ \dot{\theta}_k - u\dot{\chi}_k &= \left[\frac{3x^2 - 4}{16mn} k^2 - H_{nn} \right] \rho_k + [vk^2 - H_{nx}] y_k\end{aligned}\quad (2.5)$$

where $H_{\xi\xi} = -16\sqrt{2n^3}gx(1 - x^2)$, $u = 1 - 2x^2$, $v = 3x/8m$, $\dot{a} \equiv \partial_t a$ and the Fourier components of the fluctuation operators are defined by $O(r) = \sum_k O_k e^{ikr}$. As $k \rightarrow 0$ the density and pairing modes decouple, and their frequencies are

$$\begin{aligned}\omega_{\text{density}}^2 &= c_s^2 k^2 + O(k^4) \\ \omega_{\text{pair}}^2 &= \Delta^2 + O(k^2)\end{aligned}\quad (2.6)$$

where the speed of sound is related to the compressibility by the standard expression $c_s^2 = (n/m)\partial\mu/\partial n$, and the gap to pairing excitation is $\Delta^2 = H_{xx}H_{\xi\xi}/16n^2x^2$. Since $H_{\xi\xi} \propto -x$, A_1 and A_2 are dynamically stable against long wavelength pairing fluctuations, while A_0 is unstable. Conversely, we see a long wavelength dynamic instability towards density fluctuations if and only if a thermodynamic instability exists.

In the special case where $\lambda_a = 0$, Timmermans et al. investigated these same collective modes [149]. Our results reduce to theirs when we set $\lambda_a = 0$. We note, however, that

Timmermans et al. found that for some parameter ranges the long wavelength modes were stable, but shorter wavelength modes become unstable. Thus we expect that some of the regions which we report as being metastable may possess finite k dynamical instabilities.

For any given set of parameter values, it is straightforward to check to see if there are any finite k instabilities: Eq. (2.5) gives an analytic expression for the entire spectrum. On the other hand, it is a difficult task to produce a closed form expression for when a finite wave-vector instability occurs, and we have been unable to produce a particularly enlightening expression (except for when $\lambda_a = 0$).

2.3 Effect of non-zero λ_m and λ_{am}

We have seen that in the absence of λ_{am} and λ_m there is no stable ASF, and the metastable ASF always has larger energy than the MSF. Hence there is no MSF \leftrightarrow ASF phase transition. We now show the existence of a continuous MSF \leftrightarrow ASF phase transition when $\lambda_m > 0$. To produce such a continuous phase transition it is necessary and sufficient to show that there exists a stable ASF, with arbitrarily small atomic fraction, at the point the MSF becomes destabilized. In the presence of a non-zero λ_m and λ_{am} figure 2.2(b) represents the generic structure of \mathcal{E} ; two minima at A_2 and A_3 and a maximum at A_1 . In terms of dimensionless parameters $\gamma = \lambda_m \sqrt{n/2}/8g$ and $\eta = \lambda_{am} \sqrt{n/2}/2g$, $A_{2,3}$ appears at $x = \mp 1$ when $\beta + 2\gamma - \eta = \mp 1$, where the upper signs correspond to A_2 and the lower signs correspond to A_3 .

The compressibility at $x = \mp 1$ when $A_{2,3}$ first appears is proportional to $16\alpha\gamma - (1 \mp 2\eta)^2$. So neither ASF is stable if $\gamma = 0$, i.e., even when $\lambda_{am} \neq 0$, a continuous MSF \leftrightarrow ASF phase transition cannot exist if $\lambda_m = 0$.

The curvature (H_{xx}) at $x = \mp 1$ when $A_{2,3}$ first appears is proportional to $\pm 1 + 2(\alpha + \gamma - \eta)$. At A_3 , $H_{\xi\xi} \propto -x$ is negative, and therefore $\Delta^2 \propto H_{xx}H_{\xi\xi}$ is negative whenever $H_{xx} > 0$; i.e., A_3 is always either dynamically or thermodynamically unstable against pairing fluctuations. The dynamical instability of A_3 even when $H_{xx} > 0$ can be understood as instability against fluctuations in ξ , i.e., in the $x - \xi$ plane, the energy has a saddle-point at A_3 (recall that 4ξ is the relative phase between the atomic and molecular components). At A_2 , however, $H_{xx} > 0$ is equivalent to $\Delta^2 \propto H_{xx}H_{\xi\xi} > 0$.

When the atom-molecule scattering vanishes ($\eta = 0$), the stability conditions at A_2 , viz. $H_{xx} > 0$ and $\partial\mu/\partial n > 0$ are simultaneously satisfied if and only if $\gamma > 0$ and $16\alpha\gamma > 1$. Thus there exists an MSF \leftrightarrow ASF continuous phase transition when $\lambda_{am} = 0$ if and only if $n\lambda_a\lambda_m > 2g^2$ and $\lambda_m > 0$.

The general criterion for the existence of a continuous MSF \leftrightarrow ASF phase transition when $\lambda_m \neq 0$, $\lambda_{am} \neq 0$ can be worked out in the $\lambda_m - \lambda_{am}$ space from the conditions $16\alpha\gamma > (1 - 2\eta)^2$ and $1 + 2(\alpha + \gamma - \eta) > 0$.

2.4 Stationary States (fixed chemical potential)

Working at fixed chemical potential (and taking $\lambda_{am} = 0$), there are two type of stationary points of Eq. (2.1); an MSF: $\phi_a = 0$, $\phi_m^2 = (2\mu - \epsilon)/\lambda_m$, and an ASF: $\lambda_a\lambda_m\phi_m^3 + (\lambda_a(\epsilon - 2\mu) - 2g^2)\phi_m + \mu g = 0$, $\phi_a^2 = (\mu - 2g\phi_m)/\lambda_a$. The ASF equation has three solutions, one of which can be ruled out on the basis of having a negative density (the topmost dotted line in figure 2.3). Stability analysis is done for both ASF and MSF states by considering fluctuations in ϕ_m , ϕ_m^* , ϕ_a and ϕ_a^* , analogous to Eq. (2.5). The corresponding dynamical

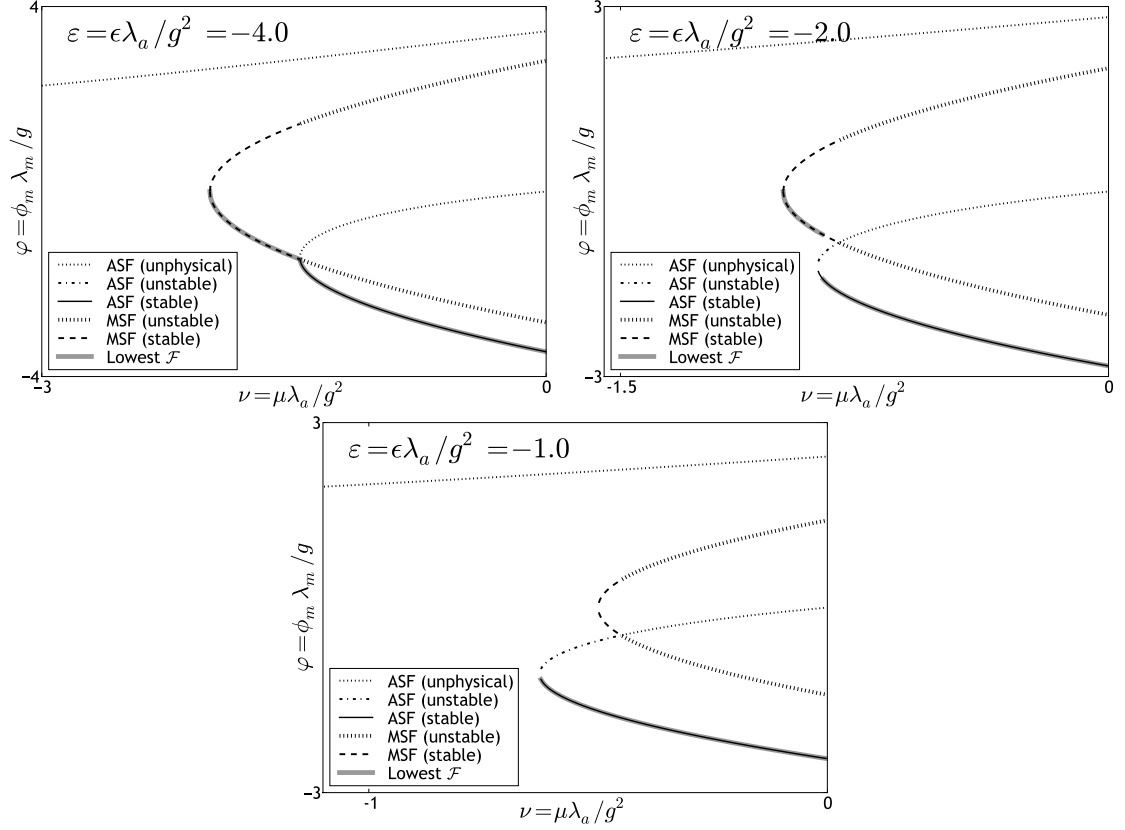


FIGURE 2.3: Stationary points of \mathcal{F} , calculated with $\lambda_m = 2\lambda_a$. (a) For $\epsilon = -4$ (below the tricritical point), as ν is increased from a negative value to 0, first the MSF turns stable, and then there is a continuous phase transition to the ASF (the thick gray line, which is the stable state with the lowest free energy, is continuous), which appears and becomes stable. (b) For $\epsilon = -2$ (above the tricritical point), the ASF turns stable before the MSF becomes unstable, and there is a discontinuous phase transition when their energies are equal (thick gray line is discontinuous). (c) Finally, for $\epsilon = -1$, a stable ASF appears first from vacuum, and it has the lowest energy throughout; so there are no further transitions.

equations are

$$\begin{aligned}
 i\partial_t \delta\psi_a &= \left(-\frac{1}{2m} \nabla^2 - \mu + 2\lambda_a |\psi_a|^2 \right) \delta\psi_a \\
 &\quad + (\lambda_a \psi_a^2 + 2g\psi_m) \delta\psi_a^* + 2g\psi_a^* \delta\psi_m \\
 i\partial_t \delta\psi_m &= \left(\epsilon - 2\mu - \frac{1}{4m} \nabla^2 + 2\lambda_m |\psi_m|^2 \right) \delta\psi_m \\
 &\quad + 2g\psi_a \delta\psi_a + \lambda_m \psi_m^2 \delta\psi_m^*
 \end{aligned} \tag{2.7}$$

In terms of dimensionless quantities $\varphi = \phi_m \lambda_m / g$, $r = \lambda_m / \lambda_a$, $\epsilon = \epsilon \lambda_a / g^2$ and $\nu = \mu \lambda_a / g^2$, the MSF solution first appears at $2\nu = \epsilon$ and is stable for $\nu < (4 - 2\sqrt{4 - \epsilon r}) / r$ (where

the dashed lines in figure 2.3 end). The two physical ASF solutions exist for $v > v_c$ where $4(\varepsilon - 2v_c - 2)^3 + 27v_c^2r = 0$; one of them is always stable (thin solid line in, e.g., figure 2.3(b)), the other is stable for $v > 0$. The ASF \leftrightarrow MSF tricritical point is obtained by demanding that the two physical ASF solutions appear exactly when the MSF destabilizes. Mathematically,

$$\begin{aligned}
4(\varepsilon - 2v - 2)^3 + 27v^2r &= 0 \\
\varphi^3 + \varphi r(\varepsilon - 2v - 2) + vr^2 &= 0 \\
\varphi^2 - r(2v - \varepsilon) &= 0,
\end{aligned} \tag{2.8}$$

where the first equation is the condition for the appearance of physical ASF solutions, the second sets φ , and the third is the condition for the destabilization of the MSF. Solving these three simultaneously gives the tricritical point $v_{tc} = -2/\sqrt{r}$ and $\varepsilon_{tc} = -1 - 4/\sqrt{r}$; r therefore uniquely determining the phase diagram. Coupled with $n = 2\phi_m^2 = 2(2\mu - \varepsilon)/\lambda_m$, this yields the familiar result $n\lambda_a\lambda_m = 2g^2$.

2.5 Discussion

We have shown that a continuous ASF \leftrightarrow MSF phase transition can occur at sufficiently high density in a Bose gas near a Feshbach resonance with repulsive molecule-molecule interaction. This ASF does not, however, correspond to the phase currently studied in cold atom experiments. The experimental “phase” is a saddle point of the free energy, and always has a higher energy than the MSF.

The most obvious route to studying this transition would involve first creating an MSF (for instance, using the technique of Xu *et al* [147]), then slowly ramping toward the resonance (making $|e|$ smaller). As pointed out by previous authors [144, 145] the transition could be detected by observing the behavior of vortices.

We caution that this transition does not occur at arbitrarily low densities, nor in the absence of molecule-molecule scattering. Estimating $\lambda_m \sim 4\pi\hbar^2 a_s/2m$ far from resonance, and using $g^2 \sim (4\pi\hbar^2/m)a_{\text{bg}}\Delta\mu\Delta B$ as in [152], we see that in current experiments [47, 49, 147] use samples which are too dilute to observe the transition. Increasing the density further is made problematic by three-body relaxation [153]. In fact, estimating the time scale of three-body recombinations[154] to be $\tau_{3\text{-body}} \sim m/\hbar a_s^4 n^2$ with $a_s = \hbar/\sqrt{m\epsilon_c}$ (ϵ_c being binding energy for the transition) and $n = 2g^2/\lambda_a\lambda_m$ already gives $\tau_{3\text{-body}} \sim 10^{-4}\text{s}$. Quantum interference effects can drastically reduce this decay rate, but only at particular binding energies set by the locations of Efimov states [154]. We fear that one would need particularly fortuitous circumstances for these interference effects to provide sufficient reduction in the decay rate. Using a photoassociation transition in lieu of Feshbach resonance may provide enough control over the parameters of the system to avoid these difficulties[155].

CHAPTER 3

EQUATION OF STATE OF SPIN-POLARIZED FERMIONS

This chapter represents unpublished work. Some of the results have been presented in [156].

3.1 Introduction

Here we address the equation of state of the $T = 0$ normal state of a two-component spin-polarized Fermi gas. This equation of state is directly observable in experiments by measuring the densities of the two species as a function of position in a trap. In 2006, two groups loaded a trap with spin-polarized mixtures of ${}^6\text{Li}$ in the two lowest hyperfine states [74, 125]. The MIT group [126, 157] observed a “three-shell structure” with a fully paired superfluid (SF) core, surrounded by a “paired superfluid”¹, surrounded by a fully polarized normal fluid. Here we will try to calculate the phase boundary between a paired SF and a polarized normal fluid. The following calculation is at $T = 0$ and will mostly be at unitarity, i.e., $|a_s| \rightarrow \infty$, but it is straightforward to extend it to a finite a_s (two-particle scattering length).

We find that a spin-imbalanced mixture of up and down spin Fermions becomes completely polarized at $\mu_\downarrow \leq -0.9\mu_\uparrow$. We also find that such a mixture becomes dynamically unstable for $n_\downarrow/n_\uparrow > 0.006$. Neither of these numbers agree with experimental findings except for the order of magnitude, and both discrepancies can be traced to the over-estimation of interaction effects in the Nozières Schmitt-Rink formulation.

¹The structure of this phase is still debated, i.e., whether it is simply a homogeneous mixture of SF and normal fluid, or whether there are other novel phases (such as FFLO) hidden there.

3.2 Formulation of the free energy

As a function of population imbalance, there is a phase transition between a BCS-paired superfluid phase and the normal phase. At sufficiently low temperature, this transition is first order, as shown in appendix B. We calculate the free energies of both the phases, and the phase boundary is the manifold on which they are equal. We begin with the polarized normal phase. For a Hamiltonian of the form

$$\mathcal{H} = \sum_{\mathbf{p},\sigma} \epsilon_{\mathbf{p}} C_{\mathbf{p},\sigma}^\dagger C_{\mathbf{p},\sigma} - U \sum_{\mathbf{p},\mathbf{p}',\mathbf{q}} C_{\mathbf{p}+\mathbf{q}/2,\uparrow}^\dagger C_{-\mathbf{p}+\mathbf{q}/2,\downarrow}^\dagger C_{-\mathbf{p}'+\mathbf{q}/2,\downarrow} C_{\mathbf{p}'+\mathbf{q}/2,\uparrow} \quad (3.1)$$

the interaction correction to free energy Ω is approximated by[13]

$$\Delta\Omega = \text{Diagram 1} - \frac{1}{2} \text{Diagram 2} + \frac{1}{3} \text{Diagram 3} - \dots \quad (3.2)$$

where Ω is defined by

$$e^{-\beta\Omega} = \text{Tr} e^{-\beta\mathcal{H}} \quad (3.3)$$

This approximation is valid in the dilute limit on both sides of a Feshbach resonance ($a_s \rightarrow \pm 0$ or $|a_s k_F| \ll 1$). We do not expect this approximation to be quantitatively accurate in the strong coupling limit ($-1 < 1/a_s k_F < 1$), but as a function that interpolates between the exact BEC and BCS results, we might expect $\Delta\Omega$ to be off by at most a small factor near unitarity. The dashed lines are interaction lines, and the usual Feynman rules apply. For the form of our interaction, the inner and outer Fermion lines must have different spins. To evaluate this series, we define a scattering matrix Γ as

$$\Gamma = \text{Diagram 1} = \text{Diagram 2} + \text{Diagram 3} + \dots \quad (3.4)$$

where the top and bottom Fermion lines have opposite spins. The change in free energy $\Delta\Omega$ is given by[13]

$$\Delta\Omega = -\frac{1}{\pi} \sum_{\mathbf{q}} \int_{-\infty}^{\infty} d\nu g(\nu) [\delta(\mathbf{q}, \nu) - \delta(\mathbf{q}, 0)] \quad (3.5)$$

$$\delta(\mathbf{q}, \nu) = \arg \Gamma(\mathbf{q}, \nu)$$

where $g(\nu) = (e^{\beta\nu} - 1)^{-1}$ is the Bose-Einstein distribution function.

It turns out that Γ is a function of only the *sum* of the incoming momenta and frequencies, and in particular if the incoming momenta are $(p + q/2, -p + q/2)$ and the outgoing momenta are $(p' + q/2, -p' + q/2)$ (where $p \equiv (\mathbf{p}, i\omega_n)$), then the scattering matrix is given by

$$\Gamma(p + q/2, -p + q/2, p' + q/2, -p' + q/2) \equiv \Gamma(q) = \frac{-U}{1 - U\Theta(q)} \quad (3.6)$$

where Θ is the two-particle propagator

$$\Theta(\mathbf{q}, i\nu_n) = \sum_{\mathbf{k}} \left\{ \frac{1 - f(\epsilon_{\frac{\mathbf{q}}{2} + \mathbf{k}} - \mu_{\uparrow} + \Sigma_{\uparrow}) - f(\epsilon_{\frac{\mathbf{q}}{2} - \mathbf{k}} - \mu_{\downarrow} + \Sigma_{\downarrow})}{\epsilon_{\frac{\mathbf{q}}{2} + \mathbf{k}} + \epsilon_{\frac{\mathbf{q}}{2} - \mathbf{k}} - i\nu_n - \mu_{\downarrow} - \mu_{\uparrow} + \Sigma_{\downarrow} + \Sigma_{\uparrow}} - \frac{1}{2\epsilon_{\mathbf{k}}} \right\} \quad (3.7)$$

and Σ_{σ} is the self-energy of a spin- σ particle. The subtraction of the divergent term in equation (3.7) follows from the relation between the scattering length and U ,

$$U = -\frac{4\pi a_s}{mV} + \sum_{\mathbf{k}} \frac{1}{2\epsilon_{\mathbf{k}}} \quad (3.8)$$

3.3 Calculating the scattering matrix

Calculating Γ is hard because the self-energies depend on Γ , and have to be determined self-consistently. For our first approximation; we fix the self-energies to their values at $\omega = 0$ and $k = k_{\text{F}}^{\sigma}$. At $T = 0$, the combination $\mu_{\sigma} - \Sigma_{\sigma}$ can be related to the population by

$$\frac{(k_{\text{F}}^{\sigma})^2}{2m} = \mu_{\sigma} - \Sigma_{\sigma}(k_{\text{F}}^{\sigma}) \quad \text{and} \quad k_{\text{F}}^{\sigma} = (6\pi^2 n_{\sigma})^{1/3} \quad (3.9)$$

so that the scattering matrix Γ is

$$\Gamma(q) = \frac{4\pi}{mV k_F^\uparrow} \frac{1}{(a_s k_F^\uparrow)^{-1} + \tilde{\Theta}(\tilde{q})} \quad (3.10)$$

where $\tilde{\Theta}$ is Θ in a dimensionless form. At $T = 0$ we find an analytic expression for equation (3.7), finding that the result depends only on the magnitude of \mathbf{q} and \mathbf{v} ,

$$\begin{aligned} \tilde{\Theta}(\tilde{q}, \tilde{v}) = & \frac{1}{2\pi} [2\pi i \zeta - 2(1+r)] \\ & - \frac{1}{2\pi} \left[\frac{1}{\tilde{q}} \left(\frac{1}{4} \tilde{q}^2 + \zeta^2 + \tilde{q}\zeta - 1 \right) \log \left(\frac{\tilde{q} + 2\zeta - 2}{\tilde{q} + 2\zeta + 2} \right) \right. \\ & + \frac{1}{\tilde{q}} \left(1 + \tilde{q}\zeta - \frac{1}{4} \tilde{q}^2 - \zeta^2 \right) \log \left(\frac{\tilde{q} - 2\zeta + 2}{\tilde{q} - 2\zeta - 2} \right) \\ & + \frac{1}{\tilde{q}} \left(\frac{1}{4} \tilde{q}^2 + \zeta^2 + \tilde{q}\zeta - r^2 \right) \log \left(\frac{\tilde{q} + 2\zeta - 2r}{\tilde{q} + 2\zeta + 2r} \right) \\ & \left. + \frac{1}{\tilde{q}} \left(r^2 + \tilde{q}\zeta - \frac{1}{4} \tilde{q}^2 - \zeta^2 \right) \log \left(\frac{\tilde{q} - 2\zeta + 2r}{\tilde{q} - 2\zeta - 2r} \right) \right] \end{aligned} \quad (3.11)$$

where

$$\tilde{q} = \frac{q}{k_F^\uparrow}; \quad r = \frac{k_F^\downarrow}{k_F^\uparrow}; \quad \tilde{v} = \frac{m\mathbf{v}}{(k_F^\uparrow)^2}; \quad \zeta = \tilde{v} + \frac{1}{2}(1+r^2) - \frac{1}{4}\tilde{q}^2 \quad (3.12)$$

When $\mu_\sigma - \Sigma_\sigma < 0$, we take $k_F^\sigma = 0$. The normal fluid is stable above some critical polarization, i.e., below some critical r . Remarkably, the (modified) Thouless criterion for a pairing instability,

$$\tilde{\Theta}(\tilde{q}, 0) + \frac{1}{a_s k_F^\uparrow} = 0 \quad (3.13)$$

is first satisfied for a *finite* q , at $r_c = 0.42$ at unitarity. This, however, corresponds to a spinodal, and this instability is preempted by a first order transition at some $r < r_c$.

3.4 Calculating the self energies

The self energies in (3.7), which relate k_F^σ and μ_σ according to (3.9), can be written down for the form of interaction (3.1) to be

$$\Sigma_\sigma(\mathbf{k}, i\omega_m) = \text{[diagram: a fermion line with a self-energy loop]} = \frac{1}{\beta} \sum_{\mathbf{q}} \sum_{i\omega_n} \Gamma(\mathbf{k} + \mathbf{q}, i\omega_m + i\omega_n) G_{-\sigma}(\mathbf{q}, i\omega_n) \quad (3.14)$$

where $G_{-\sigma}$ is the Green's function including the self-energy,

$$G_{-\sigma}(\mathbf{q}, i\omega_n) = \frac{1}{i\omega_n - \epsilon_{\mathbf{q}} + \mu_{-\sigma} - \Sigma_{-\sigma}(\mathbf{q}, i\omega_n)} \quad (3.15)$$

So the self energy has to be determined self-consistently. We again use our previous approximation, i.e., we fix the self-energies to their static values at the Fermi momenta. The Matsubara sum in (3.14) can be converted to a contour integral, and is evaluated in appendix H. The results are shown in figure 3.1. Of particular importance is the $r = 0$ point in figure 3.1 (right), which tells us that the down spin density vanishes when $\mu_\downarrow \approx -0.912\mu_\uparrow$. Experimental data[126] shows that $\mu_\downarrow \approx -0.5\mu_\uparrow$ when $n_\downarrow = 0$ ². This discrepancy is not surprising, given the difficulty of modeling the correlations in this strongly interacting gas, and later in the chapter we will discuss possible remedies.

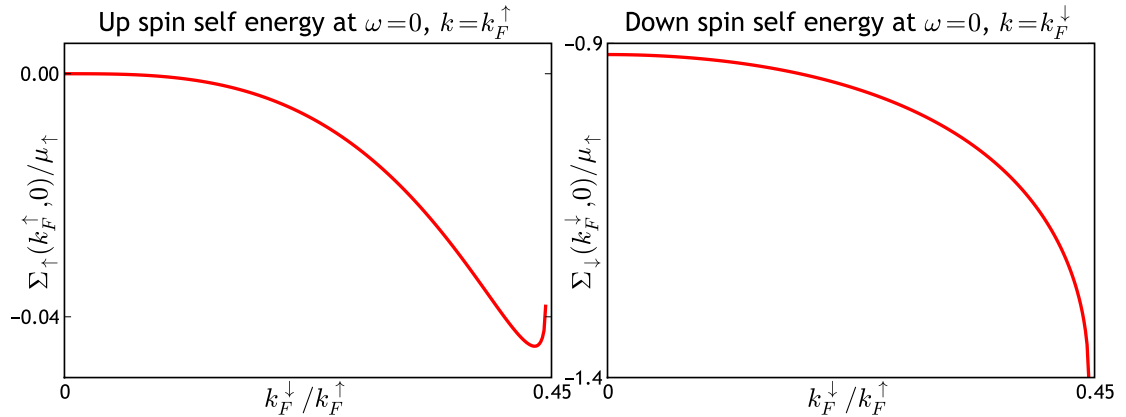


FIGURE 3.1: Up and down spin self energies as functions of r computed from eq. (H.4).

²Monte-Carlo simulations point to $\mu_\downarrow \approx -0.6\mu_\uparrow$ at vanishing n_\downarrow [158, 159].

3.5 Calculating the $T = 0$ free energy

We now calculate the free energy $\Omega = \Omega_0 + \Delta\Omega$. The noninteracting energy Ω_0 for a normal fluid is

$$e^{-\beta\Omega_0} = \prod_{\mathbf{k}} (1 + e^{\beta(\epsilon_{\mathbf{k}} - \mu_{\sigma})})$$

which at $T = 0$ reduces to

$$\frac{\Omega_0}{V} = \frac{\Omega_0^{\uparrow} + \Omega_0^{\downarrow}}{V} = -\frac{(k_F^{\uparrow})^5}{30m\pi^2} (1 + r^5) \quad (3.16)$$

One can prove from equations (3.6) and (3.7) that $\delta(\mathbf{q}, 0) = 0$. At $T = 0$ the Bose function in (3.5) contributes -1 for $v < 0$ and 0 otherwise. Scaling out the dimensioned quantities from eq. (3.5) we get

$$\frac{\Delta\Omega}{V} = \frac{1}{2\pi^3} \frac{(k_F^{\uparrow})^5}{m} \int_0^{\infty} q^2 dq \int_{-\infty}^0 d\omega \delta(q, \omega) \quad (3.17)$$

The phase shift is non-zero only if ζ as defined in (3.12) (with \tilde{v} replaced by ω) is positive, hence both the q and ω integrals are compact, with

$$\begin{aligned} \frac{\Delta\Omega}{V} &= \frac{1}{2\pi^3} \frac{(k_F^{\uparrow})^5}{m} \int_0^{\sqrt{2(1+r^2)}} q^2 dq \int_{-\frac{1}{2}(1+r^2)}^0 d\omega \delta(q, \omega) \\ \Rightarrow \frac{30m\pi^2}{(k_F^{\uparrow})^5} \left(\frac{\Omega_N}{V} \right) &= -(1 + r^5) + \frac{15}{\pi} \int_0^{\sqrt{2(1+r^2)}} q^2 dq \int_{-\frac{1}{2}(1+r^2)}^0 d\omega \delta(q, \omega) \end{aligned} \quad (3.18)$$

where Ω_N is the total free energy of the normal phase. For the fully paired superfluid phase at unitarity, the free energy is known exactly. Dimensional analysis forces it to have the form

$$\frac{\Omega_S}{V} = -\frac{1}{15\pi^2} \left(\frac{m}{1 + \beta} \right)^{3/2} (\mu_{\uparrow} + \mu_{\downarrow})^{5/2} \quad (3.19)$$

The universal parameter β is found to be $\beta \approx -0.545$ from QMC calculations [160] and $\beta \approx -0.41$ using mean-field BCS theory. Ω_N/V and Ω_S/V are plotted³ in figure 3.2 as a

³Since Ω_N is known in terms of k_F^{σ} and Ω_S is known in terms of μ_{σ} , this is not very straightforward. We vary $r = k_F^{\downarrow}/k_F^{\uparrow}$ in the range (0,0.42) and calculate Ω_N from (3.18). To calculate Ω_S according to (3.19), we first calculate μ_{\uparrow} and μ_{\downarrow} from (3.9) and figure 3.1. All the free energies in figure 3.2 appear double valued over some range, because $\mu_{\downarrow}/(\mu_{\uparrow} - \mu_{\downarrow})$ is non-monotonic in r .

function of μ_{\downarrow} ; the scaling factor $\mu_{\uparrow} - \mu_{\downarrow}$ is constant throughout a trapped gas in experiments.

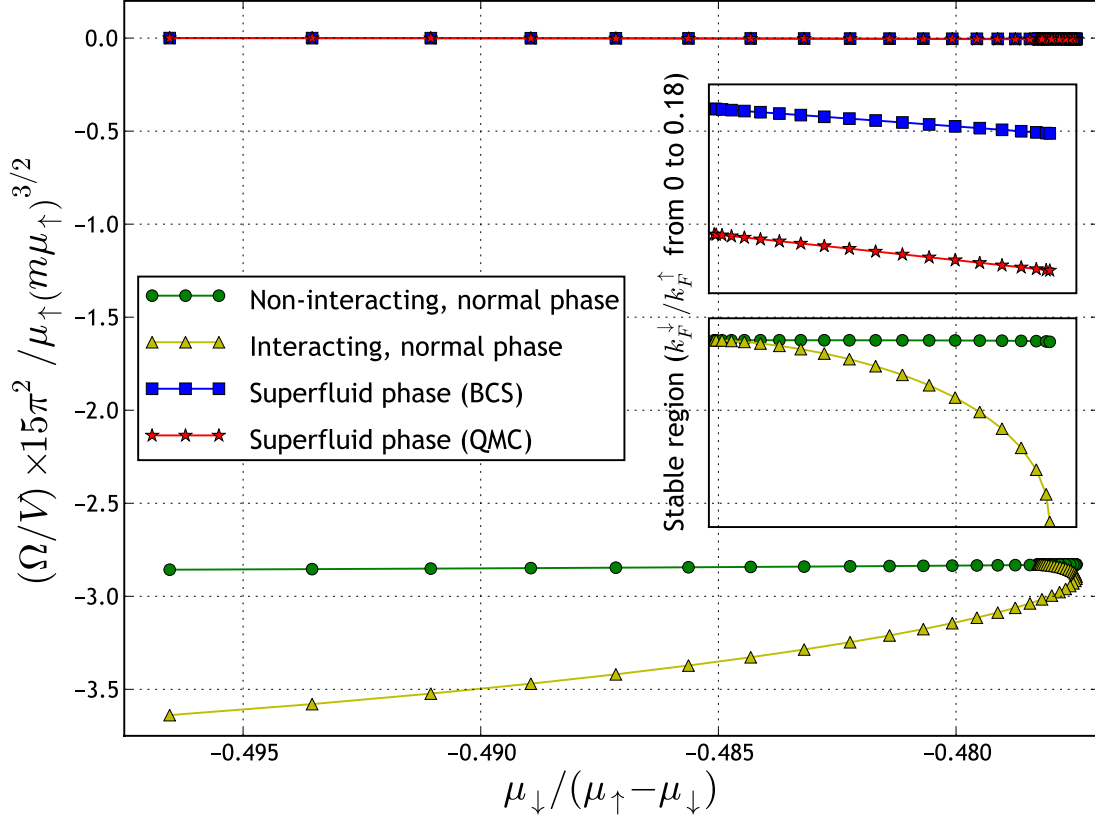


FIGURE 3.2: Free energy plots; the normal phase seems to always win.

Within our approximations, the SF phase always has higher energy, and we conclude that the T-matrix approximation underestimates the energy of the normal state. One can get an upper bound on the normal state energy by neglecting interactions, in which case the SF phase has a lower energy after some point (figure 3.3). With interactions, the normal state becomes mechanically unstable before reaching that point.

To investigate the mechanical stability of the normal state, we calculate the compress-

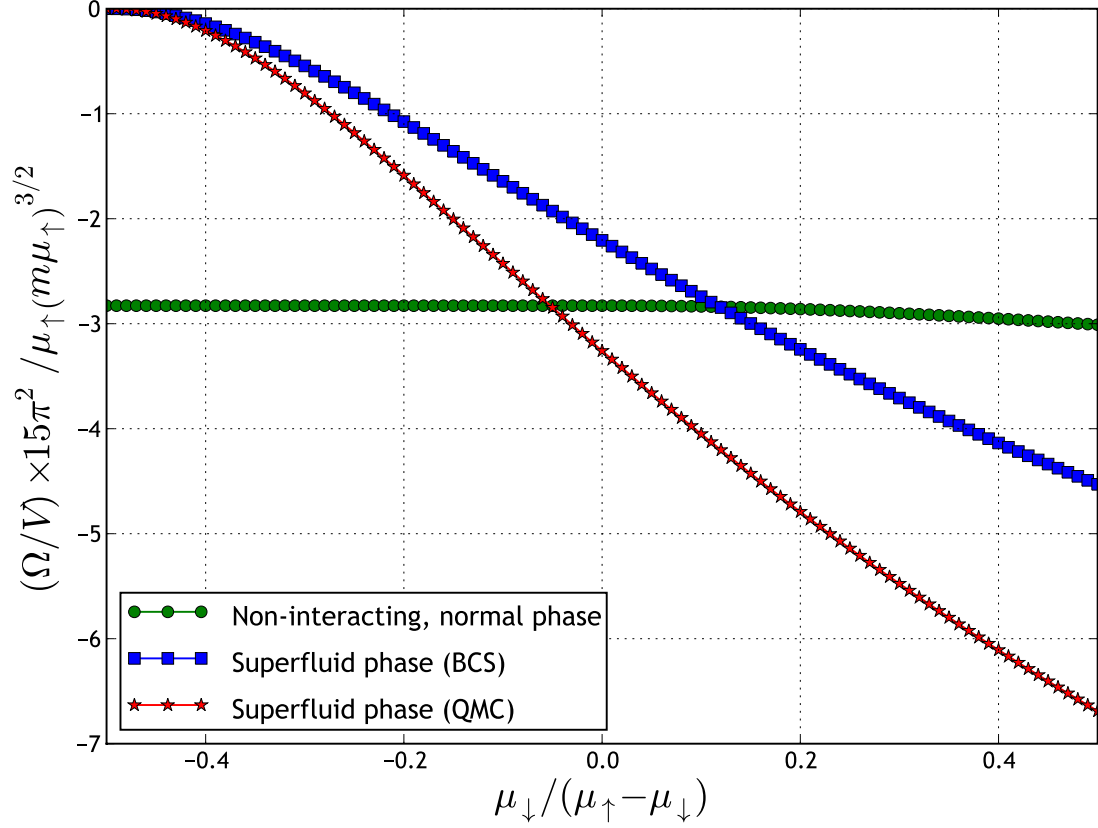


FIGURE 3.3: Free energy plots for the non-interacting model. The green curve provides an upper bound for the energy of the normal state. The SF wins after some point.

stability matrix $\partial\mu/\partial n$,

$$\frac{\partial\mu}{\partial n} = \begin{pmatrix} \frac{\partial\mu_{\uparrow}}{\partial n_{\uparrow}} & \frac{\partial\mu_{\uparrow}}{\partial n_{\downarrow}} \\ \frac{\partial\mu_{\downarrow}}{\partial n_{\uparrow}} & \frac{\partial\mu_{\downarrow}}{\partial n_{\downarrow}} \end{pmatrix} \quad (3.20)$$

This matrix ceases to be positive definite for $k_F^{\downarrow}/k_F^{\uparrow} \gtrsim 0.184$ as shown in figure 3.4 (right). The polarization of this instability corresponds to the density ratio $n_{\downarrow}/n_{\uparrow} \approx 0.006$, which is much smaller than the experimentally observed [126]

$$\frac{n_{\downarrow}}{n_{\uparrow}} \approx 0.13$$

This discrepancy highlights a major problem with the T-matrix approach.

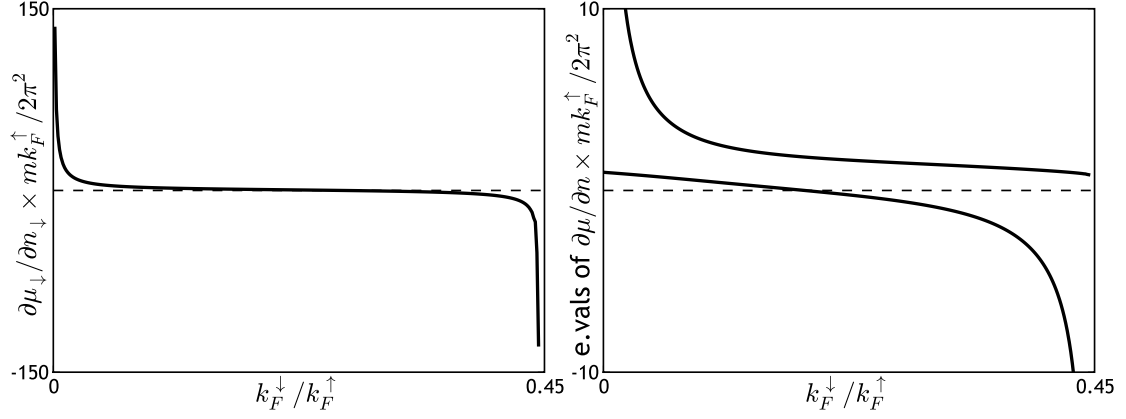


FIGURE 3.4: **Left:** The down spin compressibility $(\partial\mu_\downarrow/\partial n_\downarrow) < 0$ after $k_F^\downarrow/k_F^\uparrow \approx 0.265$. **Right:** Eigenvalues of the compressibility matrix $\partial[\mu]/\partial[n]$. One of the eigenvalues becomes negative after $k_F^\downarrow/k_F^\uparrow \approx 0.184$.

3.6 Concluding remarks

A naïve calculation without self-energies suggests that the down-spin density vanishes at $\mu_\downarrow/\mu_\uparrow = 0$, while a self-consistent self energy calculation suggests that it vanishes at $\mu_\downarrow/\mu_\uparrow \approx -0.912$; the experimental value of ~ -0.5 is somewhere in between. Further, another naïve calculation without interaction effects (figure 3.3) gives a reasonable value for when the SF phase has a lower energy, i.e., the radius of the SF core is predicted to be non-zero, while this calculation with interaction effects (figure 3.2) says that the SF phase *never* wins. And finally, this calculation predicts a dynamical instability at a very low polarization (figure 3.4, right), which is not seen in practice. All three artefacts can be traced to the over-estimation of the attractive interaction; the self-energies calculated from eqs. (H.4) are simply too negative to match experiments.

The approximation of replacing the self-energies by their values at the Fermi surface is not too bad, since it is seen that they vary only by a few percents over the entire momentum range. On the other hand, a static approximation for the self energies, i.e., using their values at $\omega = 0$, is not all that good, since they do vary considerably with ω . On the

SF side, however, this static approximation gives excellent agreement with experiments at unitarity[161, 162], hence it is not very obvious that including the frequency dependence on the normal fluid side will solve all our ills.

This discrepancy can be marginally improved by adding effective mass corrections. The curvature of $\Sigma_{\downarrow}(k, 0)$ versus k gives an effective mass correction Δm_{\downarrow} , where the effective mass $m^* = m\Delta m_{\downarrow}/(m + \Delta m_{\downarrow})$. Adding this to the scattering matrix calculation yields $\mu_{\downarrow} = -0.85\mu_{\uparrow}$, which is slightly better.

Some theorists have suggested, based on earlier work on superconductors, that dressing both up and down spin propagators with their respective self energies does not capture interaction effects accurately [163]. Instead, one should use

$$\Theta(\mathbf{K}) = \sum_{\mathbf{P}} G_{0\sigma}(\mathbf{K} - \mathbf{P})G_{-\sigma}(\mathbf{P})$$

Since we're working at vanishing down spin density, our approach automatically boils down to the case $\sigma = \uparrow$, which clearly does not yield an accurate results, and it's not obvious why one should use $\sigma = \downarrow$. Symmetric extensions of this idea, such as

$$\Theta(\mathbf{K}) = \frac{1}{2} [\Theta_{\uparrow\downarrow}(\mathbf{K}) + \Theta_{\downarrow\uparrow}(\mathbf{K})]$$

$$\Theta_{\uparrow\downarrow}(\mathbf{K}) = \sum_{\mathbf{P}} G_{0\uparrow}(\mathbf{K} - \mathbf{P})G_{\downarrow}(\mathbf{P})$$

$$\Theta_{\downarrow\uparrow}(\mathbf{K}) = \sum_{\mathbf{P}} G_{0\downarrow}(\mathbf{K} - \mathbf{P})G_{\uparrow}(\mathbf{P})$$

have also been proposed [164], although justifying such a choice starting from the equations of motion is not straightforward at best.

It is interesting to note that a non-self consistent calculation, i.e., using bare propagators to evaluate Θ , yields $\mu_{\downarrow} = -0.6\mu_{\uparrow}$ [165], which is close to Monte-Carlo simulations [158, 159]. This is effectively a summation of a subset of diagrams, and the choice of this particular subset is hard to justify, especially in the absence of small parameters near unitarity [166].

CHAPTER 4

SURFACE TENSION AT A SUPERFLUID-NORMAL INTERFACE

This chapter represents the author's contribution to "Theory of the Normal/Superfluid interface in population imbalanced Fermi gases" by Stefan K. Baur, Sourish Basu, Erich J. Mueller and Theja N. De Silva [156]. The article has been recently accepted for publication in Physical Review A.

4.1 Introduction

What happens when one tries to polarize a fermionic superfluid? Experiments at MIT [3, 125, 157] and Rice University [2, 74] have shown that when the fermions are interacting via resonant short range interactions, the fluid responds by phase separating into a largely unpolarized superfluid region and a less polarized normal region. The Rice experiments [2, 74] show a dramatic distortion of the central superfluid region in their trapped gas, pointing to significant surface tension in the boundary. In § 4.3 we present a phenomenological model for this boundary to estimate the magnitude of surface tension necessary to match experiments.

The phase separation seen in these experiments arises because a zero temperature conventional s-wave superfluid is unable to accommodate spin polarization: all of the atoms in one spin state (\uparrow) are paired with atoms of the opposite spin (\downarrow). Changing the density ratio $n_{\uparrow}/n_{\downarrow}$ from unity requires adding sufficient energy to break these pairs. Consequently, when excess particles of one spin state are added to a paired atomic cloud, those particles simply float to the "surface" at a lower chemical potential, forming a normal fluid. Given that there is a sharp boundary between the superfluid and normal region, the order parameter must vary rapidly, producing a surface energy. This surface energy

“barrier” is the microscopic cause behind surface tension. In § 4.4 we present a microscopic BCS-like model with point interactions to calculate this energy barrier and hence the surface tension.

It is worth noting that the work presented in the rest of this chapter is a slice of a longer paper [156]. The interested reader is advised to check it out for a more detailed description, including solutions of the Bogoliubov-de Gennes equations at an interface, and the effect of order parameter oscillations. The portion presented in this thesis is the author’s contribution to [156]. Work presented in § 4.3 was done in collaboration with Stefan Baur (first author of [156]), while § 4.4 is entirely the author’s original contribution.

4.2 Experimental data

Experiments at Rice [2, 74] were done with an extremely elongated cigar-shaped trap of aspect ratio of 45, and as such the effect of surface tension is very striking in the data. The

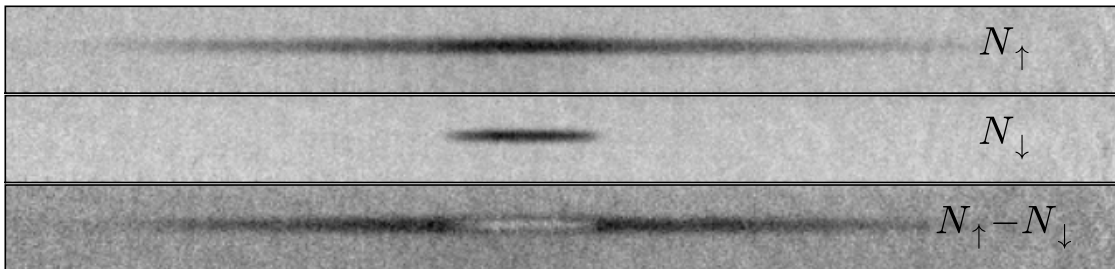


FIGURE 4.1: Experimental two-dimensional column densities (black denotes high density) for $P=0.6$, with majority atoms (\uparrow) at the top, minority atoms (\downarrow) in the middle, and their difference at the bottom. The superfluid core, which is where all the \downarrow -spins are, has a significantly different aspect ratio. The sensor is 512 pixels long (X-axis) by 40 pixels wide (Y-axis), where each pixel is $3.23 \mu\text{m}$. Data used from [2], with permission.

experimentalists took $\sim 150,000$ ${}^6\text{Li}$ atoms in an equal mixture of the two lowest hyperfine states, $|F = 1/2, m_F = \pm 1/2\rangle$. Then using an RF ramp, they spin-polarized the mixture to different values of $P = (N_{\uparrow} - N_{\downarrow}) / (N_{\uparrow} + N_{\downarrow})$. The system was allowed to equilibrate at

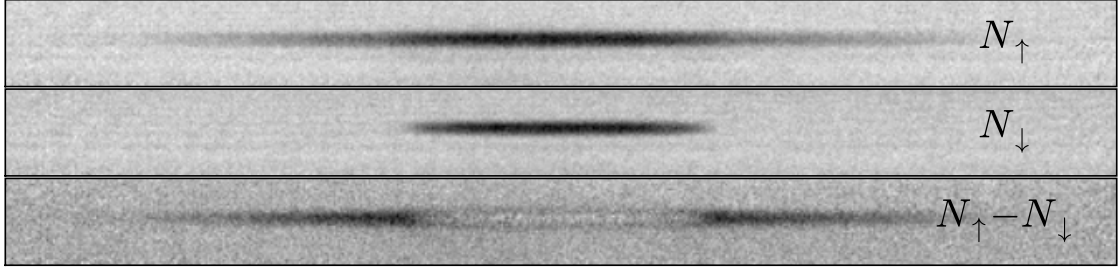


FIGURE 4.2: Very similar data to figure 4.1, except $P=0.37$. The difference in the aspect ratios is not as striking at this lower polarization. Data used from [2], with permission.

$T \ll T_F$ and 834 Gauss, where the two states have a 300 Gauss-wide Feshbach resonance. The 2-D densities were imaged optically (shown in figures 4.1 and 4.2).

At unitarity, the only relevant length scale is the interparticle spacing $n^{-1/3}$, which is $\sim 1 \mu\text{m}$. This is much less than the extent of the cloud in either direction, so local density approximation (LDA) should be quite good at predicting the spin densities as functions of the local chemical potentials,

$$\mu_{\uparrow,\downarrow}(r, z) = \mu_{\uparrow,\downarrow}(0, 0) - \frac{m}{2}(\omega_r^2 r^2 + \omega_z^2 z^2)$$

where z is the long axis of the azimuthally symmetric trap. By this logic, isopycnal contours should follow equipotential contours, which clearly does not hold for the \downarrow -spins in figures 4.1 and 4.2. This points to some surface tension between the superfluid core and the normal shell.

4.3 Phenomenological model

To construct a phenomenological model of surface tension, we assume that the zero temperature population imbalanced atomic system is phase separated into two regions: a central superfluid core surrounded by a normal shell. We take the normal state to be fully polarized (with $n_{\downarrow} = 0$) and the superfluid state to be fully paired ($n_{\uparrow} = n_{\downarrow}$). Although

this is an approximation, the experiments at Rice[2, 74] are largely consistent with this ansatz, first introduced by Chevy [124].

We restrict our discussion to unitarity, where the physics is universal and the superfluid and surface energy densities between the superfluid and normal regions have simple forms. The equation of state of the central superfluid shell is given at $T = 0$ by

$$n_s(\mu) = n_\uparrow + n_\downarrow = \frac{1}{3\pi^2} \left[\frac{2m}{\hbar^2(1+\beta)} \mu \right]^{3/2} \quad (4.1)$$

where μ is the average chemical potential and β is a dimensionless universal many body parameter [112, 167–169]. According to quantum Monte-Carlo calculations $\beta \approx -0.58$ [160, 170–173] while BCS theory gives $\beta = -0.42$. The outer fully polarized normal shell obeys

$$n_n(\mathbf{r}) = n_\uparrow = \frac{1}{6\pi^2} \left[\frac{2m\mu_n(\mathbf{r})}{\hbar^2} \right]^{3/2}. \quad (4.2)$$

The free energy densities of the bulk phases $f_{s,n} = -\int n_{s,n} d\mu$ can be written as

$$f_{s,n}(\mathbf{r}) = -\frac{2}{15\pi^2} \left(\frac{2m}{\hbar^2} \right)^{3/2} \zeta_{s,n} \mu_{s,n}^{5/2}(\mathbf{r}) \quad (4.3)$$

where $\zeta_s = 1/(1+\beta)^{3/2}$, $\zeta_n = 1/2$. Then we calculate the total bulk energies $\Omega_{S,N} = \int_{s/n} d^3\mathbf{r} f_{s,n}[\mu(\mathbf{r}), h]$ by integrating the bulk energy densities over the superfluid/normal regions. The surface tension has dimensions of energy per unit area, and since at unitarity the only energy scale is $\hbar^2 n^{2/3}/m$ and the only length scale is $n^{-1/3}$, the surface tension σ must be, by dimensional analysis,

$$\sigma = \frac{\hbar^2 n_s^{4/3}}{2m} \eta(\delta P/P) \quad (4.4)$$

where the dimensionless parameter η is a function of the pressure drop δP across the interface. In the experiments, $\delta P/P \ll 1$ [174], so we approximate $\eta(\delta P/P)$ by $\eta = \eta(0)$. We calculate the total surface energy $E_{dw} = \int d^2r \sigma[\mu(\mathbf{r}), h]$ by integrating the surface energy density over the superfluid-normal boundary. Away from the superfluid-normal

boundary, we assume that the system is locally homogenous and the external harmonic trapping potential $V_{\text{trap}}(\mathbf{r}) = b_{\perp}\rho^2 + b_z z^2 = m\omega_z^2(\lambda^2\rho^2 + z^2)/2$ is treated in the LDA by introducing a local chemical potential $\mu(\mathbf{r}) = \mu_0 - V_{\text{trap}}(\mathbf{r})$.

We make a completely general ansatz for the domain wall, only assuming rotational symmetry about the long axis of the trap. We parameterize the boundary in terms of coordinates f and θ , which are related to the cylindrical coordinates ρ and z by

$$\begin{aligned}\rho(\theta, f) &= R_{\text{TF}} f \cos \theta \\ z(\theta, f) &= Z_{\text{TF}} f \sin \theta\end{aligned}\tag{4.5}$$

where $R_{\text{TF}} = \sqrt{\mu_0/b_{\perp}}$, $Z_{\text{TF}} = \sqrt{\mu_0/b_z}$. The boundary is described by the function $f = F(\theta)$. As shown in appendix A, the two-dimensional integrals for the free energy can then be simplified to one dimensional integrals, which can be performed numerically.

The optimal shape is found by minimizing the free energy functional $\Omega_{\text{T}} = \Omega_{\text{S}} + \Omega_{\text{N}} + E_{\text{DW}}$ on the space of functions $F(\theta)$ at fixed N_{\uparrow} and N_{\downarrow} . The constraints are imposed using Lagrange multipliers. We expand $F(\theta)$ as

$$F(\theta) = \sum_{n=0}^{\infty} a_n \cos(2n\theta)\tag{4.6}$$

which is compatible with the boundary conditions imposed by the symmetry of the problem, $F'(0) = F'(\pi/2) = 0$. We truncated this series at a finite number of Fourier components N_c and numerically minimized Ω_{T} with respect to a_0, a_1, \dots, a_{N_c} . We find that we need to include more terms in this series when η is larger, but for all values of η , the profiles become insensitive to N_c for $N_c \gtrsim 15$.

In figure 4.3 we plot the boundary $F(\theta)$ that minimizes Ω_{T} for different values of η . The boundary becomes almost insensitive to η for high surface tension. This behavior has two sources: (i) For large η the ends become increasingly flat, so surface tension plays an increasingly insignificant role, (ii) the edges along the minor axis touch the edge of the

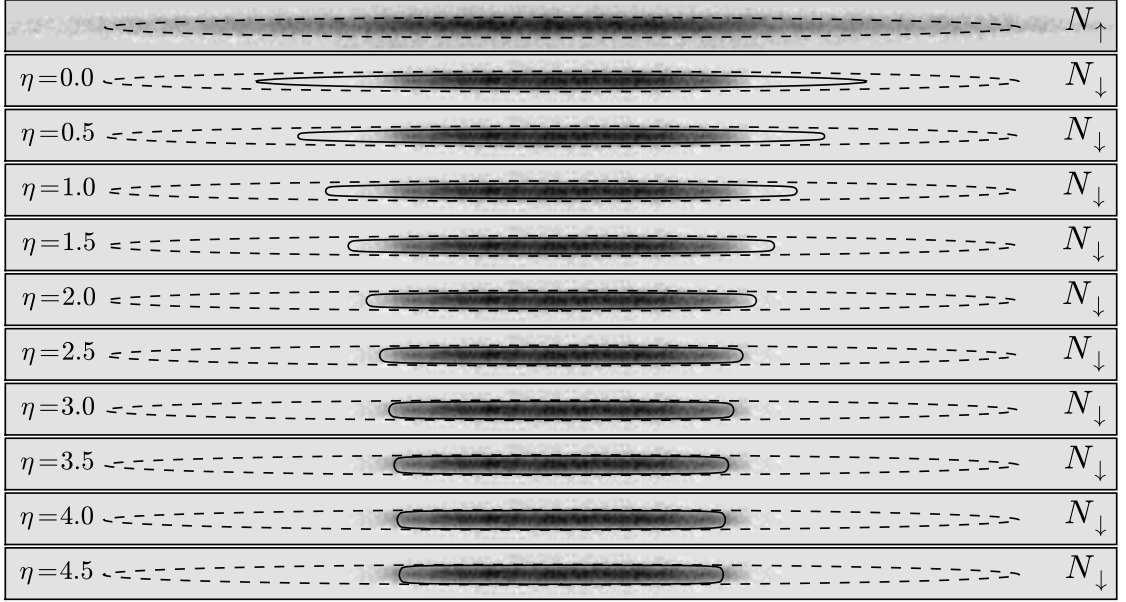


FIGURE 4.3: Experimental two-dimensional column densities (black denotes high density) for $P = 0.38$ with theoretically calculated boundaries for different surface tensions η (fixing the number of particles to be constant). Top: majority atoms N_{\uparrow} ; Bottom: minority atoms N_{\downarrow} . The dotted line is the ellipse with semi-major and semi-minor axes Z_{TF} and R_{TF} respectively, while the solid line is the superfluid-normal boundary in the presence of surface tension. As η is increased, the superfluid-normal boundary deforms from an elliptical isopotential surface, but the boundary becomes increasingly insensitive to surface tension with increasing η . $N_c = 15$ Fourier components were chosen for equation (4.6). Data corresponds to Fig. 1(c) in Ref. [2], used with permission. Data outside of an elliptical aperture has been excluded. This truncation of the data leads to a slight discrepancy in P compared to the value quoted in [2]. Each panel is $1.4\text{mm} \times 0.06\text{mm}$, and shows the true aspect ratio of the cloud.

majority cloud, at which point the superfluid-normal boundary changes to a superfluid-vacuum boundary and surface tension ceases to be important. Due to this “saturation” of the boundary shape with high η , and the difficulty of defining the boundary from noisy 2-D data, we find it convenient to follow references [174, 175] and find η by fitting our theoretical model to the 1-D axial densities, defined by $n_{\uparrow,\downarrow}^{(a)}(z) = \int dx dy n_{\uparrow,\downarrow}(x, y, z)$. As illustrated in Fig. 4.3, we improve signal to noise by excluding data outside of an elliptical window¹

¹We discarded all data outside of an ellipse which was chosen so that by eye only pixels with no particles in them were excluded. The ellipse was chosen independently for each spin state and each data set. This windowing increased the signal to noise while reducing significant systematic biases due to the back-

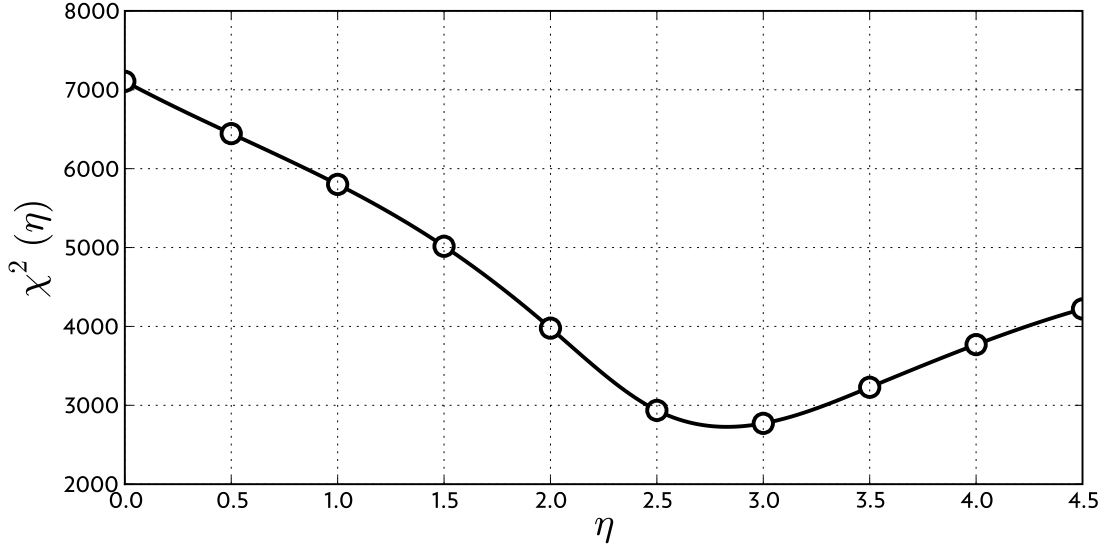


FIGURE 4.4: To pick the “best-fit” η , we fit the theoretical axial density difference to the experimental one from [2] corresponding to $P = 0.38$. χ^2 is defined in equation (4.7). The data has been elliptically windowed as in figure 4.3. $\eta = 2.83$ fits this data best.

We define a cost function $\chi^2(\eta)$ as

$$\chi^2(\eta) = \frac{1}{M} \sum_{m=1}^M \left[\left(n_{\uparrow, \text{expt}}^a(z_m) - n_{\uparrow, \text{theor}}^a(z_m) \right)^2 + \left(n_{\downarrow, \text{expt}}^a(\eta, z_m) - n_{\downarrow, \text{theor}}^a(\eta, z_m) \right)^2 \right] \quad (4.7)$$

where M is the number of pixels in the z direction, and z_m is the position of the m^{th} pixel.

We choose the η that minimizes this χ^2 . Other fit measures, such as using $\sum_m \sum_{\sigma} \left(n_{\sigma, \text{expt}}^a(z_m) - n_{\sigma, \text{theor}}^a(\eta, z_m) \right)^2$ give very similar best-fit η -s. We find that $\eta \simeq 3$ gives an axial density difference profile most closely matching the experimental density from Ref. [2] for $P = 0.38$ and $P = 0.63$. As seen in figure 4.5, the overall quality of the fit is quite good. There are however distinct differences between the predictions of the model and the observed profiles. These can largely be attributed to trap anharmonicities which we did not model.

We also believe that the δP dependence of η may be important for capturing the exact shape of the domain wall. Generically one would expect that this dependence would reduce η at the ends of the boundary, increasing the curvature of the end-caps and making ground. For example by this measure the $P = 0.39$ data has $N_{\uparrow} = 155,000$, $N_{\downarrow} = 68,500$, while without windowing $N_{\uparrow} = 166,000$, $N_{\downarrow} = 88,000$.

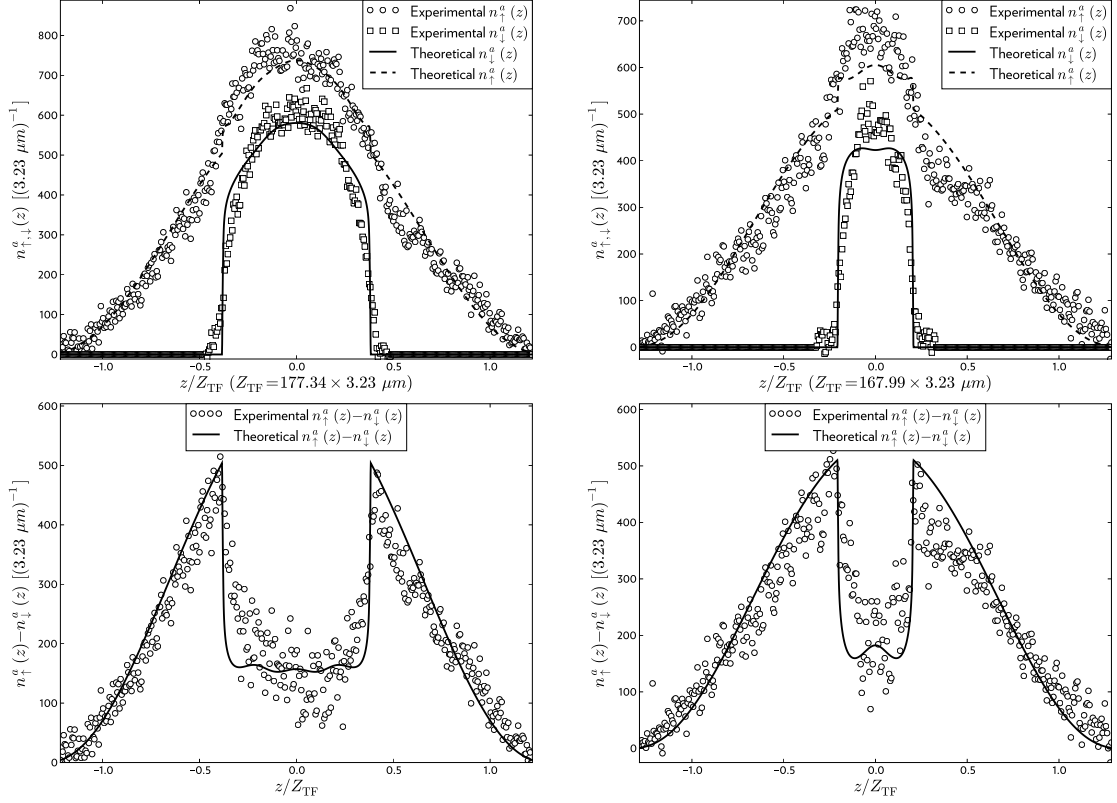


FIGURE 4.5: Axial densities. Symbols: experimental one-dimensional ${}^6\text{Li}$ spin densities and density differences for $P = 0.39$ ($N_{\uparrow} = 155,000$, $N_{\downarrow} = 68,500$) (left column) and $P = 0.63$ ($N_{\uparrow} = 123,600$, $N_{\downarrow} = 28,000$) (right column), from Ref. [2], with permission. Lines: theoretical curves for $\eta = 2.83$, taking a cigar shaped harmonic trap with small oscillation frequencies $\omega_z = (2\pi)7.2\text{Hz}$ and $\omega_r = (2\pi)325\text{Hz}$. Oscillations in the density difference within the superfluid region are artifacts of our ansatz (4.6). To minimize noise, only experimental data inside an elliptical window was considered (see text). This aperture is visible in figure 4.3.

ing a smoother axial density. This effect would also lead to an apparent polarization and number dependence of η . Finally, we found some sensitivity to how we treat the background in each image. For example, if we fit the axial density difference at $P = 0.6$ without windowing the data, we find that $\eta = 1$ provides a better fit.

Since they are based upon identical models (just using different ansatz's for the boundary shape), the quality of our fits are very similar to the ones found by Haque and Stoof when investigating a large number of similar profiles [175]. Converting to our units,

Haque and Stoof found $\eta = 4.8 \pm 1.2$. Their result is slightly higher than ours. We attribute this difference to differences in fitting procedures (such as windowing the data) and to modeling of the trap. Haque and Stoof used a more sophisticated Gaussian model for the trap, while we assumed it was harmonic.

4.4 Microscopic theory

As illustrated on the left of figure B.1 in appendix B, at low temperatures there's a discontinuous phase transition between the normal and the paired state, at which point the free energy \mathcal{F} (defined in (B.8)) is the same on both sides. However, (B.8) only holds for a spatially constant Δ . At a normal-SF interface, Δ goes from a non-zero value to zero, and this spatial variation adds to the free energy (B.8). In general, we can write the free energy as a Landau-Ginzburg expansion in the order parameter Δ :

$$\begin{aligned} \mathcal{F} = \int d^3\mathbf{r} & \left[\alpha_1 |\Delta(\mathbf{r})|^2 + \alpha_2 |\nabla\Delta(\mathbf{r})|^2 + \alpha_3 |\nabla^2\Delta(\mathbf{r})|^2 + \dots \right. \\ & + \gamma_1 |\Delta(\mathbf{r})|^4 + \gamma_2 |\Delta(\mathbf{r})|^6 + \dots \\ & \left. + \text{gradient terms of order higher than } \Delta^2 \right] \end{aligned} \quad (4.8)$$

The terms with spatially constant Δ , i.e., α_1 , γ_1 , γ_2 , etc. are contained in (B.8). Here we calculate the terms with coefficients α_2 , α_3 , etc. We neglect gradient terms higher than $O(\Delta^2)$, an approximation well-justified near the tricritical point. This approximation however introduces a significant error at $T = 0$. For the terms which are quadratic in Δ , we go to all orders in the gradient. We will see that as the temperature is lowered, α_2 , α_3 etc. successively become negative and the system is stabilized by higher gradients. The terms are readily read off from a path integral representation of the partition function.

We use a Hubbard-Stratonovich transformation (detailed in appendix C) on the usual two-particle point interaction Hamiltonian. Taking the log of the partition function (C.14),

we get the terms in the free energy that go as Δ^2

$$\mathcal{F}_2 = - \sum_{\mathbf{k}} \chi(\mathbf{k}) |\Delta(\mathbf{k})|^2 \quad (4.9)$$

The term with coefficient α_1 in (4.8) appears in both \mathcal{F} in (B.8) and in \mathcal{F}_2 above. To avoid double-counting, we subtract the $\mathbf{k} = 0$ (spatially homogenous) term from \mathcal{F}_2 . In other words, the free energy after adding \mathcal{F}_2 to \mathcal{F} is

$$\mathcal{F}_{\text{total}} = \mathcal{F} - \sum_{\mathbf{k}} (\chi(\mathbf{k}) - \chi(0)) |\Delta_{\mathbf{k}}|^2 \quad (4.10)$$

where we've freely switched between \mathbf{k} and k because $\chi(\mathbf{k})$ depends only on k , which is the magnitude of \mathbf{k} . The function $\chi(\mathbf{k})$ is the static ($\nu = 0$) limit of the more general two-particle propagator of equation (3.7), and is of general importance in the many-body problem of the BEC-BCS crossover of spin-polarized fermions, such as T-Matrix approximation schemes [176] and the finite-momentum pairing instability of the polarized normal phase to the FFLO phase [177, 178]. At $T = 0$, the integral in equation (C.15) can be done analytically to yield the result in equation (3.11), of which we only need the static part (since Δ is time-invariant). At finite T , the integral (C.15) has to be done numerically. The normal state becomes locally unstable towards finite \mathbf{q} pairing when the coefficient of $|\Delta_{\mathbf{q}}|^2$ in equation (C.14) becomes negative, or

$$\chi(\mathbf{q}, 0) - \frac{1}{U} = 0$$

Above the tricritical point, this Thouless criterion locates the second order phase boundary, while below the tricritical point it yields the spinodal of the first order phase transition.

Explicit expressions for the coefficients $\alpha_1, \alpha_2, \alpha_3, \dots$ of (4.8) are found by expanding $\chi(\mathbf{q})$ in powers of q . The exact profile of Δ at the domain wall between the normal $\Delta = 0$ and the superfluid $\Delta = \Delta_0$ can be found by minimizing $\mathcal{F}_{\text{total}}$ of (4.10), where $\Delta(\mathbf{r}) =$

$\text{Vol}^{-1} \sum_{\mathbf{q}} e^{i\mathbf{q}\cdot\mathbf{r}} \Delta_{\mathbf{q}}$. Since we're interested in the surface energy of an interface with zero curvature, we use the ansatz

$$\Delta(\mathbf{r}) = \Delta(z) = \frac{\Delta_0}{2} (\text{erf}(4z/W_{\text{dw}}) + 1) \quad (4.11)$$

which goes smoothly from $\Delta(z \rightarrow -\infty) = 0$ to $\Delta(z \rightarrow \infty) = \Delta_0$, and has the advantage of having a tractable Fourier transform (so that $\Delta_{\mathbf{q}}$ can be handled analytically). For a given $\beta\bar{\mu}$, we assume we're at the critical polarization (h_c in figure B.1, left) for a discontinuous phase transition between the SF and the normal phases, and calculate Δ_0 from equation (B.5). Using our ansatz for $\Delta(\mathbf{r})$, we minimize $\mathcal{F}_{\text{total}}$ with respect to W_{dw} , which is a measure of the width of the domain wall. Figure 4.6 shows the resulting temperature

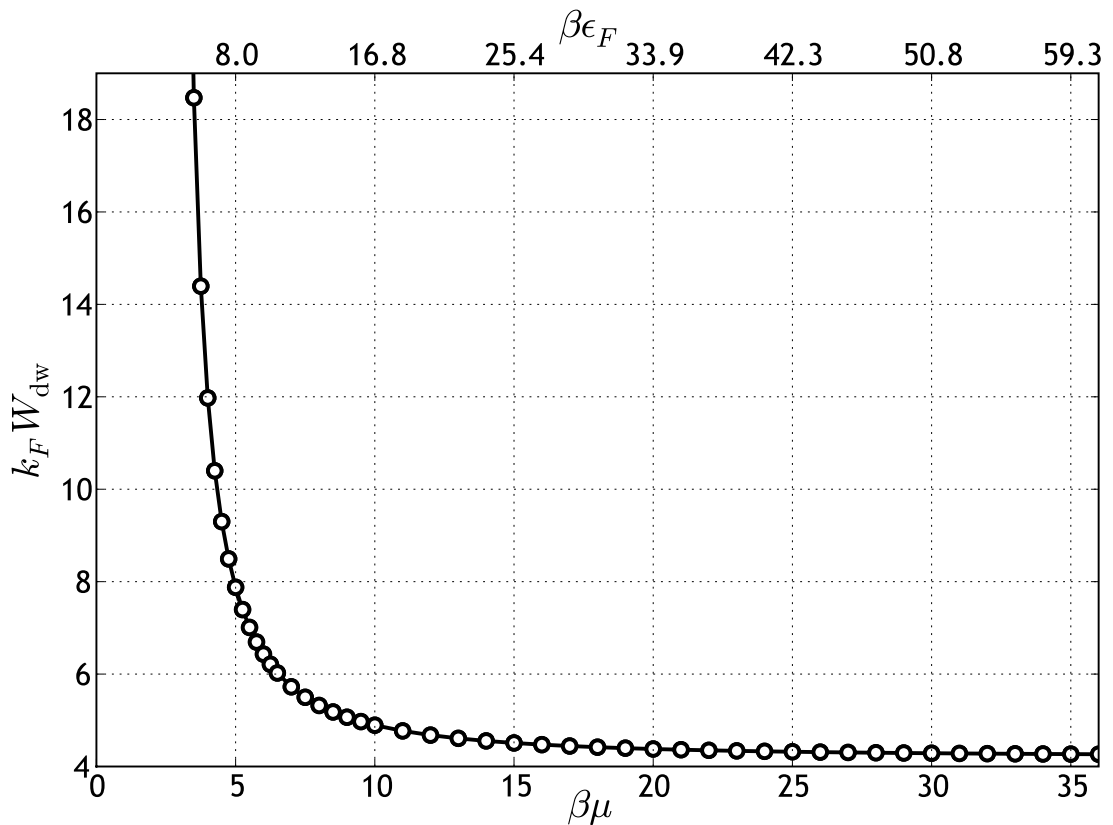


FIGURE 4.6: Width (W_{dw}) of the domain wall as function of inverse temperature (β) at unitarity, with parameters measured in terms of the chemical potential μ and $k_F^3 = 3\pi^2 n_s$. The domain wall width diverges at the tricritical point around $\beta\mu \sim 2.0$. Values of $\beta\epsilon_F$ at the top use $\epsilon_F = \hbar^2(3\pi^2 n_s)^{2/3}/2m$.

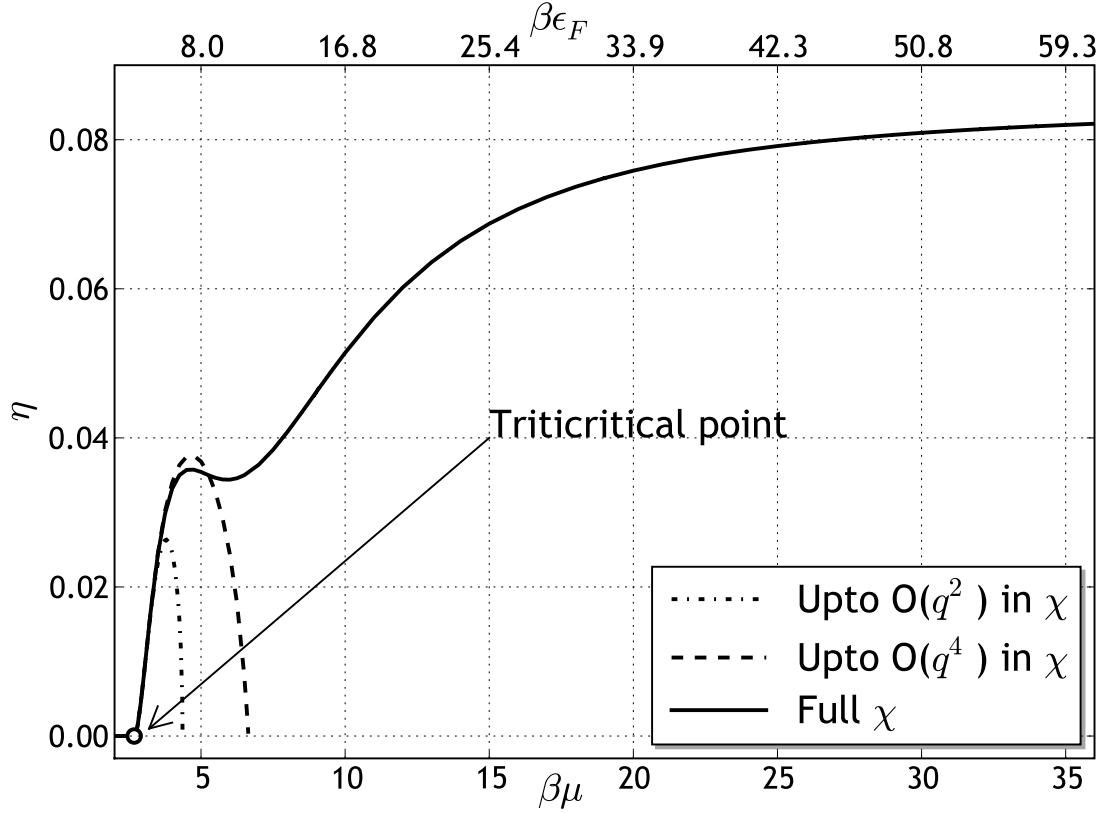


FIGURE 4.7: Dimensionless surface tension $\eta = 2\hbar^{-2}mn_s^{-4/3}\sigma$ as a function of inverse temperature β , keeping different numbers of terms in the gradient expansion. Even with the full χ , we include terms up to $O(\Delta^2)$ in the free energy. As temperatures goes to zero, the solid line suggests $\eta \sim 0.1$. Values of $\beta\epsilon_F$ at the top use $\epsilon_F = \hbar^2(3\pi^2n_s)^{2/3}/2m$.

dependence of the domain wall at unitarity. As can be seen, the domain wall diverges at the tricritical point. Using the same notation as in appendix B, the superfluid density n_s is given by

$$n_s = \frac{1}{2\pi^2} \left(\frac{2m}{\hbar^2\beta} \right)^{3/2} \int_0^\infty dy y^2 \left[1 - \left(\frac{y^2 - \beta\mu}{E_y} \right) \frac{\sinh E_y}{\cosh E_y + \cosh \beta h} \right] \quad (4.12)$$

using $\Delta = \Delta_0$.

The surface energy of the interface for a given W_{dw} is found by integrating $\mathcal{F}_{\text{total}}(\Delta(z))$ across the interface in the z direction, which by definition is the surface tension σ . Using n_s from (4.12), we evaluate η as defined in equation (4.4) for the optimal W_{dw} at each $\beta\mu$. The result is shown in figure 4.7, which also shows what this surface tension would be if

we expand $\chi(q)$ to either quadratic or quartic order in q . This corresponds to truncating (4.8) at α_2 or α_3 . While these latter approximations work well around the tricritical point, they do not correctly describe the low temperature physics: both α_2 and α_3 change sign at low temperature, and without the influence of higher order terms, the normal state becomes unstable to a FFLO state, and the surface tension vanishes. Using the full χ , we find that as $T \rightarrow 0$, the dimensionless surface tension becomes $\eta \sim 0.1$. The discrepancy between this result and the best-fit η from figure 4.4 can be ascribed, at least in part, to the neglect of gradient terms higher order in Δ . While these terms are unimportant near the tricritical point, as $T \rightarrow 0$, Δ becomes large and these terms become significant. It is likely that the kink in figure 4.7 is also a result of this truncation.

CHAPTER 5

A “DILUTION FRIDGE” OF COLD ATOMIC VAPORS

This chapter presents unpublished work.

5.1 Motivation

We present a method of cooling a gas of cold Fermions, which is analogous to a traditional dilution refrigerator. This analogy is interesting in its own right; cold gas physics is a direct descendant of low temperature physics. Further, we find the efficiency of this cooling method to be comparable to that of evaporative cooling.

A conventional ^3He - ^4He dilution fridge, first proposed by H. London in 1951, works by utilizing the latent heat of mixing of ^3He in ^4He [179]. The phase diagram of ^3He in ^4He is illustrated in figure 5.1 (left). There is a first order transition between a ^3He -rich phase and a ^3He -poor phase. Consequently, at low temperatures a mixture of ^3He and ^4He phase separates into these two phases. This phase separation is analogous to a half-filled flask of water; the lower half of the flask is rich in water and poor in air, whereas the upper half is rich in air and poor in water. When a water molecule evaporates from the water-rich phase to the water-poor phase, it crosses a first-order phase boundary and absorbs some latent heat, cooling the fluid near the phase boundary. The ^4He can be considered to be a “vacuum” for ^3He atoms; whenever a ^3He atom “evaporates” from the ^3He -rich phase to the ^3He -poor region at a fixed temperature (right to left across the phase separated region), it absorbs latent heat and cools the ^3He -rich phase, as well as anything in contact with the fluid. Figure 5.1 (right) illustrates the geometry of a dilution refrigerator based on this effect.

The entire bottom portion of the tubing in figure 5.1 (right) is filled with ^4He , and ^3He

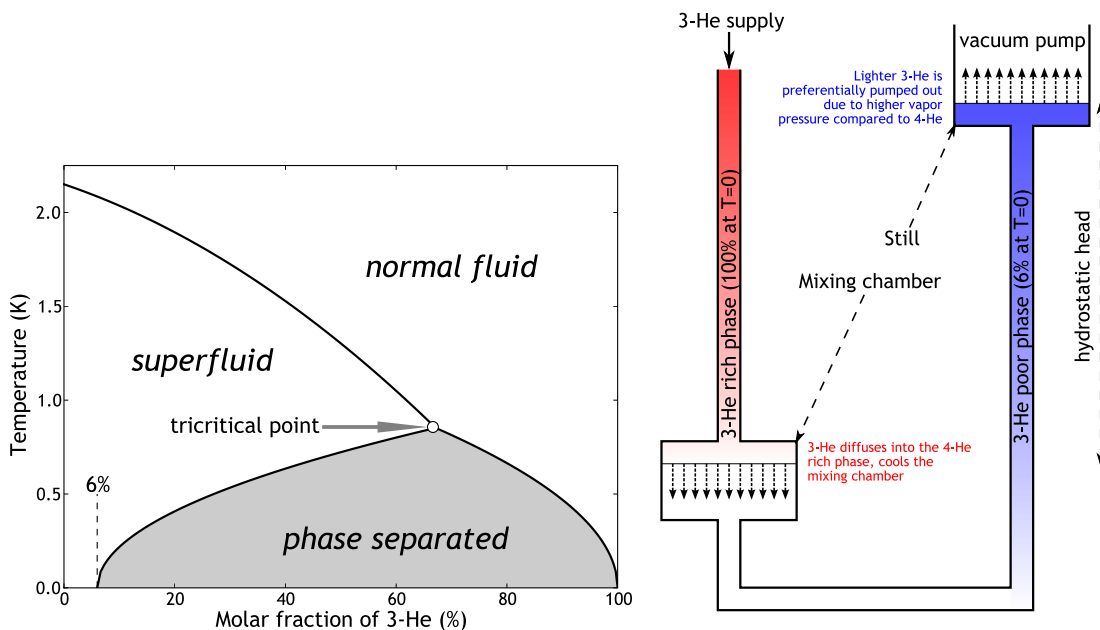


FIGURE 5.1: **Left:** ^3He - ^4He phase diagram at standard pressure. **Right:** Schematic of a traditional dilution fridge. Progressively deeper shades of red indicate higher ^3He temperature, while deeper shades of blue indicate higher ^4He concentration.

is introduced into the mixing chamber. Since ^3He has a lower mass density, it floats on the top, but some of it dissolves into ^4He , depending on the equilibrium percentage at that temperature. A vacuum pump forces evaporation from the surface of the ^3He - ^4He mixture in the still, illustrated on the right of figure 5.1. Since ^3He has a higher vapor pressure by virtue of being lighter, it is preferentially removed. This depletes the ^3He - ^4He mixture of ^3He , which is then drawn into the mixture from the mixing chamber to maintain the equilibrium concentration. This process absorbs energy (the latent heat of mixing), cooling the mixing chamber and anything in contact with it. Such refrigerators can reach temperatures of a few milliKelvins. The practical limit is set by heat loss due to recycling the ^3He from the still to the mixing chamber.

One key fact that allows this setup to work is the non-zero concentration of ^3He in the ^3He -poor phase (the ^3He - ^4He mixture) even at $T = 0$. This means that no matter how low the temperature, there is always a non-zero flux of ^3He into the mixture inside the

mixing chamber, and therefore a non-zero cooling rate.

The phase diagram of a ^3He - ^4He mixture is topologically identical to the phase diagram of a spin-polarized fermi gas (figure 5.2), with the excess up-spins playing the role of ^3He , and the pairs playing the role of ^4He . Consistent with this picture, clouds

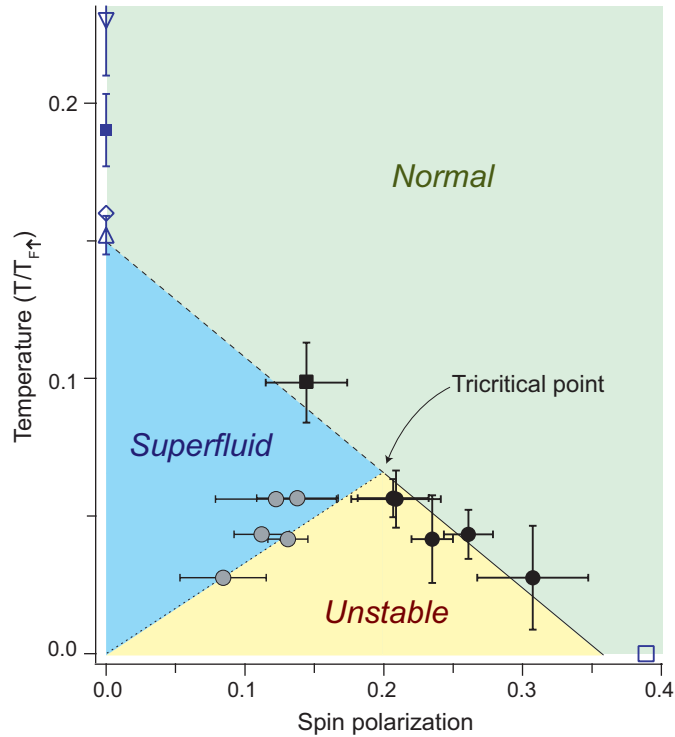


FIGURE 5.2: Phase diagram of a spin-polarized fermi gas of ^6Li at unitarity, courtesy Yong-il Shin [3]. This is topologically identical to the ^3He - ^4He phase diagram in figure 5.1. We will see that unlike this picture, there exists a partially polarized superfluid phase at $T = 0$ on the BEC side of a Feshbach resonance.

of spin-polarized Fermi gases display a fermion-poor superfluid core and a fermion-rich normal shell with a polarization and density discontinuity at the boundary (see, e.g., figures 4.1, 4.2 and 4.3). Due to this analogy with ^3He - ^4He mixtures, one would expect that if one could drive a flux of fermions from the normal to the superfluid phase, the latent heat of mixing would cool the boundary. The value of this cooling technique is that one would expect it to continue working at very low temperatures, even below those at which evaporative cooling becomes impractical. Here we evaluate the feasibility of this scheme,

proceeding in three steps. First, we generate the phase diagram for a polarized Fermi gas. Second, we need to calculate the latent heat of mixing, both to find its magnitude and sign. Third, we estimate the “efficiency” of this cooling, i.e., the fractional decrement in temperature achieved for some fractional loss of particles (analogous to the pumping of ^3He from the still). Additionally, we develop a protocol for implementing the cooling scheme.

5.2 Phase diagram

Deep in the BEC phase, a spin-polarized fermi gas can be modeled as a mixture of fermions and bound molecules, or bosons, with the Hamiltonian

$$\begin{aligned} \mathcal{H} = & \sum_{\mathbf{k}} (\epsilon_{\mathbf{k}} - \mu_f) \psi_{\mathbf{k}}^\dagger \psi_{\mathbf{k}} + \sum_{\mathbf{k}} (E_{\mathbf{k}} - \mu_b) \phi_{\mathbf{k}}^\dagger \phi_{\mathbf{k}} \\ & + \frac{g_{bb}}{2} \sum_{\mathbf{k}\mathbf{p}\mathbf{q}} \phi_{\frac{\mathbf{k}}{2}+\mathbf{p}}^\dagger \phi_{\frac{\mathbf{k}}{2}-\mathbf{p}}^\dagger \phi_{\frac{\mathbf{k}}{2}-\mathbf{q}} \phi_{\frac{\mathbf{k}}{2}+\mathbf{q}} + g_{bf} \sum_{\mathbf{k}\mathbf{p}\mathbf{q}} \phi_{\frac{\mathbf{k}}{2}+\mathbf{p}}^\dagger \psi_{\frac{\mathbf{k}}{2}-\mathbf{p}}^\dagger \psi_{\frac{\mathbf{k}}{2}-\mathbf{q}} \phi_{\frac{\mathbf{k}}{2}+\mathbf{q}} \end{aligned} \quad (5.1)$$

where ψ is a fermion operator and ϕ is a boson operator. Since the fermions are spin-polarized and the interactions are short-ranged, the Pauli exclusion principle forbids any direct interaction. Deep in the BEC phase, the couplings constants are related to the scattering lengths as $g_{bf,bb} = 4\pi\hbar^2 a_{bf,bb}/m_{bf,bb}$ where $m_{bf} = 2m_b m_f / (m_b + m_f)$ and $m_{bb} = m_b$. By solving the three- and four-body problems one finds that the fermi-bose and fermi-fermi scattering lengths in this limit are $a_{bb} = \lambda_b a = 0.6a$ [170, 180] and $a_{bf} = \lambda_f a = 1.2a$ [181] where $a > 0$ is the atom-atom scattering length.

We need to calculate the free energy of this interacting Bose-Fermi system. In the dilute limit $na^3 \ll 1$, there are a number of candidate mean-field theories we can use for this calculation. Even for the simpler case of interacting bosons, there is a zoo of approaches such as Hartree-Fock, Bogoliubov, Hartree-Fock-Bogoliubov, Hartree-Fock-Popov, etc.

However, in this case, we're interested in the low temperature thermodynamic properties of the system, such as specific heat and enthalpy of mixing. For those properties, it appears that that Hartree-Fock mean field theory yields results that are only marginally improved by the more sophisticated theories [182]. Therefore, we will use a Hartree-Fock approximation for the interacting bosons.

At temperatures below the BEC temperature for the bosons, a fraction of the bosons will be bose condensed. In other words, the bose operators can be written as

$$\phi_{\mathbf{k}} = \alpha \delta_{\mathbf{k},0} + (1 - \delta_{\mathbf{k},0}) \phi_{\mathbf{k}}$$

where α is a complex number and $|\alpha|^2$ is the condensate density (without loss of generality, we assume α is real). Introducing another mean field $n_{\text{ex}} = \sum'_{\mathbf{k}} \langle \phi_{\mathbf{k}}^\dagger \phi_{\mathbf{k}} \rangle$ and neglecting quartic fluctuations, the bosonic part of \mathcal{H} becomes

$$\mathcal{H}_{\text{bosons}} = -\mu_b \alpha^2 + \frac{g_{\text{bb}}}{2} \alpha^4 + \sum'_{\mathbf{k}} (E_{\mathbf{k}} - \mu_b + 2g_{\text{bb}} \alpha^2 + 2g_{\text{bb}} n_{\text{ex}}) \phi_{\mathbf{k}}^\dagger \phi_{\mathbf{k}} - g_{\text{bb}} n_{\text{ex}}^2$$

in which a primed sum goes over all $\mathbf{k} \neq 0$ states. Adding the fermionic part and the bose-fermi interaction (treated within Hartree-Fock), the total Hamiltonian is

$$\mathcal{H} = -\mu_b \alpha^2 + \frac{g_{\text{bb}}}{2} \alpha^4 - g_{\text{bb}} n_{\text{ex}}^2 - g_{\text{bf}} n_b n_f + \sum'_{\mathbf{k}} (E_{\mathbf{k}} - \bar{\mu}_b) \phi_{\mathbf{k}}^\dagger \phi_{\mathbf{k}} + \sum_{\mathbf{k}} (\epsilon_{\mathbf{k}} - \bar{\mu}_f) \psi_{\mathbf{k}}^\dagger \psi_{\mathbf{k}} \quad (5.2)$$

where $n_b = \alpha^2 + n_{\text{ex}}$, $n_f = \sum_{\mathbf{k}} \langle \psi_{\mathbf{k}}^\dagger \psi_{\mathbf{k}} \rangle$, $\bar{\mu}_b = \mu_b - 2g_{\text{bb}} n_b - g_{\text{bf}} n_f$ and $\bar{\mu}_f = \mu_f - g_{\text{bf}} n_b$. This Hamiltonian is diagonal in the operators, and hence the free energy per unit volume (\mathcal{A}) at finite temperature is straightforward to calculate:

$$\begin{aligned} \mathcal{A} = & (-\mu_b + g_{\text{bf}} n_f) \alpha^2 + \frac{g_{\text{bb}}}{2} \alpha^4 - g_{\text{bb}} (n_b - \alpha^2)^2 \\ & - \frac{\sqrt{2m_b^3}}{3\pi^2 \beta^{5/2}} G_{3/2}(\beta \bar{\mu}_b) - \frac{\sqrt{2m_f^3}}{3\pi^2 \beta^{5/2}} F_{3/2}(\beta \bar{\mu}_f) \end{aligned} \quad (5.3)$$

where F and G are Fermi-Dirac and Bose-Einstein integrals,

$$F_k(x) = \int_0^\infty \frac{y^k}{e^{y-x} + 1} dy \quad G_k(x) = \int_0^\infty \frac{y^k}{e^{y-x} - 1} dy \quad (5.4)$$

Although both the chemical potentials μ_f , μ_b and the densities n_b , n_f , α^2 appear in these expressions, \mathcal{A} should be viewed as a function of μ_b and μ_f . The densities are mean fields, which themselves should be viewed as functions of μ_b and μ_f . These mean fields can be defined in one of two ways, either the free energy should be stationary with respect to their variations,

$$\left. \frac{\partial \mathcal{A}}{\partial \alpha^2} \right|_{\mu_b, \mu_f, n_b, n_f} = 0 \quad \left. \frac{\partial \mathcal{A}}{\partial n_b} \right|_{\mu_b, \mu_f, n_f} = 0 \quad \left. \frac{\partial \mathcal{A}}{\partial n_f} \right|_{\mu_b, \mu_f, n_b} = 0$$

or that they satisfy the self-consistency relations¹

$$n_b = - \left. \frac{\partial \mathcal{A}}{\partial \mu_b} \right|_{\mu_f} \quad n_f = - \left. \frac{\partial \mathcal{A}}{\partial \mu_b} \right|_{\mu_b}$$

While not completely obvious, these two sets of conditions are equivalent. Extremizing \mathcal{A} with respect to the condensate density, $\partial \mathcal{A} / \partial \alpha^2 = 0$ yields

$$\alpha^2 = \frac{1}{g_{bb}} (2g_{bb}n_b + g_{bf}n_f - \mu_b) \quad (5.5)$$

which is the usual Bosonic Hartree-Fock result with an extra $g_{bf}n_f$ term accounting for interaction with the Fermions. We adimensionalize the variables with the following substitutions: $n_f = x/a^3$, $n_b = y/a^3$, $g_{bf} = 3\pi a\lambda_f/m$, $g_{bb} = 2\pi a\lambda_b/m$, $\mu_{b,f} = v_{b,f}/ma^2$ and $\beta \rightarrow \beta ma^2$. Then in the presence of a condensate ($\alpha^2 > 0$) the conditions $\partial \mathcal{A} / \partial n_f = 0$ and $\partial \mathcal{A} / \partial n_b = 0$ reduce to

$$\begin{aligned} x - \frac{1}{\pi^2 2^{1/2} \beta^{3/2}} F_{1/2} [\beta(v_f - 3\pi\lambda_f y)] &= 0 \\ y - \frac{1}{2\pi\lambda_b} (v_b - 3\pi\lambda_f x) + \frac{2}{\pi^2 \beta^{3/2}} G_{1/2} [\beta(v_b - 4\pi\lambda_b y - 3\pi\lambda_f x)] &= 0 \end{aligned} \quad (5.6)$$

while in the absence of a condensate ($\alpha^2 = 0$), such as above the BEC transition temperature,

$$\begin{aligned} x - \frac{1}{\pi^2 2^{1/2} \beta^{3/2}} F_{1/2} [\beta(v_f - 3\pi\lambda_f y)] &= 0 \\ y - \frac{2}{\pi^2 \beta^{3/2}} G_{1/2} [\beta(v_b - 4\pi\lambda_b y - 3\pi\lambda_f x)] &= 0 \end{aligned} \quad (5.7)$$

¹Note that the condensate density still has to be determined by $\partial \mathcal{A} / \partial \alpha^2 = 0$, since there's no "chemical potential" for the condensate.

These equations are nonlinear, and there is not a unique solution for a given μ_f , μ_b and β . A major difference between the cold atom systems and liquid Helium is that the atomic gases are highly compressible. Consequently, the relevant phase diagram is three dimensional, in (μ_b, μ_f, T) or (n_b, n_f, T) , and we need to solve not one but two equations simultaneously to find the phases.

5.2.1 Zero temperature

At $T = 0$ or $\beta = +\infty$, $G_k(\beta\bar{v}_b) \rightarrow 0$ while $F_k(\beta\bar{v}_f) \rightarrow (\beta\bar{v}_f)^{k+1}/(k+1)$. For $v_f, v_b < 0$, equations (5.6) are only satisfied by $x = y = 0$. In other regions, equations (5.6) generically have three types of solutions, (i) $x = 0, y > 0$, or a Bose phase, (ii) $x > 0, y = 0$, or a Fermi phase, and (iii) $x > 0, y > 0$, or a mixed phase. In the parameter space of v_f and v_b , the Fermi phase coexists with the Bose and mixed phases over certain regions, resulting in two discontinuous phase boundaries. The phase diagram is shown in figure 5.3. Even at $T = 0$, the system has a mixed phase of bosons and fermions, analogous to the “mixed phase” of 6% ^3He and 94% ^4He in figure 5.1. This means that if this system can be made into a dilution fridge, cooling will be possible at arbitrarily low temperatures.

5.2.2 Finite temperature

At finite temperature, the dash-dotted line in figure 5.3 disappears, leaving only a phase transition between a bose-condensed phase B and a normal phase F, such that $n_f^B < n_f^F$, as shown in figure 5.4. Since the boson density (and hence v_b) required for bose condensation goes up with temperature, the phase boundary in figure 5.4 (and P_c in figure 5.3) moves upward with decreasing β . These lines are the finite temperature versions of the dashed curve of figure 5.3. The solid curve between the origin and P_c in figure 5.3 turns

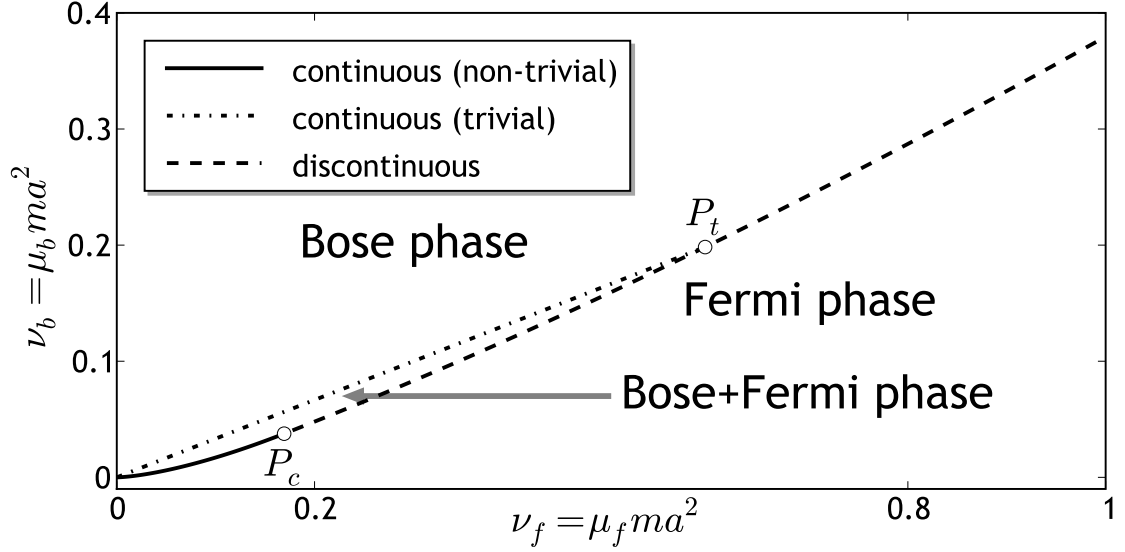


FIGURE 5.3: Phases of (5.6) at $T = 0$. $P_c = (8\pi^2\lambda_b^2/3^4\lambda_f^4, 32\pi^2\lambda_b^3/3^6\lambda_f^5)$ and $P_t = (25\pi^2\lambda_b^2/72\lambda_f^4, 25\pi^2\lambda_b^3/108\lambda_f^5)$. The dash-dotted line separating the bose phase from the mixed (bose+fermi) phase is $\nu_b = (2\lambda_b/3\lambda_f)\times\nu_f$ and the solid curve separating the mixed phase from the fermi phase is $\nu_b = 2^{1/2}\lambda_f\nu_f^{3/2}/\pi$. The dash-dotted line depicts the trivial phase transition between a Fermi vacuum and a Fermi sea, and disappears at $T > 0$. The solid line, however, is a non-trivial second order phase transition associated with the emergence of a pairing order; for $T > 0$, this curve turns into the second order BEC transition curve, while the dashed line turns into the first order BEC transition curve. P_c , which shifts with changing temperature, is a tricritical point.

into second order bose condensation curves (not shown) in figure 5.4.

5.3 Latent heat

The free energy defined in (5.3) $\mathcal{A} = (E/V) - \mu_f n_f - \mu_b n_b - T(S/V)$ can be related to pressure using a Gibbs-Duheim relation:

$$\mathcal{A} = -P$$

which means that the pressures on two sides of a normal-superfluid interface are equal, which is expected; for example, in chapter 4 we argued that the pressure drop across a flat

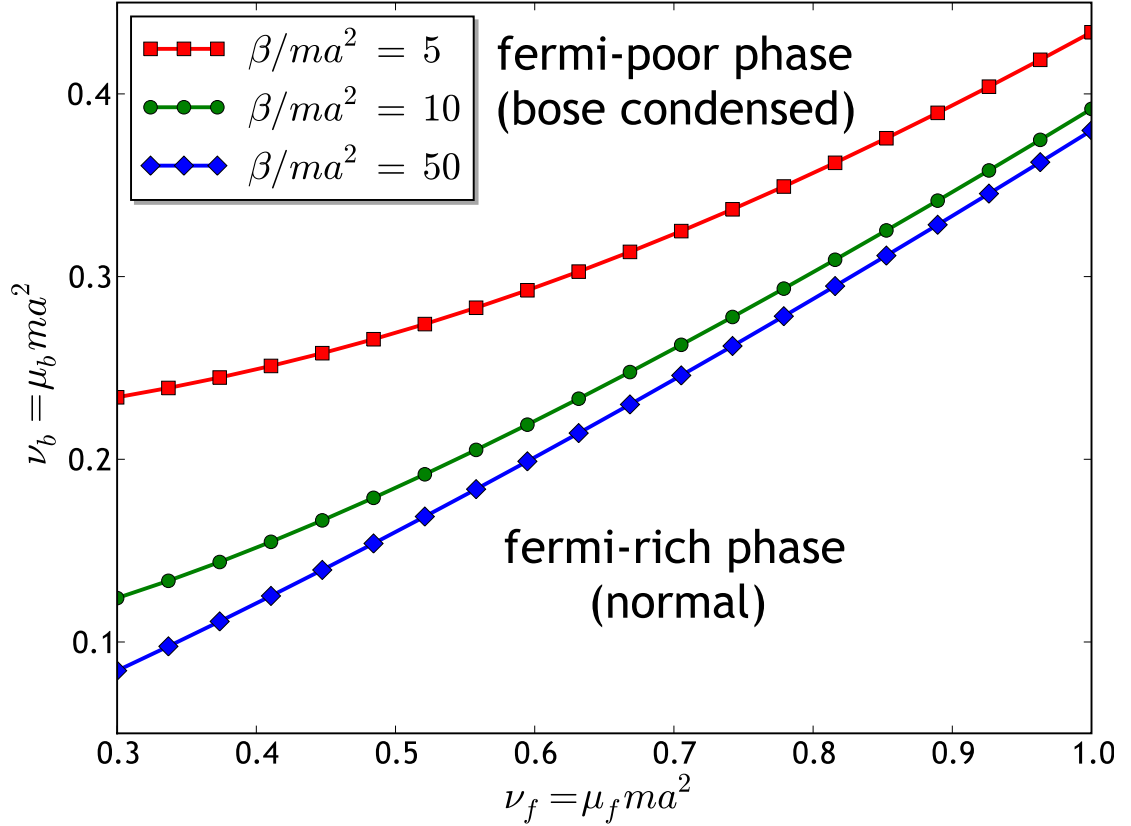


FIGURE 5.4: Finite temperature solutions of (5.6) and (5.7), zoomed in on the region of interest. Solid lines here are the $T > 0$ versions of the dashed curve in figure 5.3, while the solid curve between $(0, 0)$ and P_c in figure 5.3 turns into the $T > 0$ second order bose condensation curve (not shown above). The lines correspond to different temperatures, and separate a fermi-poor phase where some of the bosons are condensed from a fermi-rich normal phase. As T increases (β decreases), a higher boson density is required for condensation, which is why the lines move upward in the figure with decreasing β .

interface is zero, because if it weren't, the interface would move. However, when a fermion is transferred from phase F to phase B, the entropy change is not the same on both sides (exactly as in the ^3He - ^4He case). The resultant latent heat of mixing per fermion is given by

$$\left. \frac{\delta Q}{\partial N_f} \right|_{P,T} = T \left[\left. \frac{\partial S_{SF}}{\partial N_f} \right|_{P,T,N_b} - \left. \frac{\partial S_N}{\partial N_f} \right|_{P,T,N_b} \right] \quad (5.8)$$

Since we want to keep pressure – which is a function of the densities and chemical potentials – constant, evaluating this derivative is a lengthy exercise detailed in appendix E.2. The resulting latent heat per particle is plotted in figure 5.5. The latent heat drops with

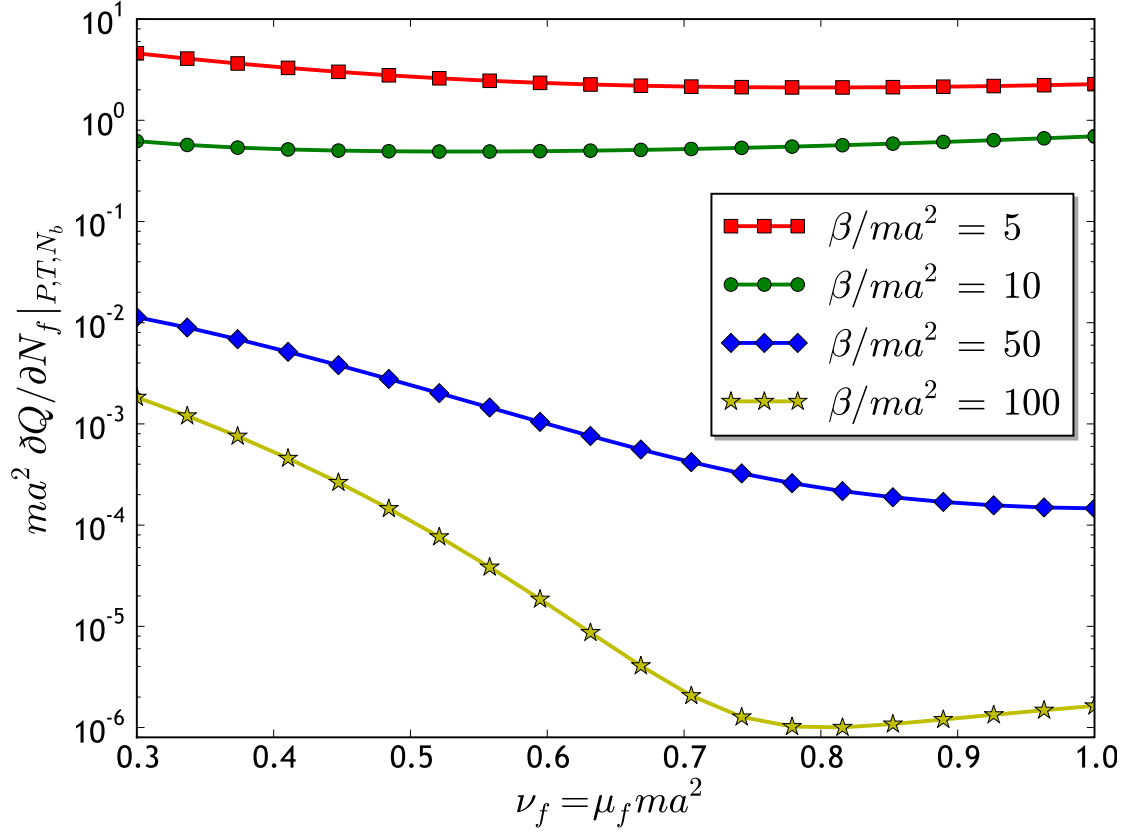


FIGURE 5.5: Latent heat of mixing per fermion along the phase boundary, as per equation (E.12). The lines above follow the phase boundaries as defined by the corresponding lines in figure 5.4, except that in figure 5.4 the $\beta/m a^2 = 100$ is almost on top of the $\beta/m a^2 = 50$ line, and is therefore not shown. The latent heats extend over a large range, and hence are presented on a log scale. We will see later that $\beta/m a^2 = 10$ is a plausible operating point.

temperature, which reflects the expected trend that it becomes harder to cool as we lower the temperature.

5.4 Cooling efficiency

For any cooling technique that relies on loss of particles, it is customary to characterize it by a cooling efficiency η ,

$$\eta = \frac{\log[T_{\text{final}}/T_{\text{initial}}]}{\log[N_{\text{final}}/N_{\text{initial}}]}$$

or its differential form

$$\eta = \frac{\Delta T/T}{\Delta N/N} \quad (5.9)$$

Given that we're working in a two-component system, one has several choices for which N to use in this definition; we use the total particle number, so $\Delta N/N \equiv \Delta N_f/(N_f + N_b)$. A larger η is better, as one wishes to cool as much as possible while minimizing atom loss. To calculate ΔT , we need the specific heat,

$$C_P = T \left. \frac{\partial S}{\partial T} \right|_{P, N_f, N_b}$$

whose calculation is detailed in appendix E.3. If a fermion loss ΔN_f results in a temperature change ΔT , then

$$\Delta N_f \times T \left. \frac{\partial S}{\partial N_f} \right|_{P, T, N_b} = C_P \Delta T$$

In terms of the functions $\Phi(x, y)$, $\Gamma(x, y)$ and $\kappa(x, y)$ defined in (E.12) and (E.19), we arrive at

$$\frac{N_f}{N} \left[\left(\Phi + \frac{\Gamma}{x} \right)_{\text{SF}} - \left(\Phi + \frac{\Gamma}{x} \right)_N \right] = \frac{1}{\beta(x+y)_N} \left[\Phi - \frac{\Gamma^2}{\kappa} \right] \frac{\Delta T}{T} \quad (5.10)$$

We assume that the system stays in thermal equilibrium, so that the heat lost is distributed evenly throughout the normal phase. This then yields

$$\eta = \frac{\Delta T/T}{\Delta N_f/N} = \frac{\beta(x+y)_N \left\{ \left[\Phi + \frac{\Gamma}{x} \right]_{\text{SF}} - \left[\Phi + \frac{\Gamma}{x} \right]_N \right\}}{\left[\Phi - \frac{\Gamma^2}{\kappa} \right]_N} \quad (5.11)$$

The cooling efficiency is plotted in figure 5.6 for each phase boundary in figure 5.5. For comparison, a typical evaporative cooling efficiency is $\eta \sim 4$, while under optimal conditions one can find $\eta = 20$.

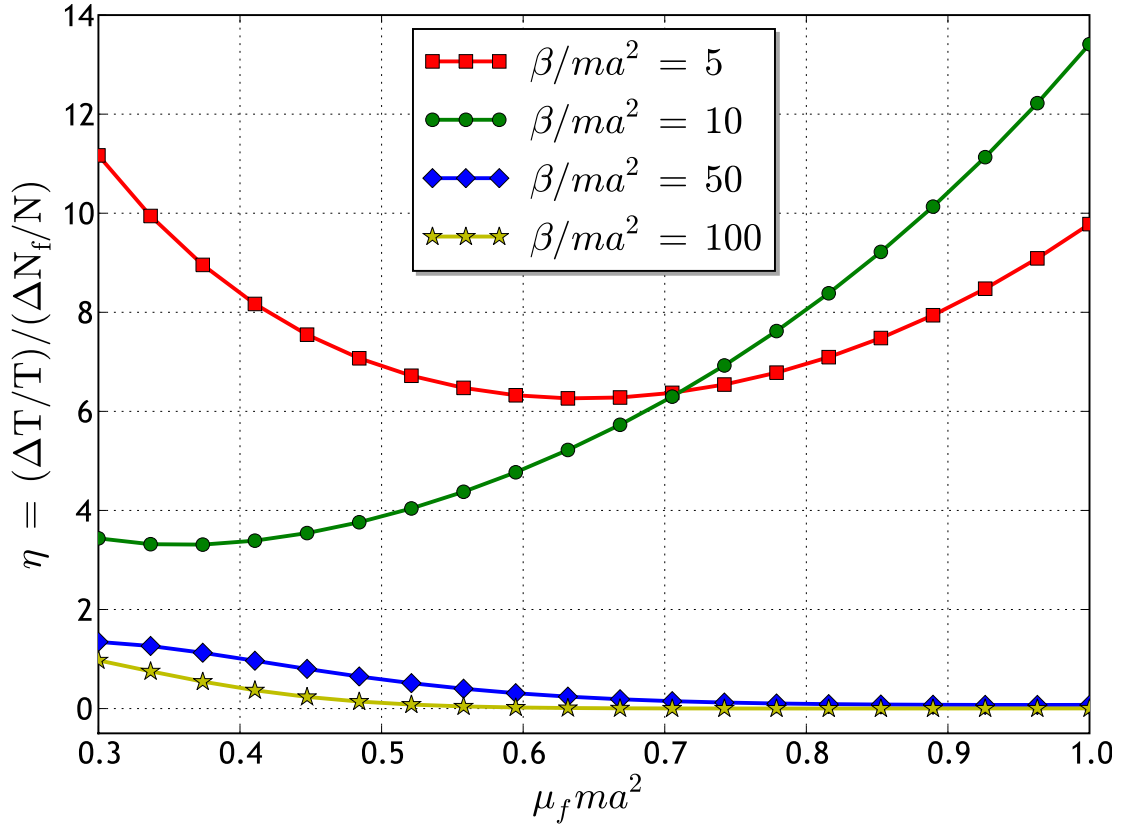


FIGURE 5.6: Cooling efficiency as defined in equation (5.9) and calculated by (5.11). As expected, it becomes harder to cool as the temperature drops. Also, these numbers do not include any loss mechanism other than pumping out the fermions.

Evaporative cooling (see appendix D.2) works by the expulsion of highly energetic particles and the thermal equilibration of the remaining cloud. In theory, an infinitely large η can be obtained by letting only particles with energy $\sim \eta k_B T$ escape. However, the fraction of particles expelled, $\sim \eta^{1/2} e^{-\eta}$, goes down exponentially and thus cooling time goes up exponentially with η . In practice, particle loss due to inelastic collisions always limits the cloud lifetime, setting a practical constraint on the maximum cooling time. Thus, η is limited by a competition between the loss of high-energy particles (that result in cooling) and the loss of all particles (due to inelastic scattering).

The same factors which limit η for evaporative cooling will also limit η in our scheme. In other words, $\Delta N/N$ can be broken down into $\Delta N_{\text{cooling}}/N + \Delta N_{\text{loss}}/N$, where the first

part results in cooling and the second part does not. So far, we've only calculated η due to the first part. To calculate the second part, we note that for fermions deep in the BEC side of resonance, the three main loss mechanisms are (i) background loss due to imperfect vacuum around the trap and laser fluctuations, (ii) three-body inelastic collisions $F + F + F' \rightarrow F + (FF')$, where F and F' are fermions in different states and (FF') is a bound molecular state, and (iii) two body inelastic collisions such as $(FF') + F \rightarrow (FF')_- + F$ or $(FF') + (FF') \rightarrow (FF')_- + (FF')$ where $(FF')_-$ is a deeply bound molecular state. The particle loss rate due to these processes needs to be compared with the pumping rate. After estimating the maximum possible pumping rate in § 5.5, we will analyze how it compares with inherent particle loss mechanisms (§ 5.5.1, 5.5.2 and 5.5.3).

5.5 Cooling geometry, or the nuts and bolts

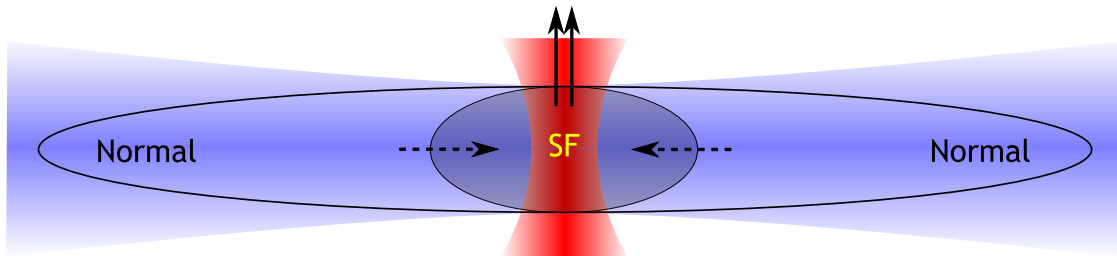


FIGURE 5.7: Pumping scheme to achieve cooling. The solid arrows denote removal of fermions from the superfluid (SF) shell in the center, while the dashed arrows denote diffusion of fermions from the normal to the superfluid phase at the boundary. The blue shading is the trapping laser, while the red shading, as will be explained below, is the evaporating or pumping laser.

For the above-mentioned scheme to work, we need to selectively pump out fermions from the superfluid region (figure 5.7), which lies at the center of the trap. It is noteworthy that even without the mechanism we're describing, removing atoms may cool or heat the gas, in part depending on the energy distribution of the particles removed. Close to Fermi degeneracy, for example, all fermions have energies close to $3\epsilon_F/5$, so removing

some has a minimal effect on the temperature. Far above Fermi degeneracy, removing particles with $\epsilon \gg k_B T$ cools the gas while removing particles with $\epsilon \ll k_B T$ heats it.

For pumping out fermions from the superfluid region, we propose driving a Raman transition between $|1/2, +1/2\rangle$ and $|3/2, +1/2\rangle$ using two counterpropagating lasers at slightly different frequencies. The two-photon momentum kick will be sufficient for expelling a light atom such as ${}^6\text{Li}$ from the trap.

As we'll see in chapter 6, atoms (fermions) and molecules (bosons) can be spectroscopically distinguished due to the binding energy of the latter, and hence one might think that a simpler, single photon mechanism such as an RF pulse or a laser tuned at the right frequency can selectively target fermions in the red shaded region in figure 5.7. This, however, is not feasible. At an operating point of 765 Gauss (justified later), the binding energy between $|1/2, +1/2\rangle$ and $|1/2, -1/2\rangle$ is 16.14 KHz, while the natural linewidth of the 671 nm (447 THz) $2S_{1/2} \rightarrow 2P_{3/2}$ optical transition is almost 6 MHz [26]. Therefore, a single-photon optical transition would not be selective enough to knock the fermions out. On the other hand, although the 300 MHz splitting between $|F = 1/2\rangle$ and $|F = 3/2\rangle$ [26] allows for a narrow RF transition, such a transition would not give enough recoil kick to the fermion to expel it from the cloud.

A two-photon Raman transition between $|1/2, +1/2\rangle$ and $|3/2, +1/2\rangle$ would allow both a narrow linewidth as well as a big recoil kick. At 765 Gauss, the difference in those energy levels is about 2 GHz [183, 184], so the linewidth is $6 \text{ MHz} \times (2 \text{ GHz}/447 \text{ THz})^3 = 0.54 \text{ nHz}$. While in reality the linewidth is larger than this ideal value, it's still less than a Hz, so specifically targetting the fermions with a Raman transition is entirely possible. The recoil temperature of ${}^6\text{Li}$ from a 671 nm photon is 3.5 μK , which is already much higher than the trap depth, so the recoil from two of those photons will be more than sufficient to knock it out of the trap.

While the bound and unbound fermions can be spectrally distinguished, the Raman lasers couple equally well to fermions everywhere in the trap. This is a consequence of the fact that the difference between the AC Stark shifts of $|1/2, +1/2\rangle$ and $|3/2, +1/2\rangle$ would be the same throughout the trap. By focusing the lasers, one can crudely target some regions spatially. In particular, we saw in chapter 4 that the superfluid phase occupies most of the volume near the trap center (e.g., figure 4.3). Thus, if we train our “evaporating” lasers crosswise (perpendicular to the long axis) through the center of the trap, most – if not all – of the fermions we kick out will be from the superfluid phase.²

The transfer of atoms from the normal to the superfluid phase is not instantaneous, and our calculation is only valid if we pump atoms out slower than the equilibration rate of the cloud. The cooling rate is limited by the time a cloud of fermions in a harmonic trap take to equilibrate after being depleted from the center. In the strongly interacting regime, transport is diffusive; the equilibration time will be determined by the diffusion coefficient, which in turn depends on the fermion scattering rate.

For a bose-fermi mixture with spin-polarized fermions at low temperatures, the fermions can relax only by collision with the bosons. The collision rate per fermion (or the inverse of the mean free time) is given by[185]

$$\Gamma_f = \frac{1}{\eta} n_b \sigma_{bf} v_{bf}$$

where $\sigma_{bf} = 4\pi a_{bf}^2 = 4\pi a^2 \lambda_f^2$ is the bose-fermi scattering cross section and $v_{bf} = (8k_B T / \pi \mu)^{1/2}$ is the thermally averaged relative collision speed between bosons and fermions with the reduced mass $\mu = m_f m_b / (m_f + m_b) = 2m/3$. For $m_f = m_b/2$, the dimensionless parameter $\eta \approx 2$ [186]. To be sufficiently deep in the BEC phase, we can choose $k_{F\uparrow} a = 1$ [170]

²Another geometry could be to use a spatial separation of the normal and superfluid phases. As seen in recent experiments[127], in an optical trap with an additional off-center magnetic trap, the superfluid and normal phases are spatially separated with a flat boundary between them. Such a profile would make it easier to target only the superfluid phase for evaporation. Further, double-well traps could possibly be engineered where the two phases reside primarily in two different potential minima, but to date we do not know of anyone of having actually done such an experiment.

where $k_{F\uparrow}^3 = 6\pi^2 n_\uparrow$. Then $\beta = 2T_{F\uparrow}/T$, and the collision rate becomes

$$\Gamma_f = 4\epsilon_{F\uparrow}(n_b a^3)\lambda_f^2 \left(\frac{12\pi}{\beta}\right)^{1/2} \quad (5.12)$$

The diffusion constant $D = v_{bf}^2/3\Gamma_f$ is given by Fermi liquid theory as

$$D = \frac{1}{m(3\pi^2\beta)^{1/2}(n_b a^3)\lambda_f^2} \quad (5.13)$$

As shown in detail in appendix F, the upper limit on the pumping rate with this diffusion constant is

$$\frac{dN}{dt} = \omega_r \frac{8\sqrt{2/3}(\alpha^2 - 1)(n_c a^3)(\omega_F/\omega_r)^2}{\alpha^2\beta\lambda_f^2(n_b a^3)} \quad (5.14)$$

where $\alpha = \omega_r/\omega_z$, ω_r (ω_z) being the radial (axial) trapping frequency of a cigar-shaped harmonic trap, $\omega_F = \epsilon_{F\uparrow}/\hbar$, and n_c is the central density of excess fermions.

To use our results for $\beta = 10$ we choose $T = T_F/5$, which also ensures the existence of a Bose condensate in the fermion-poor phase. To find the operating point on the $\beta = 10$ curve of figure 5.4, we note that on the normal side $(n_f + n_b)a^3 = 1/6\pi^2$, which happens at $\mu_f m a^2 = 0.374$. At that point, on the superfluid side $n_b a^3 = 0.03$. For typical central densities of $n_\uparrow \sim 10^{18} \text{ m}^{-3}$ for ${}^6\text{Li}$ [2, 74], we get $\epsilon_F \approx 600 \text{ nK} \approx 13 \text{ KHz}$. For these parameters and $\alpha = 45$, $n_c/n_b \approx 0.07$, $\omega_r = 2\pi \times 325 \text{ Hz}$ [2],

$$\frac{dN}{dt} \approx 10^5 \text{ s}^{-1} \quad (5.15)$$

This is an optimistic upper limit because of certain simplifying assumptions made in appendix F, such as the number in the bleached region being equal to the central density times some fixed width.³ Nevertheless, this tells us that we can pump $\sim 10^5$ particles per second while keeping the system in local equilibrium. The practicality of this cooling scheme rests on the comparison between the rate in (5.15) and the loss rates listed in § 5.4.

³Another very important assumption made in appendix F is that once the center is depleted, fermions from all over the trap flow in to restore the central density. In practice, the fermions in the edge (normal phase) are collisionless, and will therefore have a low diffusion coefficient. If we only consider the trap to extend to the edge of the superfluid state (which is equivalent to using $\omega_z \approx 2\pi \times 15 \text{ Hz}$ or $\alpha \approx 22$) [2], then this upper limit is reduced by a few percents.

5.5.1 Background loss

At a pressure of 10^{-9} Torr, typical of cold gas experiments, the ambient air density is $n \approx 3.5 \times 10^{13} \text{ m}^{-3}$, and the thermal velocity at 300 K is $v \approx 700 \text{ m/s}$. The scattering cross section between a cold atom and an air molecule is just their area, which is $\sim (1\text{\AA})^2$, and given that there are typically 10^5 particles in a trap, the total cross section is $\sigma = 10^{-15} \text{ m}^2$. Therefore, the background scattering rate is

$$\Gamma_{\text{back}} = n\sigma v = 24.5 \text{ s}^{-1} \quad (5.16)$$

For a trap with 10^5 particles at the start, the initial particle loss rate due to background scattering would be ~ 4000 per second. This rate is much lower than the rate from (5.15), and can thus be neglected. In typical experiments, the background decay rate is several tens of seconds[187], and is almost never a limiting factor on the cloud lifetime.

5.5.2 Three-body collisions

On the BEC side, the number of three-body recombinations $\uparrow + \uparrow + \downarrow \rightarrow \uparrow\downarrow + \uparrow$ per unit time per unit volume is[188]

$$\Gamma_{3\text{-body}} \approx \frac{681a^6}{m} n_{\uparrow}^{8/3} n_{\downarrow}$$

while the spin-flipped version $\uparrow + \downarrow + \downarrow \rightarrow \uparrow\downarrow + \downarrow$ has the same rate with the spin indices flipped. Since for our system there are no excess \downarrow -spins, i.e., $n_{\downarrow} = 0$, this recombination rate is zero, and we do not have to worry about this loss mechanism.

5.5.3 Two-body collisions

Two-body collisions can be either fermion-boson or boson-boson. In both cases, one of the resulting components is a deeply bound molecule, denoted $(\uparrow\downarrow)_-$. Near a Feshbach resonance on the BEC side, the collision rates are proportional to $a^{-3.33}$ for $\uparrow + \uparrow\downarrow \rightarrow \uparrow + (\uparrow\downarrow)_-$ events and $a^{-2.55}$ for $\uparrow\downarrow + \uparrow\downarrow \rightarrow \uparrow\downarrow + (\uparrow\downarrow)_-$ events [180]. The proportionality constants are system-dependent, and this stabilization of dimers near a Feshbach resonance have been observed experimentally for ${}^6\text{Li}_2$ [107, 108] and ${}^{40}\text{K}_2$ [189].

At given densities, $k_{F\uparrow}a = 1$ is achieved at 765 Gauss, where the 2-body scattering lifetime $\tau_{2\text{-body}}$ was observed to be ≥ 10 s [108]. In other words,

$$\frac{dN_{2\text{-body}}}{N} = -\frac{dt}{\tau_{2\text{-body}}} \quad (5.17)$$

So if we start with $\sim 10^5$ fermions in our trap, we will start losing particles at 10^4 per second due to this effect.

Comparing the three loss mechanisms above with the possible pumping rate in (5.15), we can see that if in a given time ΔN_f fermions are pumped out by a laser, another $\approx 0.1\Delta N_f$ will be lost to inelastic two-body collisions. In other words, in (5.11), we need to multiply the denominator by 1.1 to account for losses. This will reduce all the η -s in figure 5.6 by 9%. So for example for $\beta = 10$ and $\mu_f m a^2 = 0.37$, with losses, $\eta = 3.0$ instead of 3.3. While this is slightly lower than good evaporative cooling schemes, the fact that this scheme kicks in after the evaporative stage still makes this a viable final stage.

CHAPTER 6

FINAL-STATE EFFECTS IN THE RF SPECTRUM OF STRONGLY INTERACTING FERMIONS

*This chapter was adapted from “Final-State Effects in the Radio Frequency Spectrum of Strongly Interacting Fermions” by Sourish Basu and Erich J. Mueller, published in Physical Review Letters **101**, 060405 (2008) [190].*

Can pairing between fermions be detected by spectroscopy? Spectroscopy is routinely employed to characterize the rotational and vibrational states of molecules [191] (many of which are difermionic), and a spectroscopic measurement of the superconducting gap in a traditional superconductor was one of the first validations of the BCS theory [88, 89]. One should therefore be able to detect the formation of fermion pairs in cold atomic gases in the BEC-BCS crossover region by spectroscopy. In the presence of pairs, the spectrum of such a gas should consist of a sharp symmetric peak corresponding to an excitation of the free fermions, and an asymmetric continuum due to the dissociation of pairs.

Markus Greiner and colleagues used this idea to demonstrate the formation of $^{40}\text{K}_2$ molecules on the BEC side of a Feshbach resonance [192]. At $T > T_{\text{BEC}}$, their trap held a mixture of atoms and molecules in chemical equilibrium, which yielded a temperature-broadened bimodal radio-frequency (RF) spectrum: a relatively sharp peak from the excitation of the atoms, and a broader peak from the dissociation of the molecules. The offset between the two was a measure of the binding energy, which agreed with a simple two-body calculation of molecular binding energy (appendix G).

Later experiments observed similar bimodal spectra on the BCS side [116, 193], and by analogy interpreted them to be signatures of Cooper pairing. This interpretation was bolstered by theoretical calculations showing that finite temperature paired fermions in

a trap would indeed exhibit a bimodal spectrum [194, 195]. However, that conclusion has been called into question recently with the discovery that even an unpaired Fermi gas at a finite temperature can give rise to a bimodal spectrum, purely by being in a trap [196, 197].

The question of whether fermion pairing has a spectroscopic signature can be settled if the signals from different density regions, or different parts of the trap, can be tomographically resolved. One way of doing this for a cylindrically symmetric trap is via an inverse Abel transform, which gives us density-resolved spectra at the cost of lower signal to noise [132].

Interpreting the tomographic spectra of [132], and later [80], was non-trivial because of final-state interactions; instead of two strongly interacting fermionic species, experiments [80, 116, 132] were done in a regime where there were three strongly interacting fermionic states, due to the presence of several close-by Feshbach resonances.

In this chapter, we present a theory of RF spectra in the presence of final state interactions across the BEC-BCS crossover region. Depending on the parameter range, a spectrum of a homogeneous system can be unimodal or bimodal at $T = 0$. In particular, on the BCS side the spectrum need not always be bimodal despite the existence of Cooper pairs. We identify the physical processes behind the peaks and continua, and place experiments [80, 116, 132] in their proper regions in the parameter space of interactions.¹

¹The chronology of events that led up to this is interesting. We initially tried to explain the distinctly non-BCS lineshapes of [132], in part motivated by the explanation of [116] on the BEC side. After going through with the theory, we discovered an additional feature, viz. a symmetric δ -function peak, that [132] had not observed. Some months later, Wolfgang Ketterle presented RF spectra at a conference that had an unexplained feature: a symmetric peak! They were exactly where we expected them to be. Happy coincidence prevailed, and we published our results [190] almost simultaneously with [80].

6.1 Introduction

Radio frequency (RF) spectroscopy may become a powerful probe of the many-body state of a gas of cold atoms. One indicator of this potential is the sharpness of hyperfine spectral lines [198]: orders of magnitude smaller than the ~ 100 kHz interaction strengths found in interacting clouds of lithium atoms. As cold atom experiments begin probing exotic states of matter, this separation of energy scales may allow one to detect subtle atomic correlations.

Despite this optimistic viewpoint, there appears to be major theoretical holes in our understanding of RF spectra, even at a qualitative level. The primary difficulty is that when radio waves change the hyperfine spin of an atom, the entire many-body state needs to adjust. Including these final state interactions is a nontrivial many-body problem, akin to the one which must be solved to understand the X-ray spectra of metals [199]. These are hard problems – there is no generic prescription for including these final state interactions, rather the solution will depend on the system at hand. Here we present a variational calculation in which we calculate the radio frequency spectrum of a strongly interacting superfluid two-component Fermi gas, including arbitrarily strong short range interactions in the final state. We find structure in the spectra which have not previously been theoretically described.

We consider a model where a gas of neutral Fermions occupy two different hyperfine states $|1\rangle$ and $|2\rangle$. Radio waves drive a transition from $|2\rangle$ to a new hyperfine state $|3\rangle$. Interactions between atoms in the three states are described by scattering lengths a_{12} , a_{13} , and a_{23} .

Previous approaches to understanding the RF spectrum of a superfluid Fermi gas have either neglected final state interactions [137, 194–196, 200], or included them with

sum rules [201–203], diagrammatics [204], or energy arguments [197]. Many of these previous works focussed on trying to gain quantitative understanding of the spectra for very specific parameter values. Here we present a straightforward variational approach which complements these other works: we focus on gaining a global picture of the qualitative structure of the RF spectrum for all parameter values. While elementary, our formalism is quite powerful – as was kindly pointed out to us by Giancarlo Strinati, it is equivalent to the zero-temperature limit of the BCS-RPA theory used by Perali et al. [204] to explore the unitary limit.

Final state interactions can qualitatively change the RF spectrum. For example, in early experiments [184] with the three lowest hyperfine states of Lithium atoms ², final state interactions nearly canceled out the contribution from interactions in the initial state. This is due to the proximity of three wide Feshbach resonances: $B_{12} = 834\text{G}$ ($\Delta B_{12} = 300\text{G}$), $B_{13} = 690\text{G}$ ($\Delta B_{13} = 122\text{G}$) and $B_{23} = 811\text{G}$ ($\Delta B_{23} = 222\text{G}$). The scattering lengths, which diverge on resonance, all become large at the same time. When $a_{12} \approx a_{13}$, the interaction effects cancel [201]. Later experiments [116, 132, 192, 193, 205] found nontrivial spectra – some of which were used as evidence of pairing in these gases.

6.2 The model

Here we use a BCS ansatz for the initial state, and a restricted set of final states which includes only “coherent” excitations: the quasihole created in state $|2\rangle$ has the same momentum as the excited atom. The neglected excitations will shift our spectral lines and introduce broadening, however our approach should capture the qualitative features of the spectrum. Our approach is exact in the limiting case of $a_{12} = a_{13}$, where the spectrum is

² $|1\rangle, |2\rangle, |3\rangle = |1/2, 1/2\rangle, |1/2, -1/2\rangle, |3/2, -3/2\rangle$ where $|F, m_F\rangle$ are their zero-field quantum numbers

a single delta-function peak at its free space value. Furthermore, when $a_{13} = 0$, it reduces to the BCS result: a broad asymmetric peak corresponding to the breaking up of Cooper pairs. Generically we find a bimodal spectrum containing both the delta-function and the broad continuum, though for some parameter ranges the delta-function lies in the continuum and becomes significantly broadened, disappearing as $a_{13} \rightarrow 0$. These results mirror those in Chin and Julienne's study of the RF spectrum of a single molecule [205]. Interpreting the delta function peak as a "bound-bound" transition, we encounter final state pairs in parameter ranges where no free-space molecules exist.

We construct a "phase diagram" (figure 6.1) in the final interaction ($a_{13}k_F$) versus initial interaction ($a_{12}k_F$) plane, delineating the regions where we expect to see a bound-bound transition and where we do not. We also plot the interaction values used in three experiments [80, 116, 132]. The experimental observations are consistent with our predictions; in [132] no bound-bound transition is seen, while in [80] one is always seen.

We only consider the spectrum of the homogeneous gas (measurable tomographically [132]), and avoid discussing the trap averaged spectrum, where inhomogeneous broadening obscures the basic physics [197]. Further, we restrict ourselves to the $T = 0$ unpolarized case ($n_1 = n_2$).

The role of the hyperfine energies ϵ_j ($j=1,2,3$), is most transparent if we make the Canonical transformation to the field operators $\psi_{j,k} \rightarrow e^{-i\epsilon_j t} \psi_{j,k}$, to arrive at a Hamiltonian $\mathcal{H} = H + H_{\text{RF}}$ with $H = H_1 + H_2 + H_3 + H_{12} + H_{13}$,

$$H_j = \sum_k \epsilon_k \psi_{j,k}^\dagger \psi_{j,k} \quad (6.1)$$

$$H_{ij} = -\lambda_{ij} \sum_{kpq} \psi_{i,k}^\dagger \psi_{j,p}^\dagger \psi_{j,p-q} \psi_{i,k+q} \quad (6.2)$$

$$\begin{aligned} H_{\text{RF}} &= \sum_k (\psi_{3,k}^\dagger \psi_{2,k} e^{-i\omega t} + \psi_{2,k}^\dagger \psi_{3,k} e^{i\omega t}) \quad (6.3) \\ &= e^{-i\omega t} X + e^{i\omega t} X^\dagger, \end{aligned}$$

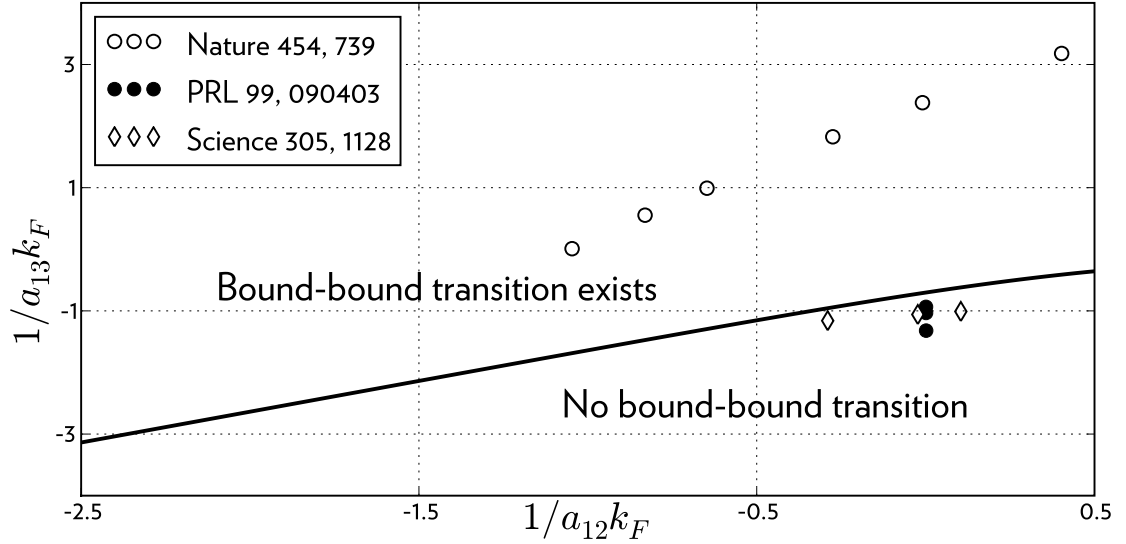


FIGURE 6.1: Phase diagram showing for which values of initial (a_{12}) and final (a_{13}) scattering lengths the homogeneous RF spectrum contains a bound-bound peak. Scattering lengths are normalized via the fermi wavevector, $k_F = (3\pi^2 n)^{1/3}$, where n is the atomic density. Symbols: parameters from lowest temperature data in the experiments – references [116], [132] and [80] correspond to open diamonds, closed circles, and open circles respectively.

We neglect the H_{23} term.³ The RF detuning is $\omega = \omega_{\text{RF}} - (\epsilon_3 - \epsilon_2)$ and the free particle dispersion is $\epsilon_k = k^2/2m - \mu$, where m is the atomic mass, and we use units where $\hbar = 1$. The interaction parameters λ_{ij} relate to the scattering lengths a_{ij} between states $|i\rangle$ and $|j\rangle$ by

$$\frac{1}{\lambda_{ij}} = -\frac{mV}{4\pi a_{ij}} + \sum_k \frac{m}{k^2} \quad (6.4)$$

where V is the spatial volume. Of particular importance is that if $\lambda_{12} = \lambda_{13}$, then $[X, H] = 0$, implying that the RF spectrum will consist of a single unshifted delta-function.

We make the variational ansatz that the system is initially in the BCS state

$$|\text{GS}\rangle = \prod_k (u_k + v_k \psi_{1,k}^\dagger \psi_{2,-k}^\dagger) |\text{vac}\rangle. \quad (6.5)$$

Minimizing $\langle H - \mu N \rangle$, and neglecting the Hartree terms [206] yields a ground state energy

³By the Pauli exclusion principle, the $|2\rangle$ atoms are spatially anticorrelated. To lowest order, the RF excitation will create $|3\rangle$ atoms which share these correlations, rendering negligible the impact of H_{23} .

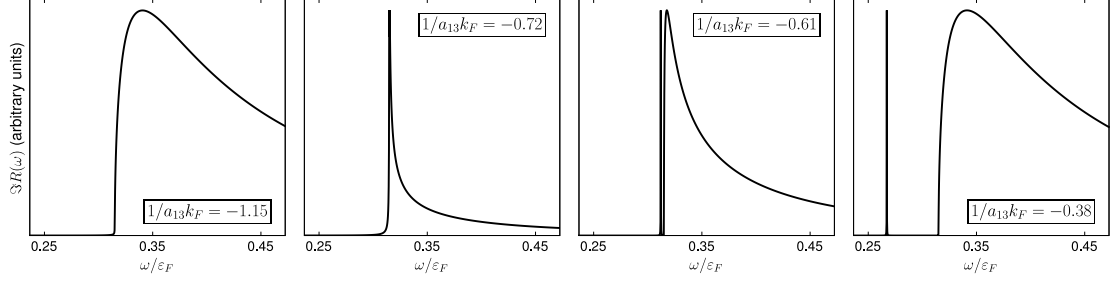


FIGURE 6.2: Theoretical radio frequency spectra at $a_{12} \rightarrow \infty$, where $k_F = (3\pi^2 n)^{1/3}$ and $\epsilon_F = k_F^2/2m$. The discrete peak on the right two figures correspond to a “bound-bound” transition between Cooper pairs in the various channels. Moving to the left, that peak merges with the continuum. The discrete peak has been scaled down for display; its actual spectral weight is shown in figure 6.4.

$E_{\text{GS}} = \langle H \rangle = \sum_k (\epsilon_k - E_k) + \Delta^2/\lambda_{12}$, with $v_k^2 = (E_k - \epsilon_k)/2E_k$, and $u_k^2 = (E_k + \epsilon_k)/2E_k$. The gap Δ obeys $\lambda_{12} \sum_k 1/2E_k = 1$ and the number of particles is $N = 2 \sum_k |v_k|^2$. The excitations will be described by quasiparticle operators $\gamma_k = u_k \psi_{1,k} - v_k \psi_{2,-k}^\dagger$ and $\eta_k = v_k \psi_{1,k}^\dagger + u_k \psi_{2,-k}$ with energies $E_k = \sqrt{(\epsilon_k - \mu)^2 + \Delta^2}$.

6.3 Spectral density

Fermi’s Golden rule states that given an RF detuning ω , the rate of transitions I to a set of final states $|f\rangle$ is given by the imaginary part of a spin response function,

$$\begin{aligned} I(\omega) &\propto \sum_f |\langle \text{GS} | H_{\text{RF}} | f \rangle|^2 \delta(\omega + E_{\text{GS}} - E_f) \\ &= \text{Im} \langle \text{GS} | X^\dagger \frac{1}{\omega - \bar{H}} X | \text{GS} \rangle = \text{Im} R(\omega), \end{aligned} \quad (6.6)$$

where $\bar{H} = H - E_{\text{GS}}$. We approximate this response by restricting the final states to those containing a single quasiparticle. By definition this captures the “coherent” part of the response where most of the spectral weight lies [207], and aside from the BCS ansatz is exact when $a_{13} = a_{12}$ or when $a_{13} = 0$. Introducing the *incomplete* but orthonormal set

of states

$$|k\rangle = \frac{1}{\nu_k} \Psi_{3,k}^\dagger \Psi_{1,k} |\text{GS}\rangle = -\Psi_{3,k}^\dagger \Upsilon_{-k}^\dagger |\text{GS}\rangle, \quad (6.7)$$

we replace the \bar{H} in (6.6) by $\tilde{H} = \sum_{k,k'} |k\rangle \bar{H}_{kk'} \langle k'|$, where $\bar{H}_{kk'} = \langle k | \bar{H} | k' \rangle = \delta_{kk'} (E_k + \epsilon_k) - \lambda_{13} u_k u_{k'}$. Matrix inversion gives

$$\begin{aligned} \frac{R(\omega)}{V} &= \frac{1}{V} \sum_{k,k'} \nu_k \nu_{k'} [(\omega - \tilde{H})^{-1}]_{kk'} \\ &= \frac{(2m\mu)^{3/2}}{(2\pi)^2 \mu} \left[G_3 + \frac{2}{\pi} \frac{\bar{\Delta}^2 G_2^2}{\frac{1}{a_{13}\sqrt{2m\mu}} + \frac{2}{\pi} G_1} \right]. \end{aligned} \quad (6.8)$$

In terms of scaled variables $\bar{\omega} = \omega/\mu$, $\bar{\Delta} = \Delta/\mu$ and $E_x = \sqrt{(x^2 - 1)^2 + \bar{\Delta}^2}$,

$$\begin{aligned} G_1 &= \int_0^\infty dx \left[-1 - \frac{x^2(E_x + x^2 - 1)}{E_x(\bar{\omega} - E_x - x^2 + 1)} \right], \\ G_2 &= \int_0^\infty \frac{x^2 dx}{E_x(\bar{\omega} - x^2 - E_x + 1)}, \\ G_3 &= \int_0^\infty x^2 dx \frac{E_x - x^2 + 1}{E_x(\bar{\omega} - E_x - x^2 + 1)}. \end{aligned} \quad (6.9)$$

As previously discussed, there are two contributions to the spectrum: a continuum from breaking up Cooper pairs, and a discrete peak from the conversion of a Cooper pair into a pair in the new channel. Mathematically, the continuum comes from the poles of the integrands of the G 's. Since we have severely restricted the available final states and neglected Hartree terms, the location of this continuum is independent of the final-state interactions and corresponds to all ω for which we can find a k with $\omega = E_k + \epsilon_k$: *ie.* $\omega > \sqrt{\Delta^2 + \mu^2} - \mu$. In a more sophisticated theory the threshold will depend on a_{13} . The discrete peak comes from the condition

$$\frac{1}{a_{13}\sqrt{2m\mu}} + \frac{2}{\pi} G_1 = 0. \quad (6.10)$$

This condition can only be satisfied for sufficiently strong interactions. In particular, if $a_{12} = \infty$, we find that this peak exists if $a_{13} > 0$ or if $a_{13}\sqrt{2m\mu} \lesssim -1$. In the former case the excited state can be thought of as a molecular pair, but in the latter case it is more

analogous to a Cooper pair. When $a_{12} = a_{13}$, one can recognize that if one sets $\omega = 0$ in Eq. (6.10) one recovers the gap equation. In this limit all spectral weight resides in this zero-detuning peak.

In the BCS-BEC crossover, the chemical potential depends on interactions and density in a nontrivial way. Following convention we will quote our results in terms of the Fermi momentum of an ideal Fermi gas with the same density as the one we are considering, $k_F = (3\pi^2 n)^{1/3}$. In figures 6.2 and 6.3 (top) we illustrate the a_{13} dependence of the spectrum by showing the spectral density when $a_{12} = \infty$. As figures 6.1, 6.2 and 6.3 reveal, the pair-pair transition peak breaks off from the continuum around $a_{13}k_F = -0.7$. As the solid line in figure 6.4 shows, most of the spectral weight is in that peak close to unitarity. For $0 < a_{13}k_F \ll 1$ (beyond the right hand edge of figures 6.3 (top) and 6.4) the spectral weight shifts back to the continuum. In that regime, the wavefunction overlap between the large $|1\rangle\text{-}|2\rangle$ Cooper pairs and the small $|1\rangle\text{-}|3\rangle$ molecules becomes negligible. Further, the spectral weight in the bound-bound peak goes to zero when it hits the continuum (left edge of the curves in figure 6.4), in agreement with [205]. Figure 6.3 (bottom) is similar to figure 6.3 (top), except that we show the a_{12} dependence of the spectrum keeping $a_{13} = \infty$.

We now discuss how the structure seen in figures 6.2 and 6.3 can be measured experimentally. First, since all physics only depends on the dimensionless parameters $a_{ij}k_F$ all interactions can be modified by changing the density. If $a_{12} = \infty$ then *only* the final state interaction is changed when the density is varied. This is a powerful knob: as seen in figure 6.1, two of the experiments [116, 132] have been performed very close to the point in Fig. 6.3 (top) where a bound-bound transition emerges from the continuum. A modest increase in density should allow the observation of this feature. Alternatively, one can produce different final state interactions by changing which internal states one uses in

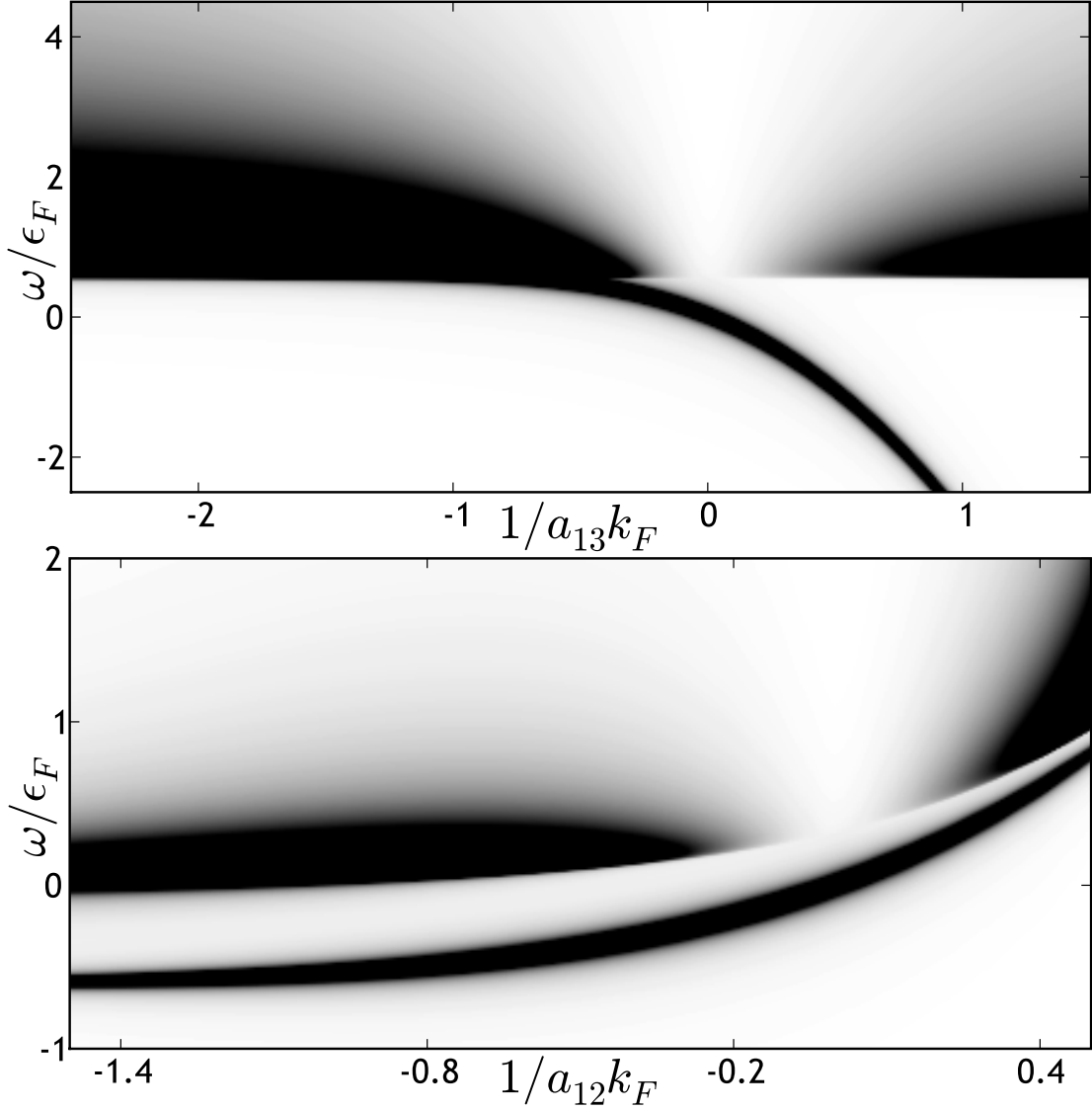


FIGURE 6.3: **[Top]** Spectral density as a function of final state scattering length a_{13} and RF frequency ω , when initial state interactions satisfy $a_{12} = \infty$. **[Bottom]** Same plot, except as a function of initial state scattering length a_{12} and ω with $a_{13} = \infty$. Spectral weight increases from white to black. The δ -function peak has been broadened to improve readability.

the experiment [80]. For Lithium ² in states $|1\rangle$, $|2\rangle$ and $|3\rangle$, one has six combinations: instead of a $|1\rangle|2\rangle$ superfluid, for example, one could take a $|2\rangle|3\rangle$ superfluid and excite $|2\rangle$ to $|1\rangle$. For the six possible combinations of pairing and excitation, final state interactions ($1/a_{\text{final}}k_F$) for typical central densities [132] are tabulated in table 6.1.

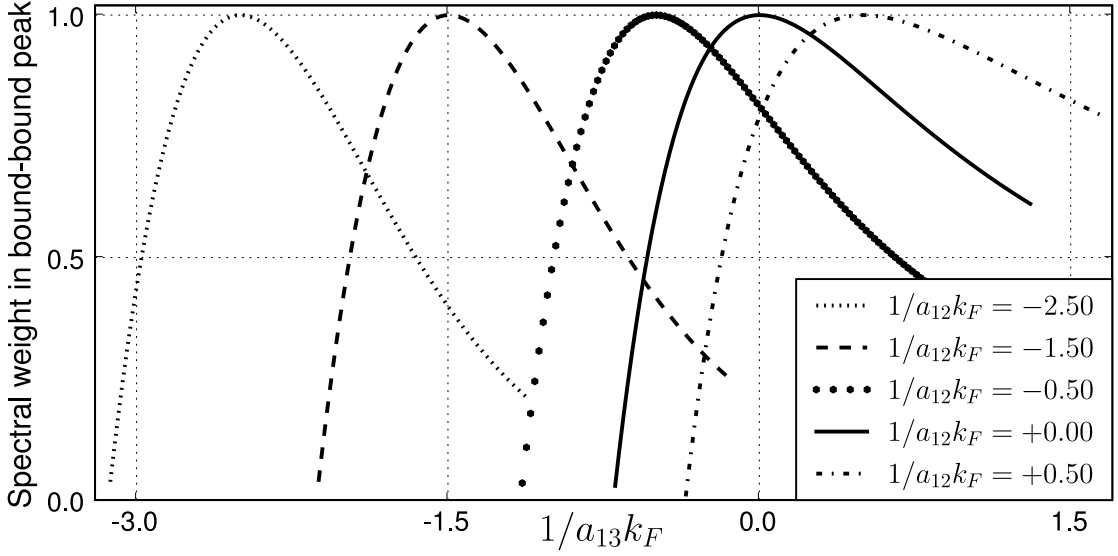


FIGURE 6.4: Fraction of spectral weight in the bound-bound peak as a function of final state interaction strength a_{13} , for different values of a_{12} . When the two interactions are equal, i.e., $a_{13} = a_{12}$, all the weight is in this peak.

TABLE 6.1: Final state interactions for different initial pairs and excitations at typical experimental densities [132]. For all cases, $1/a_{\text{initial}}k_F = 0$, i.e., the initial pair is at unitarity.

Initial pair	RF excitation	$1/a_{\text{final}}k_F$
12	2→3	-0.94
12	1→3	-0.19
13	1→2	2.58
13	3→2	2.14
23	2→1	-0.86
23	3→1	0.18

6.4 Quantitative accuracy

Motivated by refs. [201–203], we compute the zeroth and first moments of the resolvent R_{exact} , defined in eq (6.6), and our approximation, R_{approx} , from eq (6.8). The $|k\rangle$ basis is sufficiently large that the zeroth moment, or total spectral weight, is preserved by our

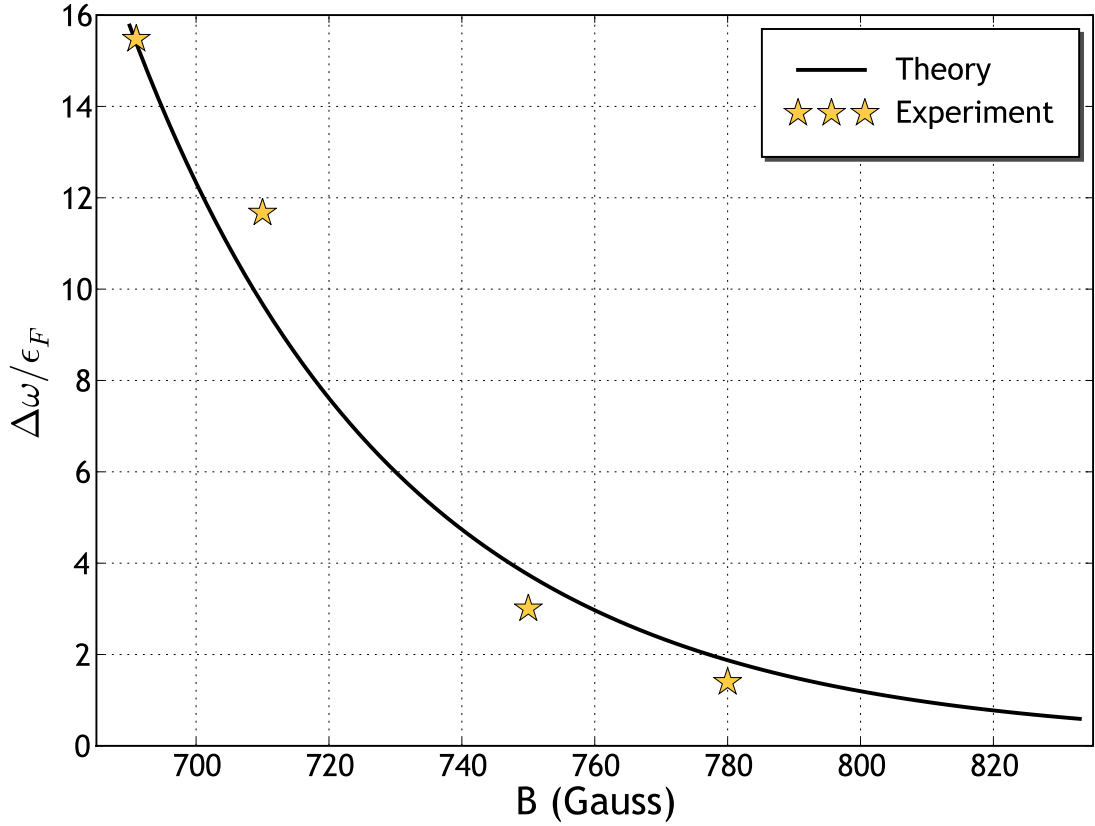


FIGURE 6.5: **Solid line:** separation between the “bound-bound” peak and the continuum from our theory, in units of the Fermi energy. **Stars:** Experimental data from [80]. This is a zero parameter fit, with density and magnetic field as the only inputs.

approximation,

$$\int_{-\infty}^{\infty} \frac{d\omega}{\pi} \mathcal{I}R_{\text{exact}}(\omega) = \langle \text{GS} | X^\dagger X | \text{GS} \rangle = \sum_k v_k^2 \quad (6.11)$$

$$\int_{-\infty}^{\infty} \frac{d\omega}{\pi} \mathcal{I}R_{\text{approx}}(\omega) = \sum_k |\langle k | X | \text{GS} \rangle|^2 = \sum_k v_k^2$$

The higher moments of both R_{exact} and R_{approx} are dominated by long tails which arise from the short distance structure of the BCS pairs. In the absence of final state interaction, for example, $R_{\text{approx}}(\omega) \propto \omega^{-3/2}$ for large ω . With final state interaction, $R_{\text{approx}}(\omega) \propto \omega^{-5/2}$ and our approach reproduces the first spectral moment in [201].

Finally we comment on the quantitative accuracy of our approach. The largest approximation that we make is the neglect of Hartree-type interactions. These terms will

shift the spectral lines. We also neglected incoherent processes which will broaden the spectra. Another important approximation was our neglect of finite temperature effects. These could be important in experiments where $T/T_F \sim 0.1$. Despite the severity of these approximations, we believe that our calculation is valuable for its simplicity. It illustrates the important physics in a transparent manner.

Quantitatively comparing our theory to experiments such as [80] is difficult because those experiments usually trap-average perpendicular to the long axis to improve their signal to noise ratio. However, in the regime where a bound-bound transition exists (upper half of figure 6.1) with a significant weight, even a trap averaged spectrum should show a peak and a continuum, with the peak heavily weighted by regions of high density at the center. We compare the separation between the peak and the continuum from our theory with data from [80] in figure 6.5. The agreement is quite good.

APPENDIX A

EVALUATION OF THE PHENOMENOLOGICAL FREE ENERGY

Here we detail how one calculates the Free energy of our pheonomological model for a general domain wall shape. We parameterize the boundary by $f = F(\theta)$, in terms of which the coordinates of the boundary are $\rho(\theta, f) = R_{\text{TF}} f \cos \theta$ and $z(\theta, f) = Z_{\text{TF}} f \sin \theta$.

The surface energy is

$$\begin{aligned}
 E_{\text{DW}} &= A_{dw} \int \left(1 - \frac{\rho^2}{R_{\text{TF}}^2} - \frac{z^2}{Z_{\text{TF}}^2} \right)^2 d^2 r \\
 &= 2A_{dw} \int_0^{\pi/2} d\theta F(\theta) \cos \theta \\
 &\quad \times [F'(\theta) \cos \theta - F(\theta) \sin \theta] \times [1 - F(\theta)^2]^2 \\
 &\quad \times \sqrt{1 + \left(\frac{Z_{\text{TF}}}{R_{\text{TF}}} \right)^2 \left(\frac{F'(\theta) \sin \theta + F(\theta) \cos \theta}{F'(\theta) \cos \theta - F(\theta) \sin \theta} \right)^2}
 \end{aligned} \tag{A.1}$$

where we define the coefficient

$$A_{dw} = \hbar \omega_z R_{\text{TF}}^2 Z_{\text{TF}} \left[\frac{2m}{\hbar^2} \right]^{3/2} \left[\frac{\eta \pi \mu_0^{3/2}}{(1 + \beta)^2 (3\pi^2)^{4/3}} \right]. \tag{A.2}$$

We write the free energy of the superfluid core as

$$\begin{aligned}
 \Omega_s &= A_s \int_s \rho d\rho dz \left(1 - \frac{\rho^2}{R_{\text{TF}}^2} - \frac{z^2}{Z_{\text{TF}}^2} \right)^{5/2} \\
 &= 2A_s \int_0^{\pi/2} d\theta \cos \theta \int_0^{F(\theta)} df f^2 (1 - f^2)^{5/2} \\
 &= 2A_s \int_0^{\pi/2} d\theta G_1[F(\theta)] \cos \theta
 \end{aligned} \tag{A.3}$$

$$A_s = -\zeta_s R_{\text{TF}}^2 Z_{\text{TF}} \left[\frac{2m}{\hbar^2} \right]^{3/2} \left[\frac{4\mu_0^{5/2}}{15\pi} \right] \tag{A.4}$$

$$\begin{aligned}
 G_1(x) &= \frac{1}{384} \left[x \sqrt{1 - x^2} (-15 + 118x^2 - 136x^4 + 48x^6) \right. \\
 &\quad \left. + 15 \sin^{-1}(x) \right]
 \end{aligned} \tag{A.5}$$

Similarly, the free energy of the fully polarized normal shell, $\Omega_N = A_n \int_n \rho d\rho dz (1 + \gamma - \rho^2/R_{TF}^2 - z^2/Z_{TF}^2)^{5/2}$, is:

$$\begin{aligned}\Omega_N &= 2A_n(1 + \gamma)^4 \left[\frac{5\pi}{256} - \int_0^{\pi/2} d\theta G_1 \left[\frac{F(\theta)}{\sqrt{1 + \gamma}} \right] \cos \theta \right] \\ A_n &= -\zeta_n R_{TF}^2 Z_{TF} \left[\frac{2m}{\hbar^2} \right]^{3/2} \left[\frac{4\mu_0^{5/2}}{15\pi} \right].\end{aligned}\quad (\text{A.6})$$

The total number of atoms in the two phases are given by

$$\begin{aligned}N_s &= 2B_s \int_0^{\pi/2} d\theta \cos \theta G_2[F(\theta)] \\ N_n &= 2B_n(1 + \gamma)^3 \left[\pi/32 - \int_0^{\pi/2} d\theta \cos \theta G_2 \left[\frac{F(\theta)}{\sqrt{1 + \gamma}} \right] \right]\end{aligned}\quad (\text{A.7})$$

where

$$\begin{aligned}B_{s,n} &= \zeta_{s,n} \frac{2}{3\pi} \left[\frac{2m\mu_0}{\hbar^2} \right]^{3/2} R_{TF}^2 Z_{TF} \\ G_2(x) &= \frac{1}{48} \left[x\sqrt{1 - x^2}(-3 + 14x^2 - 8x^4) + 3 \sin^{-1}(x) \right].\end{aligned}\quad (\text{A.8})$$

Thus both the free energy, and the constraints of fixed N and P reduce to one dimensional integrals.

APPENDIX B
BCS THEORY

The BCS theory has been extremely successful at describing conventional superconductors, and is also an accurate description of cold gases on the $a < 0$ side (therefore called the BCS side) of a Feshbach resonance, getting better farther from the resonance. Here we summarize the BCS theory for spin-polarized fermions. The BCS Hamiltonian is

$$\begin{aligned}\mathcal{H} &= \sum_{\mathbf{k},\sigma} \epsilon_{\mathbf{k}\sigma} \Psi_{\mathbf{k}\sigma}^\dagger \Psi_{\mathbf{k}\sigma} - \sum_{\mathbf{k}} \Delta_{\mathbf{k}} \Psi_{\mathbf{k}\uparrow}^\dagger \Psi_{-\mathbf{k},\downarrow}^\dagger - \sum_{\mathbf{k}} \Delta_{\mathbf{k}}^* \Psi_{-\mathbf{k}\downarrow} \Psi_{\mathbf{k}\uparrow} \\ \Delta_{\mathbf{k}} &= \sum_{\mathbf{k}'} U_{\mathbf{k}\mathbf{k}'} \langle \Psi_{-\mathbf{k}'\downarrow} \Psi_{\mathbf{k}'\uparrow} \rangle\end{aligned}\tag{B.1}$$

where $\epsilon_{\mathbf{k}\sigma}$ includes Hartree-Fock corrections to the free energy. In general, $\mu_\uparrow \neq \mu_\downarrow$ since their populations are different. This quadratic Hamiltonian can be diagonalized by the linear (Bogoliubov) transformation

$$\Psi_{\mathbf{k}\uparrow} = u_{\mathbf{k}}^* \gamma_{1,\mathbf{k}} + v_{\mathbf{k}} \gamma_{2,\mathbf{k}}^\dagger \quad \Psi_{\mathbf{k}\downarrow} = -v_{-\mathbf{k}} \gamma_{1,-\mathbf{k}}^\dagger + u_{-\mathbf{k}}^* \gamma_{-\mathbf{k},2}$$

where the coefficients follow $|u_{\mathbf{k}}|^2 + |v_{\mathbf{k}}|^2 = 1$ to satisfy fermionic commutation relations. Hence we can write express the coefficients as $u_{\mathbf{k}} = \cos \theta_{\mathbf{k}}$ and $v_{\mathbf{k}} = \sin \theta_{\mathbf{k}}$. The angles $\theta_{\mathbf{k}}$ are determined by the condition that this transformation diagonalizes \mathcal{H} , which for s-wave superconductors ($\Delta_{\mathbf{k}} = \Delta$) gives

$$\tan 2\theta_{\mathbf{k}} = \frac{2\Delta}{\epsilon_{\mathbf{k}\uparrow} + \epsilon_{\mathbf{k}\downarrow}}$$

The diagonalized Hamiltonian reads

$$\begin{aligned}\mathcal{H} &= \sum_{\mathbf{k}} \lambda_{1,\mathbf{k}} \gamma_{1,\mathbf{k}}^\dagger \gamma_{1,\mathbf{k}} + \sum_{\mathbf{k}} \lambda_{2,\mathbf{k}} \gamma_{2,\mathbf{k}}^\dagger \gamma_{2,\mathbf{k}} + \sum_{\mathbf{k}} \left[\bar{\epsilon}_{\mathbf{k}} - \sqrt{\bar{\epsilon}_{\mathbf{k}}^2 + \Delta^2} \right] + \frac{\Delta^2}{U} \\ \lambda_{[1,2],\mathbf{k}} &= \sqrt{\bar{\epsilon}_{\mathbf{k}}^2 + \Delta_{\mathbf{k}}^2} \pm \frac{\Delta_{\mathbf{k}} \epsilon_{\mathbf{k}}}{2}\end{aligned}\tag{B.2}$$

where we've assumed $U_{\mathbf{k}\mathbf{k}'} = U$ and defined $2\bar{\epsilon}_{\mathbf{k}} = \epsilon_{\mathbf{k}\uparrow} + \epsilon_{\mathbf{k}\downarrow}$, $\Delta_{\mathbf{k}} \epsilon_{\mathbf{k}} = \epsilon_{\mathbf{k}\uparrow} - \epsilon_{\mathbf{k}\downarrow} = \mu_\downarrow - \mu_\uparrow$. Densities ($n_\sigma = \sum_{\mathbf{k}} \langle \Psi_{\mathbf{k}\sigma}^\dagger \Psi_{\mathbf{k}\sigma} \rangle$) and other quantities can be calculated at finite temperature

using

$$\langle Y_{i,\mathbf{k}}^\dagger Y_{i,\mathbf{k}} \rangle = \frac{1}{e^{\beta\lambda_{i,\mathbf{k}}} + 1}$$

We quote the relevant expressions here for reference:

$$n_\uparrow = \frac{1}{2\pi^2} \left[\frac{2m}{\hbar^2\beta} \right]^{3/2} \int_0^\infty \frac{y^2 dy}{2} \frac{e^{\beta h/2} + \cosh E_y - (y^2 - \beta\bar{\mu}) \sinh E_y/E_y}{\cosh E_y + \cosh(\beta h/2)} \quad (\text{B.3})$$

$$n_\downarrow = \frac{1}{2\pi^2} \left[\frac{2m}{\hbar^2\beta} \right]^{3/2} \int_0^\infty \frac{y^2 dy}{2} \frac{e^{-\beta h/2} + \cosh E_y - (y^2 - \beta\bar{\mu}) \sinh E_y/E_y}{\cosh E_y + \cosh(\beta h/2)} \quad (\text{B.4})$$

$$\frac{1}{a} = -\frac{2}{\pi} \left[\frac{2m}{\hbar^2\beta} \right]^{1/2} \int_0^\infty y^2 dy \left[\frac{1}{E_y} \frac{\sinh E_y}{\cosh E_y + \cosh(\beta h/2)} - \frac{1}{y^2} \right] \quad (\text{B.5})$$

$$\begin{aligned} \frac{\langle \mathcal{H} \rangle}{\text{Vol}} = \frac{1}{2\pi^2\beta} \left[\frac{2m}{\beta\hbar^2} \right]^{3/2} & \left[\int_0^\infty y^2 dy \left\{ \frac{E_y (e^{-E_y} + \cosh(\beta h/2)) - (\beta h/2) \sinh(\beta h/2)}{\cosh E_y + \cosh(\beta h/2)} \right. \right. \\ & \left. \left. + y^2 - \beta\bar{\mu} - E_y + \frac{(\beta\Delta)^2}{2y^2} \right\} + \frac{\pi}{2a} (\beta\Delta)^2 \sqrt{\frac{\beta\hbar^2}{2m}} \right] \end{aligned} \quad (\text{B.6})$$

where $\bar{\mu} = \mu_\uparrow + \mu_\downarrow$ and $E_y = \sqrt{(y^2 - \beta\bar{\mu})^2 + (\beta\Delta)^2}$. Equation (B.5) is called the *gap equation*, since solving that at fixed temperature $1/\beta$ and scattering length a gives the gap Δ . On the other hand, solving equation (B.5) with $\Delta = 0$ gives the transition temperature $1/\beta_c$ as a function of a . To characterize the phase transition from $\Delta = 0$ to $\Delta \neq 0$, we need to construct the free energy as a function of Δ .

$$\mathcal{F} = -\frac{1}{\beta} \log \text{Tr} e^{-\beta\mathcal{H}} \quad (\text{B.7})$$

Since \mathcal{H} is quadratic in the Bogoliubons, this can be calculated analytically. After the smoke clears, we're left with

$$\begin{aligned} \frac{\mathcal{F}}{\text{Vol}} = \frac{1}{2\pi^2\beta} \left[\frac{2m}{\hbar^2\beta} \right]^{3/2} & \left[\int_0^\infty dy \left[\frac{1}{2} (\beta\Delta)^2 + y^2 (y^2 - \beta\bar{\mu}) \right. \right. \\ & \left. \left. - y^2 \log \left\{ 2 \cosh E_y + 2 \cosh \frac{\beta h}{2} \right\} \right] + \frac{\pi}{2a} (\beta\Delta)^2 \sqrt{\frac{\beta\hbar^2}{2m}} \right] \end{aligned} \quad (\text{B.8})$$

At low temperatures (figure B.1 left), this \mathcal{F} has two minima in Δ , one of them $\Delta = 0$, and the transition between them is discontinuous. Above a temperature specified by $[\mathcal{F}''(\Delta = 0)/\Delta]_{\Delta=0} = 0$, the transition is continuous from $\Delta = 0$ to $\Delta \neq 0$ (figure B.1 right). At $T = 0$, $h = 0$ and $a \rightarrow \infty$, the gap can only depend on the density, and in

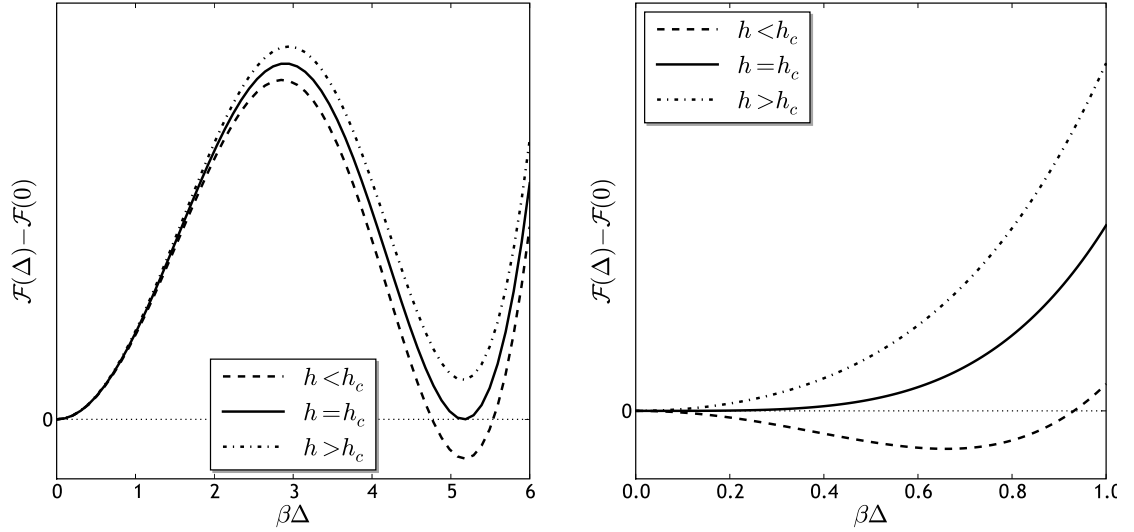


FIGURE B.1: \mathcal{F} from (B.8) at unitarity. **Left:** At low temperature, $\mathcal{F}(\Delta) - \mathcal{F}(0)$ has two minima. As the chemical potential mismatch h crosses a threshold h_c , the order parameter Δ jumps discontinuously from a finite value to zero. **Right:** At high temperature above the tricritical point, the phase transition is continuous at h_c .

fact $\Delta = 1.16\bar{\mu}$. The chemical potential mismatch h_c after which there's a discontinuous transition from the superconducting to the normal state ($\Delta = 0$) is called the Clogston limit, and at $T = 0$, $a \rightarrow \infty$, $h_c = 1.6\bar{\mu}$.

APPENDIX C

THE HUBBARD-STRATONOVICH TRANSFORMATION

The Hubbard-Stratonovich transformation is used to eliminate a pair of fermionic fields in favor of a single bosonic field. The usual point-interaction Hamiltonian

$$\mathcal{H} = \sum_{\mathbf{k}\sigma} \epsilon_{\mathbf{k}\sigma} \Psi_{\mathbf{k}\sigma}^\dagger \Psi_{\mathbf{k}\sigma} - V \sum_{\mathbf{k}\mathbf{k}'\mathbf{q}} \Psi_{\frac{\mathbf{q}}{2}+\mathbf{k}'\uparrow}^\dagger \Psi_{\frac{\mathbf{q}}{2}-\mathbf{k}'\downarrow}^\dagger \Psi_{\frac{\mathbf{q}}{2}-\mathbf{k}\downarrow} \Psi_{\frac{\mathbf{q}}{2}+\mathbf{k}\uparrow}$$

provides an ideal test case. The partition function for this Hamiltonian can be written as

$$\begin{aligned} \mathcal{S} &= \int_0^\beta d\tau \sum_{\mathbf{k}\sigma} \Psi_{\mathbf{k}\sigma}^\dagger \partial_\tau \Psi_{\mathbf{k}\sigma} - \int_0^\beta d\tau \mathcal{H} \\ \mathcal{Z} &= \int \left\{ \prod_{\mathbf{k}\sigma} d\Psi_{\mathbf{k}\sigma} d\Psi_{\mathbf{k}\sigma}^* \right\} e^{\mathcal{S}} \end{aligned} \quad (\text{C.1})$$

Using the identity

$$\frac{\pi}{\alpha} \int dz dz^* e^{-\alpha|z|^2} = 1 \quad (\text{C.2})$$

we write unity in terms of an arbitrary scalar function $\Delta_{\mathbf{k}}$:

$$\left[\prod_{\mathbf{k}} \frac{\alpha_{\mathbf{k}}}{\pi} \right] \int \left\{ \prod_{\mathbf{k}} d\Delta_{\mathbf{k}} d\Delta_{\mathbf{k}}^* \right\} e^{-\sum_{\mathbf{k}} \alpha_{\mathbf{k}} |\Delta_{\mathbf{k}}|^2} = 1 \quad (\text{C.3})$$

Since the integral over $\Delta_{\mathbf{k}}$ spans the entire scalar space, this result holds even if we shift $\Delta_{\mathbf{k}}$ by any arbitrary amount, in particular:

$$\begin{aligned} \Delta_{\mathbf{k}} &\rightarrow \Delta_{\mathbf{k}} - V \sum_{\mathbf{q}} \Psi_{\frac{\mathbf{k}}{2}-\mathbf{q}\downarrow} \Psi_{\frac{\mathbf{k}}{2}+\mathbf{q}\uparrow} \\ \therefore |\Delta_{\mathbf{q}}|^2 &\rightarrow |\Delta_{\mathbf{q}}|^2 - V \Delta_{\mathbf{q}}^* \sum_{\mathbf{k}'} \Psi_{\frac{\mathbf{q}}{2}-\mathbf{k}'\downarrow} \Psi_{\frac{\mathbf{q}}{2}+\mathbf{k}'\uparrow} - V \Delta_{\mathbf{q}} \sum_{\mathbf{k}} \Psi_{\frac{\mathbf{q}}{2}+\mathbf{k}\uparrow}^* \Psi_{\frac{\mathbf{q}}{2}-\mathbf{k}\downarrow}^* \\ &\quad + V^2 \sum_{\mathbf{k}\mathbf{k}'} \Psi_{\frac{\mathbf{q}}{2}+\mathbf{k}\uparrow}^* \Psi_{\frac{\mathbf{q}}{2}-\mathbf{k}\downarrow}^* \Psi_{\frac{\mathbf{q}}{2}-\mathbf{k}'\downarrow} \Psi_{\frac{\mathbf{q}}{2}+\mathbf{k}'\uparrow} \end{aligned} \quad (\text{C.4})$$

If we multiply the partition function by unity as defined in (C.3) with the shift defined in (C.4), we get

$$\begin{aligned}
Z &= \int \left\{ \prod_{\mathbf{k}\sigma} d\psi_{\mathbf{k}\sigma} d\psi_{\mathbf{k}\sigma}^* \right\} \left\{ \prod_{\mathbf{p}} d\Delta_{\mathbf{p}} d\Delta_{\mathbf{p}}^* \right\} e^S \\
S &= \int_0^\beta d\tau \sum_{\mathbf{k}\sigma} \psi_{\mathbf{k}\sigma}^* (\partial_\tau - \epsilon_{\mathbf{k}\sigma}) \psi_{\mathbf{k}\sigma} + V \int_0^\beta d\tau \sum_{\mathbf{q}\mathbf{k}\mathbf{k}'} \psi_{\frac{\mathbf{q}}{2}+\mathbf{k}\uparrow}^* \psi_{\frac{\mathbf{q}}{2}-\mathbf{k}\downarrow}^* \psi_{\frac{\mathbf{q}}{2}-\mathbf{k}'\downarrow} \psi_{\frac{\mathbf{q}}{2}+\mathbf{k}'\uparrow} \\
&\quad - \int_0^\beta d\tau \sum_{\mathbf{p}} \alpha_{\mathbf{p}} |\Delta_{\mathbf{p}}|^2 + V \sum_{\mathbf{p}} \int_0^\beta d\tau \alpha_{\mathbf{p}} \Delta_{\mathbf{p}}^* \sum_{\mathbf{k}'} \psi_{\frac{\mathbf{p}}{2}-\mathbf{k}'\downarrow} \psi_{\frac{\mathbf{p}}{2}+\mathbf{k}'\uparrow} \\
&\quad + V \sum_{\mathbf{p}} \int_0^\beta d\tau \alpha_{\mathbf{p}} \Delta_{\mathbf{p}} \sum_{\mathbf{k}} \psi_{\frac{\mathbf{p}}{2}+\mathbf{k}\uparrow}^* \psi_{\frac{\mathbf{p}}{2}-\mathbf{k}\downarrow}^* \\
&\quad - V^2 \sum_{\mathbf{p}} \alpha_{\mathbf{p}} \int_0^\beta d\tau \sum_{\mathbf{k}\mathbf{k}'} \psi_{\frac{\mathbf{p}}{2}+\mathbf{k}\uparrow}^* \psi_{\frac{\mathbf{p}}{2}-\mathbf{k}\downarrow}^* \psi_{\frac{\mathbf{p}}{2}-\mathbf{k}'\downarrow} \psi_{\frac{\mathbf{p}}{2}+\mathbf{k}'\uparrow}
\end{aligned} \tag{C.5}$$

This is true for any $\alpha_{\mathbf{k}}$, and in particular for $\alpha_{\mathbf{p}} = 1/V$. This choice gets rid of the interaction term, leaving us with

$$\begin{aligned}
S &= \underbrace{\int_0^\beta d\tau \sum_{\mathbf{k}\sigma} \psi_{\mathbf{k}\sigma}^* (\partial_\tau - \epsilon_{\mathbf{k}\sigma}) \psi_{\mathbf{k}\sigma}}_{S_0} - \frac{1}{V} \int_0^\beta d\tau \sum_{\mathbf{q}} |\Delta_{\mathbf{q}}|^2 \\
&\quad + \underbrace{\int_0^\beta d\tau \sum_{\mathbf{q}} \Delta_{\mathbf{q}}^* \sum_{\mathbf{k}} \psi_{\frac{\mathbf{q}}{2}-\mathbf{k}\downarrow} \psi_{\frac{\mathbf{q}}{2}+\mathbf{k}\uparrow}}_{\mathcal{A}} + \underbrace{\int_0^\beta d\tau \sum_{\mathbf{q}} \Delta_{\mathbf{q}} \sum_{\mathbf{k}} \psi_{\frac{\mathbf{q}}{2}+\mathbf{k}\uparrow}^* \psi_{\frac{\mathbf{q}}{2}-\mathbf{k}\downarrow}^*}_{\mathcal{B}} \\
&\quad \underbrace{\hspace{10em}}_{S_1}
\end{aligned} \tag{C.6}$$

So the partition function becomes

$$Z \propto \int \left\{ \prod_{\mathbf{p}} d\Delta_{\mathbf{p}} d\Delta_{\mathbf{p}}^* \right\} e^{-\frac{1}{V} \int_0^\beta d\tau \sum_{\mathbf{p}} |\Delta_{\mathbf{p}}|^2} \times \underbrace{\int \left\{ \prod_{\mathbf{k}\sigma} d\psi_{\mathbf{k}\sigma} d\psi_{\mathbf{k}\sigma}^* \right\} e^{S_0} e^{S_1}}_{\langle e^{S_1} \rangle} \tag{C.7}$$

where the expectation is evaluated with the “free fermion” Hamiltonian. Now

$$\langle e^{S_1} \rangle = 1 + \langle S_1 \rangle + \frac{1}{2} \langle S_1^2 \rangle + \frac{1}{6} \langle S_1^3 \rangle + \dots \tag{C.8}$$

and since we’re averaging with respect to S_0 only terms of the form $\langle \mathcal{A}\mathcal{B} \rangle$, $\langle \mathcal{A}^2\mathcal{B}^2 \rangle$, $\langle \mathcal{A}^3\mathcal{B}^3 \rangle$ etc. will be non-zero.

$$\langle e^{S_1} \rangle = 1 + \langle \mathcal{A}\mathcal{B} \rangle + \frac{1}{4} \langle \mathcal{A}^2\mathcal{B}^2 \rangle + \dots + \frac{1}{(n!)^2} \langle \mathcal{A}^n\mathcal{B}^n \rangle + \dots \tag{C.9}$$

If we're close to the tricritical point, Δ is small, and we can consider terms up to order Δ^2 , or in other words, only the term $\langle \mathcal{A}\mathcal{B} \rangle$.

$$\langle \mathcal{A}\mathcal{B} \rangle = \int_0^\beta d\tau \int_0^\beta d\tau' \sum_{\mathbf{q}} \Delta_{\mathbf{q}}^* \sum_{\mathbf{q}'} \Delta_{\mathbf{q}'} \sum_{\mathbf{k}\mathbf{k}'} \left\langle \Psi_{\frac{\mathbf{q}}{2}-\mathbf{k}\downarrow}(\tau) \Psi_{\frac{\mathbf{q}}{2}+\mathbf{k}\uparrow}(\tau) \Psi_{\frac{\mathbf{q}'}{2}+\mathbf{k}'\uparrow}^*(\tau') \Psi_{\frac{\mathbf{q}'}{2}-\mathbf{k}'\downarrow}^*(\tau') \right\rangle \quad (\text{C.10})$$

We can now use Wick's theorem to break up the expectation value into pairs, and the multiple sum above simplifies to

$$\langle \mathcal{A}\mathcal{B} \rangle = \beta \sum_{\mathbf{q}} |\Delta_{\mathbf{q}}|^2 \sum_{\mathbf{k}} \frac{1 - f(\epsilon_{\frac{\mathbf{q}}{2}+\mathbf{k}\uparrow}) - f(\epsilon_{\frac{\mathbf{q}}{2}-\mathbf{k}\downarrow})}{\epsilon_{\frac{\mathbf{q}}{2}+\mathbf{k}\uparrow} + \epsilon_{\frac{\mathbf{q}}{2}-\mathbf{k}\downarrow}} \quad (\text{C.11})$$

This sum by itself is divergent, but the first exponential in (C.7) subtracts off the divergent part. At unitarity

$$-\frac{|\Delta_{\mathbf{p}}|^2}{V} = -|\Delta_{\mathbf{p}}|^2 \sum_{\mathbf{k}} \frac{1}{2\epsilon_{\mathbf{k}}} \quad (\text{C.12})$$

So the combination

$$\chi(\mathbf{q}) = \sum_{\mathbf{k}} \left\{ \frac{1 - f(\epsilon_{\frac{\mathbf{q}}{2}+\mathbf{k}\uparrow}) - f(\epsilon_{\frac{\mathbf{q}}{2}-\mathbf{k}\downarrow})}{\epsilon_{\frac{\mathbf{q}}{2}+\mathbf{k}\uparrow} + \epsilon_{\frac{\mathbf{q}}{2}-\mathbf{k}\downarrow}} - \frac{1}{2\epsilon_{\mathbf{k}}} \right\} \quad (\text{C.13})$$

is convergent, and appears in the partition function as

$$\mathcal{Z} \propto \int \left\{ \prod_{\mathbf{p}} d\Delta_{\mathbf{p}} d\Delta_{\mathbf{p}}^* \right\} e^{\beta \sum_{\mathbf{q}} \chi(\mathbf{q}) |\Delta_{\mathbf{q}}|^2} \quad (\text{C.14})$$

$\chi(\mathbf{q})$ is given by the integral

$$\begin{aligned} \chi(\mathbf{q}) &= \frac{\text{Vol}}{2\pi^2} \left(\frac{2m}{\beta} \right)^{3/2} \frac{\beta}{2} \int_0^\infty dk \frac{k\mathcal{L}(k, q) - 2k^2 - \frac{1}{2}q^2 + 2\beta\mu}{k^2 - \beta\mu + \frac{1}{4}q^2} \\ \mathcal{L}(k, q) &= \frac{1}{q} \log \frac{e^{-kq} + e^{k^2+q^2/4} (e^{-\beta\mu\uparrow} + e^{-\beta\mu\downarrow}) + e^{2k^2+q^2/2+kq} e^{-2\beta\mu}}{e^{kq} + e^{k^2+q^2/4} (e^{-\beta\mu\uparrow} + e^{-\beta\mu\downarrow}) + e^{2k^2+q^2/2-kq} e^{-2\beta\mu}} \end{aligned} \quad (\text{C.15})$$

Effectively, we've written down the partition function in terms of a Bosonic field Δ .

APPENDIX D

COOLING AND TRAPPING OF ATOMS

The “granddaddy” of all cooling techniques in this field is laser cooling[31, 208], in which off-resonant (red-shifted) laser beams are used to slow down atoms by decreasing their average velocity, or putting them in “optical molasses” as is more fancifully known. Then the cooled gas is placed in a magneto-optical trap (MOT), where they are evaporatively cooled to nanoKelvin temperatures. In the eleven years since the first BEC, newer and better variations have been perfected over this archetypal technique, including some all-optical techniques, which obviate the need for bulky magnets. Below we outline the idea of laser cooling and evaporative cooling. It should be noted, however, that very often there is another cooling step between the two, such as Raman cooling or Sisyphus cooling, for which the reader is referred to the literature [209–213].

D.1 Laser cooling

Suppose an atom has a transition from the ground state to an excited state at an energy $\Delta = E_1 - E_0$. If a photon at frequency $\nu_0 = \Delta/h$ hits this atom (and if the photon is of the “right kind”, i.e., has the right polarization and so on – more about that later), then it can excite the atom from the ground state to the excited state. However, there will also be a momentum transfer, in that the momentum of the photon $h\nu_0/c$ will be transferred to the atom. So an atom at rest will receive a “kick” when it absorbs a photon, and will speed up. If, however, we can tune things so that only atoms in motion receive this “kick”, and further, they receive this “kick” only in a direction opposite their current velocity, then they will slow down after repeated kicks. The way to ensure this velocity selectivity is by ensuring that the photon has an energy *less* than Δ . The absorption spectrum of an

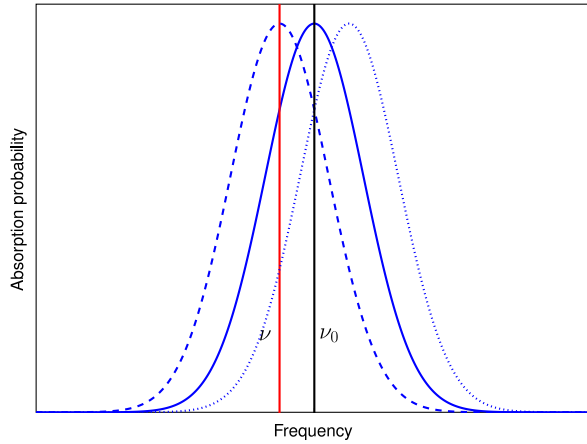


FIGURE D.1: Schematic representation (color on-line) of red-detuned laser and Doppler-shifted absorption spectrum. The solid curve corresponds to the absorption spectrum of an atom at rest, the dashed blue curve is for an atom moving *towards* the laser source, while the dotted blue curve is for an atom moving *away* from the laser source.

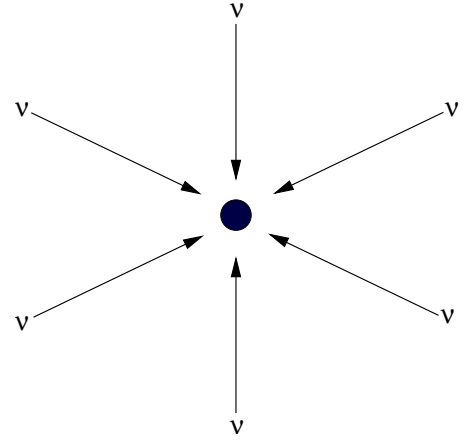


FIGURE D.2: Laser cooling by six lasers along the three axes. The solid arrows are lasers, all identically red detuned, and the blob in the center is the gas being cooled.

atom, even at zero temperature, has a finite width limited by the lifetime of the excited state. In figure (D.1), the absorption spectrum is represented by a solid blue curve with a peak at ν_0 , the resonant frequency. Let an external laser be tuned to some frequency $\nu < \nu_0$ (the vertical red line). Now if the atom is moving *towards* the laser source with a velocity v , then according to the atom the frequency of the laser is *blue shifted* to

$$\nu' = \nu \sqrt{\frac{1 + (v/c)}{1 - (v/c)}} \approx \nu \left(1 + \frac{v}{c}\right) \quad (\text{D.1})$$

Or, equivalently, from the point of view of the laser, the absorption spectrum of the atom is *red shifted* so that the absorption peak is now at $\nu'_0 = \nu_0(1 - v/c)$. If, however, the velocity is “just right” so that the red-shifted peak is exactly on top of ν (the dashed blue curve in figure (D.1)), i.e.,

$$v = \frac{c}{\nu_0} (\nu_0 - \nu) \quad (\text{D.2})$$

then the atom will absorb photons from the laser with a high probability. Conserving both energy and momentum in such an (inelastic) process where a photon is completely absorbed by an atom to go into the excited state E_1 , we see that the new velocity of the atom is

$$v' = v - \frac{\Delta}{mc} \quad (\text{D.3})$$

where m is the mass of the atom.¹ Atoms that are moving away from the laser, however (dotted curve in figure (D.1)), will be blue-shifted w.r.t. the laser, and hence will not absorb photons and will not receive any kicks. So we have found a way of slowing down only atoms moving with a certain velocity. If we now use identically red-shifted lasers (which can be achieved by splitting a single laser) from all six directions in xyz space (figure (D.2)), then we will slow down all atoms that have a velocity component v in any of the three directions.

When the atom re-emits and comes down to the ground state, it will emit in a random direction, so the *average* kick received from multiple re-emissions is going to be zero. This arrangement is going to slow down all atoms with a specific velocity component v , which depends upon the degree of detuning as mentioned above. So now we gradually sweep the laser frequency closer to ν_0 to target lower and lower velocities. This brings down the average velocity of all the atoms, effectively cooling them.

D.1.1 Magneto-optic trapping

Cooling is not trapping. Although the above procedure will slow atoms down, there is nothing to prevent them from slowly drifting out of the focal point of the six lasers. This is prevented by a magneto-optical trap (MOT). It turns out, to trap atoms in a MOT, we

¹The atoms are assumed to be slow so that the momentum is non-relativistic ($\mathbf{p} = m\mathbf{v}$).

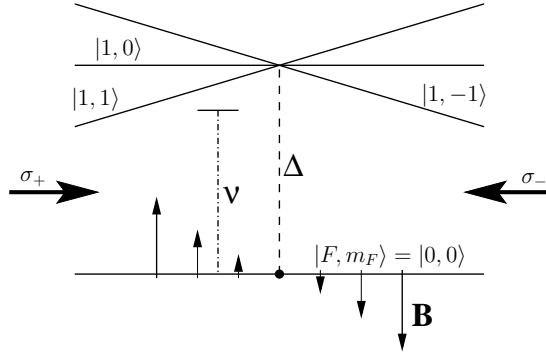


FIGURE D.3: Schematic of a MOT in 1-D.

need an atom with not one but *three* excited states, which are degenerate in the absence of an external magnetic field. Suppose the total angular momentum of an atom is $F = 0$ in the ground state and $F = 1$ in the first excited state. We place the gas in an anti-Helmholtz magnetic field geometry², such that the field is lowest at the center of the trap and highest at the edges, having opposite signs at the opposite edges, as in figure (D.3). This ensures that the $|1, 1\rangle$ state has the highest energy on one side, while the $|1, -1\rangle$ state has the highest energy on the other side. The states $|1, 0\rangle$ and $|0, 0\rangle$ do not experience any Zeeman shift. Now we shine two red-detuned lasers of the same frequency (ν in figure (D.3)) but opposite circular polarizations (σ_+ and σ_-) from the two sides, such that σ_+ shines from the end where $|1, 1\rangle$ has the lower energy. The key point is that σ_+ only couples $|0, 0\rangle$ with $|1, 1\rangle$, while σ_- only couples $|0, 0\rangle$ with $|1, -1\rangle$. At the center of the trap, ν is slightly lower than Δ and consequently there is the usual laser cooling as detailed above. Now if an atom strays to the right in figure (D.3), then its $|0, 0\rangle \rightarrow |1, -1\rangle$ absorption gets closer to ν and its $|0, 0\rangle \rightarrow |1, 1\rangle$ transition moves away from ν . In terms of photon absorption, it “sees” the σ_- beam better than the σ_+ beam, absorbs more photons from the right³ and experiences a net force to the left. It is also obvious that this net force increases as the atom moves further rightward⁴. An analogous effect takes place at the left

²This is done by simply reversing the current in one of the two Helmholtz coils

³In short, the role of the atom velocity used in laser cooling above is played by the magnetic field.

⁴Close to the center, this restoring force is harmonic, not surprisingly.

extremity, pushing all left-straying atoms to the right. So this setup not only cools the atoms down, it also traps them by creating a net restoring force towards the center. This basic setup is replicated along all three axes to create a 3D trap to contain cooled gases.

D.1.2 Temperature limits

The lowest temperature(s) possible with the method outlined above comes from two facts.

- This technique obviously depends on the fact that static atoms do not absorb the photons, while atoms moving with a certain velocity do. This will no longer be the case if the Doppler shift is as small as the absorption line-width; at (and below) that detuning, the absorption spectrum ceases to be velocity dependent. This lower limit on the detuning sets a limit on the lowest velocities we can target. If the absorption line-width is $h\gamma$, then *Doppler limit* of temperature is

$$k_B T_{\text{Doppler}} = \frac{1}{2} h\gamma \quad (\text{D.4})$$

This is of the order of 100 microKelvins. The first few laser cooling experiments seemed to agree with this estimate of the lower bound on temperature[30, 214]. Interestingly, subsequent laser cooling experiments turned out to produce much lower (sub-Doppler) temperatures quite by happy chance[215, 216]. This surprising result was explained later as a result of a Sisyphus-like cooling process in the standing-wave field of two counterpropagating lasers[217]. This lowered the temperature by a factor of five to ten from Eq (D.4), until it hit the next limit (below).

- Although the re-emission kick is in a random direction, ensuring that the time-averaged momentum kick due to re-emission is zero, the time-averaged kinetic energy of the atom due to re-emission kicks is non-zero. This sets a limit on the

lowest temperature achievable by

$$k_B T_R = \frac{\Delta^2}{2mc^2} \quad (\text{D.5})$$

This is of the order of 10 microKelvins, and is called the *single photon recoil limit*. This is still too high to produce BCS-s, and this limit was broken by techniques such as Raman cooling[218, 219] which produced temperatures lower by a factor of ten to hundred.

As we have noted, the simple laser cooling and magneto-optical trapping summarized above is not enough to produce nanoKelvin temperatures. This is usually followed by one or more stages [217–219], until, to produce a BEC, the atoms need to be evaporatively cooled.

D.2 Evaporative cooling

Using a combination of optical techniques, the temperature can be brought down to several μK , sometimes even several nK[211]. However, what matters in creating BEC-s is not the temperature alone, but the phase space density⁵. Although [211] obtained a temperature of ~ 2.8 nK, they only got $n\lambda_{dB}^3 \sim 10^{-7}$. Even a more improved technique[220] which achieved a much higher phase space density with Raman-cooled Cesium only managed $n\lambda_{dB}^3 \sim 1/500$. To get a BEC, atoms are cooled in much the same way as a cup of coffee.

In a cup of coffee, the most energetic molecules with a lot of kinetic energy escape from the surface into the gaseous form. Since their kinetic energy is more than the mean kinetic energy, their escape brings the average kinetic energy *down*, which brings down

⁵The condition for forming a BEC is $n\lambda_{dB}^3 = 2.612$, where n is the density, and λ_{dB} is the thermal de Broglie wavelength, given by $\lambda_{dB} = \hbar/\sqrt{2mk_B T}$. So we need low temperatures *and* high densities to form a BEC[67].

the temperature (our coffee obviously gets cold!). In cold gases, much the same principle applies. During optical cooling, the atoms are trapped inside a magneto-optic trap. Now since we need to go far below the recoil limit, a MOT is not the best trap any more. So the pre-cooled atoms are trapped inside some kind of conservative trap, for example a purely static magnetic field or a far-off-resonant optical field[221]. Higher-energy atoms are expelled by mainly four different evaporation techniques[222].

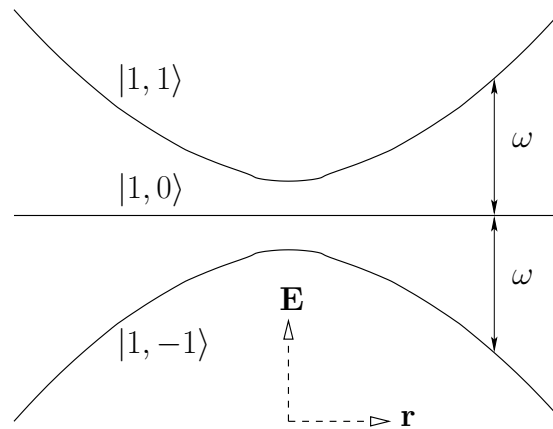


FIGURE D.4: Energy levels of $|F, m_F\rangle$ states in a quadratic magnetic trap; \mathbf{r} is the distance from the trap center and \mathbf{E} is the energy.

1. **Direct contact with walls:** Some experimentalists keep a sticky wall close to the sample, and then lower the temperature of the wall gradually. The wall absorbs the high energy tail of the distribution.
2. **Lowering the trapping potential:** The total trapping potential can be suddenly lowered, so that bound states of the deeper potential now become continuum states of the shallower potential. The problem with this is that the elastic collisions rates are small throughout the ramping and cannot be increased, so the cooling is very slow.
3. **Lowering trapping potential along one axis:** In this method, in a 3D trap, only the axial trapping potential is lowered, so this is basically a 1D selection method. The advantage is that the trapping volume and hence the collision rate can still be

controlled through the radial potential, so this cooling can be a lot faster than the previous one.

4. **RF-induced evaporation:** This is currently the most popular and effective method. Let an atom with $F = 1$ be trapped as shown in figure (D.4); the magnetic field is a minimum at the center, and $|1, 1\rangle$ is a low-field-seeking state which is trapped. The atoms with higher kinetic energy will reside closer to the edges, and hence our goal is to eliminate the atoms close to the edges. We apply an RF field at frequency ω , which is resonant with the $|1, -1\rangle \leftrightarrow |1, 0\rangle$ and $|1, 0\rangle \leftrightarrow |1, 1\rangle$ transitions near the edge. Then only the atoms in $|1, 1\rangle$ near the edge will undergo stimulated emission to end up first in $|1, 0\rangle$ and finally in $|1, -1\rangle$. Now $|1, -1\rangle$ is a high-field-seeking state, and so will “roll down” the potential and exit the trap. This will eliminate the higher energy atoms and bring the temperature down. Sometimes instead of an RF field, a laser is tuned to some optical transition and selectively applied to the edges of the cloud, to eliminate atoms by optical pumping.

This last stage of evaporative cooling can give six orders of magnitude increment in $n\lambda_{dB}^3$, resulting in Bose-Einstein condensation. To summarize, Doppler cooling produces a temperature of $\sim 100 \mu\text{K}$; intermediate techniques bring it down to $\sim 10 \mu\text{K}$ (or sometimes even $\sim \text{nK}$ [211]); and evaporative cooling, with possible temperatures as low as 500 pK[223], brings the phase space density up to form BEC-s.

The techniques of Doppler and evaporative cooling, while general, do not necessarily always work. For example, the energy level structure of the target molecule might be too complicated for Doppler cooling, in which case techniques such as [224, 225] need to be used. More importantly, evaporative cooling will not work for atoms with unfavorable collisional properties. A direct evaporative cooling relies on the rapid thermalization of a cloud, which, at low temperatures, depends on the s -wave scattering between the

atoms. For degenerate Fermions, the s -wave scattering length is zero between identical species due to Pauli exclusion principle, and the p -wave scattering goes to zero at low temperatures. So they can not thermalize, and cannot be cooled by direct evaporative cooling. This can be a problem even for certain Bosonic species; e.g., the s -wave scattering length of ^{85}Rb vanishes for scattering energies of $E \simeq 375 \mu\text{K}$ [226].

In such unfavorable cases, the target is *sympathetically* cooled. The idea behind cooling a difficult-to-cool species is to find a second species that has good collisional properties with the first species, i.e., which has a much higher rate of elastic collisions than inelastic collisions. Then we cool the second species down, and let the first species thermalize with the second species, thereby bringing down the temperature [36, 68, 69, 73, 226]. The importance of this technique cannot be overemphasized, since every single experiment with degenerate fermi gases utilizes sympathetic cooling.

APPENDIX E

PARTIAL DERIVATIVES AT CONSTANT PRESSURE

E.1 A general “chain rule”

Suppose we have two functions $f(x, y)$ and $z(x, y)$, and we want to evaluate $\partial f/\partial x|_z$ instead of $\partial f/\partial x|_y$. In general,

$$\delta f = \left. \frac{\partial f}{\partial x} \right|_y \delta x + \left. \frac{\partial f}{\partial y} \right|_x \delta y$$

If we add the constraint $z(x, y) = \text{constant}$, then

$$\begin{aligned} \delta z &= \left. \frac{\partial z}{\partial x} \right|_y \delta x + \left. \frac{\partial z}{\partial y} \right|_x \delta y = 0 \\ \Rightarrow \delta y &= -\delta x \left. \frac{\partial z}{\partial x} \right|_y \left. \frac{\partial y}{\partial z} \right|_x \end{aligned}$$

Using this δy in the expression for δf ,

$$\begin{aligned} \left. \frac{\partial f}{\partial x} \right|_z &= \left. \frac{\partial f}{\partial x} \right|_y - \left. \frac{\partial f}{\partial y} \right|_x \left. \frac{\partial z}{\partial x} \right|_y \left. \frac{\partial y}{\partial z} \right|_x \\ &= \left. \frac{\partial f}{\partial x} \right|_y + \left. \frac{\partial f}{\partial y} \right|_x \left. \frac{\partial y}{\partial x} \right|_z \end{aligned} \tag{E.1}$$

E.2 Latent heat

We need to evaluate $\partial S/\partial N_f|_{P,T,N_b}$.

$$\begin{aligned} \left. \frac{\partial S}{\partial N_f} \right|_{P,T,N_b} &= \left. \frac{\partial S}{\partial N_f} \right|_{V,T,N_b} + \left. \frac{\partial S}{\partial V} \right|_{T,N_f,N_b} \left. \frac{\partial V}{\partial N_f} \right|_{P,T,N_b} \\ &= \left. \frac{\partial s}{\partial n_f} \right|_{V,T,N_b} + \left. \frac{\partial P}{\partial T} \right|_{V,N_f,N_b} \left. \frac{\partial V}{\partial N_f} \right|_{P,T,N_b} \end{aligned} \tag{E.2}$$

where $s = S/V$, and we've related $\partial S/\partial V$ to $\partial P/\partial T$ using a Maxwell's relation. Since it's easier for us to express the densities in terms of the chemical potentials (rather than the

other way round), we can write

$$s = s(T, \mu_f, \mu_b, n_f(T, \mu_f, \mu_b), n_b(T, \mu_f, \mu_b))$$

Noting that constant V and N_b implies constant n_b , we have

$$\begin{aligned} \delta n_b|_T &= \left. \frac{\partial n_b}{\partial \mu_f} \right|_{\mu_b, T} \delta \mu_f + \left. \frac{\partial n_b}{\partial \mu_b} \right|_{\mu_f, T} \delta \mu_b = 0 \\ \Rightarrow \delta \mu_b &= -\delta \mu_f \frac{\left. \frac{\partial n_b}{\partial \mu_f} \right|_{T, \mu_b}}{\left. \frac{\partial n_b}{\partial \mu_b} \right|_{\mu_f, T}} \\ \Rightarrow \delta s|_{T, n_b} &= \left. \frac{\partial s}{\partial n_f} \right|_{n_b, T, \mu_f, \mu_b} \delta n_f + \delta \mu_f \left[\left. \frac{\partial s}{\partial \mu_f} \right|_{\mu_b, T, n_f, n_b} - \left. \frac{\partial s}{\partial \mu_b} \right|_{\mu_f, T, n_f, n_b} \frac{\left. \frac{\partial n_b}{\partial \mu_f} \right|_{T, \mu_b}}{\left. \frac{\partial n_b}{\partial \mu_b} \right|_{\mu_f, T}} \right] \end{aligned} \quad (\text{E.3})$$

but at constant T , we can write δn_f as

$$\begin{aligned} \delta n_f|_T &= \left. \frac{\partial n_f}{\partial \mu_f} \right|_{\mu_b} \delta \mu_f + \left. \frac{\partial n_f}{\partial \mu_b} \right|_{\mu_f} \delta \mu_b \\ &= \delta \mu_f \left[\left. \frac{\partial n_f}{\partial \mu_f} \right|_{\mu_b, T} - \left. \frac{\partial n_f}{\partial \mu_b} \right|_{\mu_f, T} \frac{\left. \frac{\partial n_b}{\partial \mu_f} \right|_{T, \mu_b}}{\left. \frac{\partial n_b}{\partial \mu_b} \right|_{\mu_f, T}} \right] \\ \Rightarrow \delta \mu_f|_{T, n_b} &= \frac{\delta n_f}{\left. \frac{\partial n_f}{\partial \mu_f} \right|_{\mu_b, T} - \left. \frac{\partial n_f}{\partial \mu_b} \right|_{\mu_f, T} \frac{\left. \frac{\partial n_b}{\partial \mu_f} \right|_{T, \mu_b}}{\left. \frac{\partial n_b}{\partial \mu_b} \right|_{\mu_f, T}}} \end{aligned} \quad (\text{E.4})$$

Substituting $\delta \mu_f$ from equation (E.4) into (E.3),

$$\left. \frac{\partial s}{\partial n_f} \right|_{T, n_b} = \left. \frac{\partial s}{\partial n_f} \right|_{T, n_b, \mu_f, \mu_b} + \frac{\left. \frac{\partial s}{\partial \mu_f} \right|_{\mu_b, T, n_f, n_b} \left. \frac{\partial n_b}{\partial \mu_b} \right|_{\mu_f, T} - \left. \frac{\partial s}{\partial \mu_b} \right|_{\mu_f, T, n_f, n_b} \left. \frac{\partial n_b}{\partial \mu_f} \right|_{T, \mu_b}}{\left. \frac{\partial n_f}{\partial \mu_f} \right|_{T, \mu_b} \left. \frac{\partial n_b}{\partial \mu_b} \right|_{T, \mu_f} - \left. \frac{\partial n_f}{\partial \mu_b} \right|_{T, \mu_f} \left. \frac{\partial n_b}{\partial \mu_f} \right|_{T, \mu_b}} \quad (\text{E.5})$$

The entropy per unit volume s is just $(\mathcal{E} - \mathcal{A})/T$, where \mathcal{E} is the expectation of the Hamiltonian (5.2),

$$\begin{aligned}\frac{\mathcal{E}_{\text{SF}}}{ma^5} &= 2\pi\lambda_b y^2 + 3\pi\lambda_f x y - 2v_b y + \frac{1}{4\pi^2} \left(\frac{2}{\beta}\right)^{3/2} \left[\frac{1}{\beta} F_{3/2}(\beta\tilde{v}_f) - \tilde{v}_f F_{1/2}(\beta\tilde{v}_f) \right] \\ &\quad + \frac{1}{4\pi\lambda_b} (v_b - 3\pi\lambda_f x)^2 + \frac{1}{4\pi^2} \left(\frac{4}{\beta}\right)^{3/2} \left[\frac{1}{\beta} G_{3/2}(\beta\tilde{v}_b) - \tilde{v}_b G_{1/2}(\beta\tilde{v}_b) \right] \\ \frac{\mathcal{E}_{\text{N}}}{ma^5} &= -2\pi\lambda_b y^2 - 3\pi\lambda_f x y + \frac{1}{4\pi^2} \left(\frac{2}{\beta}\right)^{3/2} \left[\frac{1}{\beta} F_{3/2}(\beta\tilde{v}_f) - \tilde{v}_f F_{1/2}(\beta\tilde{v}_f) \right] \\ &\quad + \frac{1}{4\pi^2} \left(\frac{4}{\beta}\right)^{3/2} \left[\frac{1}{\beta} G_{3/2}(\beta\tilde{v}_b) - \tilde{v}_b G_{1/2}(\beta\tilde{v}_b) \right]\end{aligned}\tag{E.6}$$

On the other hand, in terms of dimensionless variables, \mathcal{A} is

$$\begin{aligned}\frac{\mathcal{A}_{\text{SF}}}{ma^5} &= \frac{1}{4\pi\lambda_b} (v_b - 3\pi\lambda_f x y)^2 + 2\pi\lambda_b y^2 - 2v_b y + 3\pi\lambda_f x y \\ &\quad - \frac{1}{6\pi^2\beta} \left[\left(\frac{4}{\beta}\right)^{3/2} G_{3/2}(\beta\tilde{v}_b) + \left(\frac{2}{\beta}\right)^{3/2} F_{3/2}(\beta\tilde{v}_f) \right] \\ \frac{\mathcal{A}_{\text{N}}}{ma^5} &= -2\pi\lambda_b y^2 - 3\pi\lambda_f x y - \frac{1}{6\pi^2\beta} \left[\left(\frac{4}{\beta}\right)^{3/2} G_{3/2}(\beta\tilde{v}_b) + \left(\frac{2}{\beta}\right)^{3/2} F_{3/2}(\beta\tilde{v}_f) \right]\end{aligned}\tag{E.7}$$

Then $\partial s/\partial n_f$ becomes

$$\begin{aligned}\left. \frac{\partial s}{\partial n_f} \right|_{T, n_b} &= \beta k_B \frac{\partial(\mathcal{E} - \mathcal{A})}{\partial x} + \beta k_B \frac{\frac{\partial(\mathcal{E} - \mathcal{A})}{\partial v_f} \frac{\partial y}{\partial v_b} - \frac{\partial(\mathcal{E} - \mathcal{A})}{\partial v_b} \frac{\partial y}{\partial v_f}}{\frac{\partial[x, y]}{\partial[v_f, v_b]}} \\ &= k_B \Phi\end{aligned}\tag{E.8}$$

where Φ is a function of x , y , v_f , v_b and β . Everything that is not explicitly varying above has been kept fixed, so the derivatives, though tedious, are straightforward. \mathcal{E} and \mathcal{A} used above are actually their dimensionless forms, i.e., divided by ma^5 . The denominator above is the determinant of a Jacobian matrix,

$$\frac{\partial[x, y]}{\partial[v_f, v_b]} = \left. \frac{\partial x}{\partial v_f} \right|_{T, v_b} \left. \frac{\partial y}{\partial v_b} \right|_{T, v_f} - \left. \frac{\partial x}{\partial v_b} \right|_{T, v_f} \left. \frac{\partial y}{\partial v_f} \right|_{T, v_b}$$

Next, we need to calculate $\partial P/\partial T|_{n_f, n_b}$. Again, the pressure is a function of

$$P = P(T, \mu_f, \mu_b, n_f(T, \mu_f, \mu_b), n_b(T, \mu_f, \mu_b))$$

and n_b and n_f being constant give

$$\begin{aligned}\delta n_f &= \left. \frac{\partial n_f}{\partial T} \right|_{\mu_f, \mu_b} \delta T + \left. \frac{\partial n_f}{\partial \mu_f} \right|_{\mu_b, T} \delta \mu_f + \left. \frac{\partial n_f}{\partial \mu_b} \right|_{\mu_f, T} \delta \mu_b = 0 \\ \delta n_b &= \left. \frac{\partial n_b}{\partial T} \right|_{\mu_f, \mu_b} \delta T + \left. \frac{\partial n_b}{\partial \mu_f} \right|_{\mu_b, T} \delta \mu_f + \left. \frac{\partial n_b}{\partial \mu_b} \right|_{\mu_f, T} \delta \mu_b = 0\end{aligned}\tag{E.9}$$

and we can solve the above system for $\delta \mu_f$ and $\delta \mu_b$,

$$\begin{aligned}\delta \mu_f &= \delta T \frac{\left. \frac{\partial n_f}{\partial \mu_b} \right|_{\mu_f, T} \left. \frac{\partial n_b}{\partial T} \right|_{\mu_f, \mu_b} - \left. \frac{\partial n_b}{\partial \mu_b} \right|_{\mu_f, T} \left. \frac{\partial n_f}{\partial T} \right|_{\mu_f, \mu_b}}{\left. \frac{\partial [n_f, n_b]}{\partial [\mu_f, \mu_b]} \right|_{\mu_f, \mu_b}} \\ \delta \mu_b &= \delta T \frac{\left. \frac{\partial n_b}{\partial \mu_f} \right|_{\mu_b, T} \left. \frac{\partial n_f}{\partial T} \right|_{\mu_f, \mu_b} - \left. \frac{\partial n_f}{\partial \mu_f} \right|_{\mu_b, T} \left. \frac{\partial n_b}{\partial T} \right|_{\mu_f, \mu_b}}{\left. \frac{\partial [n_f, n_b]}{\partial [\mu_f, \mu_b]} \right|_{\mu_f, \mu_b}}\end{aligned}\tag{E.10}$$

Substituting these into δP give us what we want:

$$\begin{aligned}\delta P|_{n_f, n_b} &= \left. \frac{\partial P}{\partial T} \right|_{n_f, n_b, \mu_f, \mu_b} \delta T + \left. \frac{\partial P}{\partial \mu_f} \right|_{n_f, n_b, \mu_b, T} \delta \mu_f + \left. \frac{\partial P}{\partial \mu_b} \right|_{n_f, n_b, \mu_f, T} \delta \mu_b \\ \Rightarrow \left. \frac{\partial P}{\partial T} \right|_{n_f, n_b} &= \left. \frac{\partial P}{\partial T} \right|_{n_f, n_b, \mu_f, \mu_b} + \frac{1}{\left. \frac{\partial [n_f, n_b]}{\partial [\mu_f, \mu_b]} \right|_{\mu_f, \mu_b}} \left\{ \left. \frac{\partial P}{\partial \mu_f} \right|_{T, n_b, n_f, \mu_b} \left[\left. \frac{\partial n_f}{\partial \mu_b} \right|_{\mu_f, T} \left. \frac{\partial n_b}{\partial T} \right|_{\mu_f, \mu_b} - \left. \frac{\partial n_b}{\partial \mu_b} \right|_{\mu_f, T} \left. \frac{\partial n_f}{\partial T} \right|_{\mu_f, \mu_b} \right] \right. \\ &\quad \left. + \left. \frac{\partial P}{\partial \mu_b} \right|_{T, n_f, n_b, \mu_f} \left[\left. \frac{\partial n_b}{\partial \mu_f} \right|_{\mu_b, T} \left. \frac{\partial n_f}{\partial T} \right|_{\mu_f, \mu_b} - \left. \frac{\partial n_f}{\partial \mu_f} \right|_{\mu_b, T} \left. \frac{\partial n_b}{\partial T} \right|_{\mu_f, \mu_b} \right] \right\} \\ &= \frac{k_B \beta^2}{a^2} \frac{\partial \mathcal{A}}{\partial \beta} + \frac{(k_B/a^3) \beta^2}{\left. \frac{\partial [x, y]}{\partial [v_f, v_b]} \right|_{\mu_f, \mu_b}} \left\{ x \left[\frac{\partial y}{\partial v_b} \frac{\partial x}{\partial \beta} - \frac{\partial x}{\partial v_b} \frac{\partial y}{\partial \beta} \right] + y \left[\frac{\partial x}{\partial v_f} \frac{\partial y}{\partial \beta} - \frac{\partial y}{\partial v_f} \frac{\partial x}{\partial \beta} \right] \right\} \\ &= \frac{k_B}{a^3} \Gamma\end{aligned}\tag{E.11}$$

where we've used $P = -\mathcal{A}$. Finally, we note that $\left. \partial V / \partial N_f \right|_{P, T, N_b}$ is just $1/n_f = a^3/x$, and

hence

$$T \left. \frac{\partial S}{\partial N_f} \right|_{P, T, N_b} = \frac{1}{m a^2} \frac{1}{\beta} \left[\Phi + \frac{\Gamma}{x} \right]\tag{E.12}$$

which has the correct dimension of energy (our β is dimensionless).

E.3 Specific heat

We need to evaluate $\partial S/\partial T|_{P,N_f,N_b}$, which is

$$\begin{aligned}\frac{\partial S}{\partial T}\Big|_{P,N_f,N_b} &= \frac{\partial S}{\partial T}\Big|_{V,N_f,N_b} + \frac{\partial S}{\partial V}\Big|_{T,N_f,N_b} \frac{\partial V}{\partial T}\Big|_{P,N_f,N_b} \\ &= V \frac{\partial s}{\partial T}\Big|_{n_f,n_b} - \frac{\partial P}{\partial T}\Big|_{n_f,n_b}^2 \Big/ \frac{\partial P}{\partial V}\Big|_{T,N_f,N_b}\end{aligned}\quad (\text{E.13})$$

where we've used a Maxwell's relation to relate $\partial S/\partial V$ to $\partial P/\partial T$, and used

$$\frac{\partial V}{\partial T}\Big|_P \frac{\partial T}{\partial P}\Big|_V \frac{\partial P}{\partial V}\Big|_T = -1$$

The calculation of $\partial s/\partial T$ is identical to the calculation of $\partial P/\partial T$ detailed in appendix E.2 above, with P substituted by s . In terms of dimensionless variables, it reads

$$\begin{aligned}\frac{\partial s}{\partial T}\Big|_{n_f,n_b} &= -\frac{k_B^2 m \beta^2}{a} \frac{\partial \beta(\mathcal{E} - \mathcal{A})}{\partial \beta} + \frac{k_B^2 \beta^3 m/a}{\frac{\partial[x,y]}{\partial[v_f,v_b]}} \left\{ \begin{aligned} &\left[\frac{\partial y}{\partial v_b} \frac{\partial x}{\partial \beta} - \frac{\partial x}{\partial v_b} \frac{\partial y}{\partial \beta} \right] \frac{\partial(\mathcal{E} - \mathcal{A})}{\partial v_f} \\ &+ \left[\frac{\partial x}{\partial v_f} \frac{\partial y}{\partial \beta} - \frac{\partial y}{\partial v_f} \frac{\partial x}{\partial \beta} \right] \frac{\partial(\mathcal{E} - \mathcal{A})}{\partial v_b} \end{aligned} \right\} \\ &= k_B^2 \frac{m}{a} \Theta\end{aligned}\quad (\text{E.14})$$

We've already calculated $\partial P/\partial T|_{n_f,n_b}$ in appendix E.2 above, so all that's left is to calculate $\partial P/\partial V$.

$$\delta P|_T = \frac{\partial P}{\partial \mu_f}\Big|_{\mu_b,n_f,n_b} \delta \mu_f + \frac{\partial P}{\partial \mu_b}\Big|_{\mu_f,n_f,n_b} \delta \mu_b + \frac{\partial P}{\partial n_f}\Big|_{\mu_f,\mu_b,n_b} \delta n_f + \frac{\partial P}{\partial n_b}\Big|_{\mu_f,\mu_b,n_f} \delta n_b \quad (\text{E.15})$$

The last two terms are zero, since $P = -\mathcal{A}$, and in equilibrium $\partial \mathcal{A}/\partial n_{f,b} = 0$. Further, since N_f and N_b are constant, $\delta n_{f,b} = -n_{f,b}(\delta V/V)$, which means

$$\begin{aligned}\delta n_f|_T &= \frac{\partial n_f}{\partial \mu_f}\Big|_{\mu_b,T} \delta \mu_f + \frac{\partial n_f}{\partial \mu_b}\Big|_{\mu_f,T} \delta \mu_b = -n_f \frac{\delta V}{V} \\ \delta n_b|_T &= \frac{\partial n_b}{\partial \mu_f}\Big|_{\mu_b,T} \delta \mu_f + \frac{\partial n_b}{\partial \mu_b}\Big|_{\mu_f,T} \delta \mu_b = -n_b \frac{\delta V}{V}\end{aligned}\quad (\text{E.16})$$

We can solve these equations to get $\delta\mu_{f,b}$ in terms of δV ,

$$\begin{aligned}\delta\mu_f &= \frac{\delta V/V}{\frac{\partial[n_f, n_b]}{\partial[\mu_f, \mu_b]}} \left[n_b \frac{\partial n_f}{\partial \mu_b} \Big|_{\mu_f, T} - n_f \frac{\partial n_b}{\partial \mu_b} \Big|_{\mu_f, T} \right] \\ \delta\mu_b &= \frac{\delta V/V}{\frac{\partial[n_f, n_b]}{\partial[\mu_f, \mu_b]}} \left[n_f \frac{\partial n_b}{\partial \mu_f} \Big|_{\mu_b, T} - n_b \frac{\partial n_f}{\partial \mu_f} \Big|_{\mu_b, T} \right]\end{aligned}\tag{E.17}$$

Substituting these solutions into (E.15), we get

$$\begin{aligned}V \frac{\partial P}{\partial V} \Big|_{T, N_f, N_b} &= \frac{n_f}{\frac{\partial[n_f, n_b]}{\partial[\mu_f, \mu_b]}} \left[n_b \frac{\partial n_f}{\partial \mu_b} \Big|_{\mu_f, T} - n_f \frac{\partial n_b}{\partial \mu_b} \Big|_{\mu_f, T} \right] + \frac{n_b}{\frac{\partial[n_f, n_b]}{\partial[\mu_f, \mu_b]}} \left[n_f \frac{\partial n_b}{\partial \mu_f} \Big|_{\mu_b, T} - n_b \frac{\partial n_f}{\partial \mu_f} \Big|_{\mu_b, T} \right] \\ &= \frac{1}{ma^5 \frac{\partial[x, y]}{\partial[v_f, v_b]}} \left\{ x \left[y \frac{\partial x}{\partial v_b} - x \frac{\partial y}{\partial v_b} \right] + y \left[x \frac{\partial y}{\partial v_f} - y \frac{\partial x}{\partial v_f} \right] \right\} \\ &= \frac{\kappa}{ma^5}\end{aligned}\tag{E.18}$$

Finally, using (E.11), (E.14) and (E.18) in (E.13), we get

$$C_P = T \frac{\partial S}{\partial T} \Big|_{P, N_f, N_b} = \frac{k_B V}{\beta a^3} \left[\Theta - \frac{\Gamma^2}{\kappa} \right]\tag{E.19}$$

which has the dimension of k_B as it should (recall that β is dimensionless).

APPENDIX F

“STEADY-STATE” PUMPING RATE FROM A TRAP CENTER

We need to calculate the relaxation rate of a fermi cloud in a harmonic trap if the center is suddenly depleted. For our estimate we'll assume that the equilibrium density profile of a polarized Fermi gas in a harmonic trap is gaussian. This is a slight approximation; for example the 3D density in a cigar-shaped trap is $n(\mathbf{r}) = (2mk_B T)^{3/2} F_{1/2}(\mu(\mathbf{r})/k_B T) / 4\pi^2$ where $F_{1/2}$ was defined in (5.4). $\mu(\mathbf{r})$ is the local chemical potential $\mu(0) - m\omega_z^2 z^2/2 - m\omega_r^2 r^2/2$. At high T, $n(\mathbf{r}) = (2m/\pi\beta)^{3/2} (e^{\beta\mu(0)}/8) e^{-\beta m(\omega_z^2 z^2 + \omega_r^2 r^2)/2}$ is a gaussian in trap coordinates z and r , whereas even at low T, a gaussian is not a bad approximation for $n(\mathbf{r}) = (2m\mu(\mathbf{r}))^{3/2}/6\pi^2$. The 1-D axial density profile in a cigar-shaped trap is

$$n(z) = n_0 e^{-\beta m \omega_z^2 z^2 / 2}$$

where $n_0 = 2\pi n_c / \beta m \omega_r^2$, n_c being the 3-D central density. Now suppose at $t = 0$ an identical laser, focussed crosswise, is used to “bleach” the trap center of particles, so that the density profile $n(z, t = 0)$ looks like figure F.1.

$$n(z, t = 0) = n_0 \left(e^{-\beta m \omega_z^2 z^2 / 2} - e^{-\beta m \omega_r^2 z^2 / 2} \right)$$

We need to figure out how the profile in figure F.1 relaxes to its equilibrium.

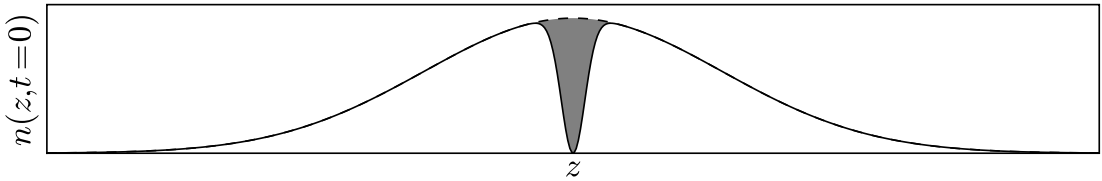


FIGURE F.1: Axial density profile (solid line) after depletion at $t = 0$. The dashed line represents density profile before depletion, while the area of the shaded region is the particle number depleted, which comes out to a fraction ω_z/ω_r of the total number.

Diffusive transport in a harmonic trap is governed by a Smoluchowski equation, which evolves a probability function $p(\mathbf{r}, t; \mathbf{r}', 0)$. This probability function can be thought of

as the probability of finding a particle at position \mathbf{r} and time t given its initial position \mathbf{r}' at $t = 0$. In the presence of an external force $\mathbf{F}(\mathbf{r})$, the Smoluchowski equation with a homogenous and isotropic diffusion constant D is [227]

$$\partial_t p(\mathbf{r}, t; \mathbf{r}', 0) = D \nabla \cdot (\nabla - \beta \mathbf{F}) p(\mathbf{r}, t; \mathbf{r}', 0) \quad (\text{F.1})$$

where $\beta = 1/k_B T$. If the force \mathbf{F} is due to a harmonic potential, then the equation separates into three orthogonal coordinates. Along the z -direction, for example, if the force is $F_z = -kz$,

$$\partial_t p(z, t; z', 0) = D (\partial_z^2 + \beta k \partial_z z) p(z, t; z', 0)$$

Substituting $k = m\omega_z^2$, this has the Green's function

$$p(z, t; z', 0) = \frac{1}{\sqrt{2\pi k_B T S(t)/k}} \exp \left[-\frac{(z - z' e^{-2t/\tau})^2}{2k_B T S(t)/k} \right] \quad (\text{F.2})$$

where $S(t) = 1 - e^{-4t/\tau}$ and $\tau = 2k_B T/kD$, where D is the diffusion constant. Accordingly, the density profile at time t will be given by

$$\begin{aligned} n(z, t) &= \int_{-\infty}^{\infty} dz' n(z', 0) p(z, t; z', 0) \\ &= n_0 \sqrt{2} \left[\frac{\exp \left[-z^2 / \left(DS(t)\tau + \frac{2e^{-4t/\tau}}{m\beta\omega_z^2} \right) \right]}{\sqrt{2e^{-4t/\tau} + DmS(t)\tau\beta\omega_z^2}} - \frac{\exp \left[-z^2 / \left(DS(t)\tau + \frac{2e^{-4t/\tau}}{m\beta\omega_r^2} \right) \right]}{\sqrt{2e^{-4t/\tau} + DmS(t)\tau\beta\omega_r^2}} \right] \\ &= n_0 \left[\exp \left[-\beta m \omega_z^2 z^2 / 2 \right] - \frac{\exp \left[-\beta m \omega_r^2 z^2 / 2 (\alpha^2 S(t) + e^{-4t/\tau}) \right]}{\sqrt{\alpha^2 S(t) + e^{-4t/\tau}}} \right] \end{aligned} \quad (\text{F.3})$$

where $\alpha = \omega_r/\omega_z$, and we've used the profile in figure F.1 for $n(z', 0)$. The density recovers to its equilibrium value (sans the particles kicked out) in much less than time τ , as seen in figure F.2. The density at the center of the trap behaves as

$$n(0, t) = n_0 \left[1 - \frac{1}{\sqrt{\alpha^2 - e^{-4t/\tau}(\alpha^2 - 1)}} \right] \quad (\text{F.4})$$

For short times, this is linear in time with a slope $2n_0(\alpha^2 - 1)/\tau$, whereas for long times, this asymptotes to $n_0(\alpha - 1)/\alpha$. The $t = 0$ slope fixes the rate at which particles can flow

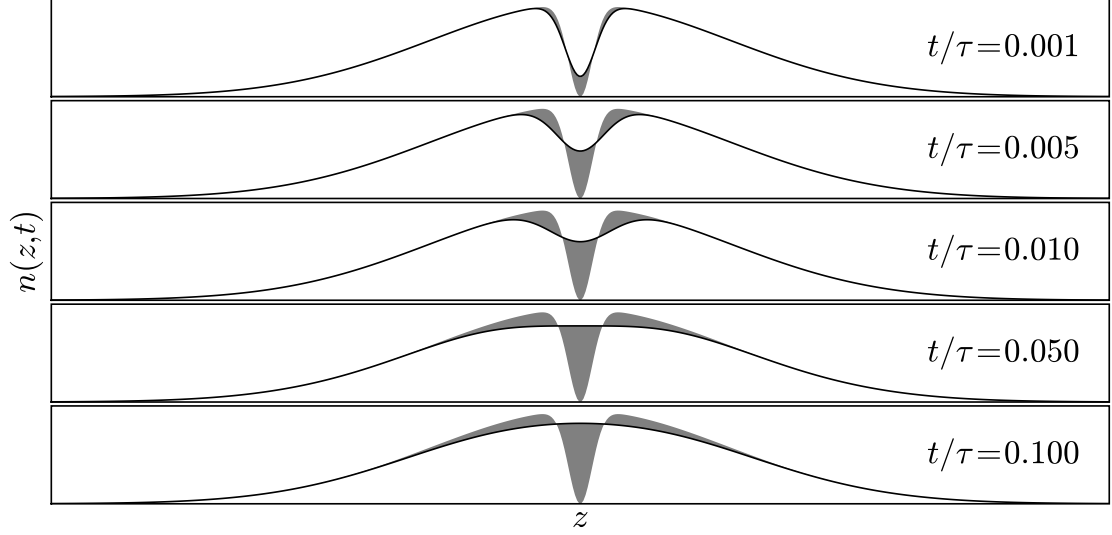


FIGURE F.2: After being “bleached”, the trap center recovers very quickly. The solid black line is the density profile at different times t/τ , while the shaded area is the difference from the $t = 0$ bleached profile.

diffusively to the center of the trap. The total number of particles kicked out is

$$N_{\text{kicked}} = \int_{-\infty}^{\infty} dz n_0 e^{-\beta m \omega_r^2 z^2 / 2} = n_0 \times \frac{\sqrt{2\pi}}{\omega_r \sqrt{m\beta}}$$

To estimate the particle flux into the center, we can assume, therefore, that the total particle number in the bleached region is the central density $n(0, t)$ times the “width” $\sqrt{2\pi}/\omega_r \sqrt{m\beta}$. Therefore the particle flux into the bleached region for short times is

$$\dot{N}_{\text{bleached}} = \frac{2n_0}{\tau} (\alpha^2 - 1) \frac{\sqrt{2\pi}}{\omega_r \sqrt{\beta m}} = \frac{(\alpha^2 - 1) n_c D (2\pi)^{3/2}}{\omega_r \alpha^2 \beta^{3/2} m a} \quad (\text{F.5})$$

where β is the dimensionless form, i.e., multiplied by $1/ma^2$. The diffusion constant from equation (5.13), fed into this formula, gives

$$\begin{aligned} \dot{N}_{\text{bleached}} &= \frac{(n_c a^3) (\alpha^2 - 1) (2\pi)^{3/2}}{\alpha^2 (ma^2)^2 \beta (n_b a^3) \lambda_f^2 (3\pi^3)^{1/2} \omega_r} = \frac{4e_{\text{F}\uparrow}^2 (n_c a^3) (\alpha^2 - 1) (2\pi)^{3/2}}{\alpha^2 \beta (n_b a^3) \lambda_f^2 (3\pi^3)^{1/2} \omega_r} \\ &= \omega_r \frac{8\sqrt{2/3} (\alpha^2 - 1) (n_c a^3) (\omega_{\text{F}}/\omega_r)^2}{\alpha^2 \beta \lambda_f^2 (n_b a^3)} \end{aligned} \quad (\text{F.6})$$

where we’ve used $ak_{\text{F}\uparrow} = 1$. Since we cannot pump faster than this rate of inflow towards a depleted center, this is an upper limit on our pumping rate.

APPENDIX G
FESHBACH RESONANCE

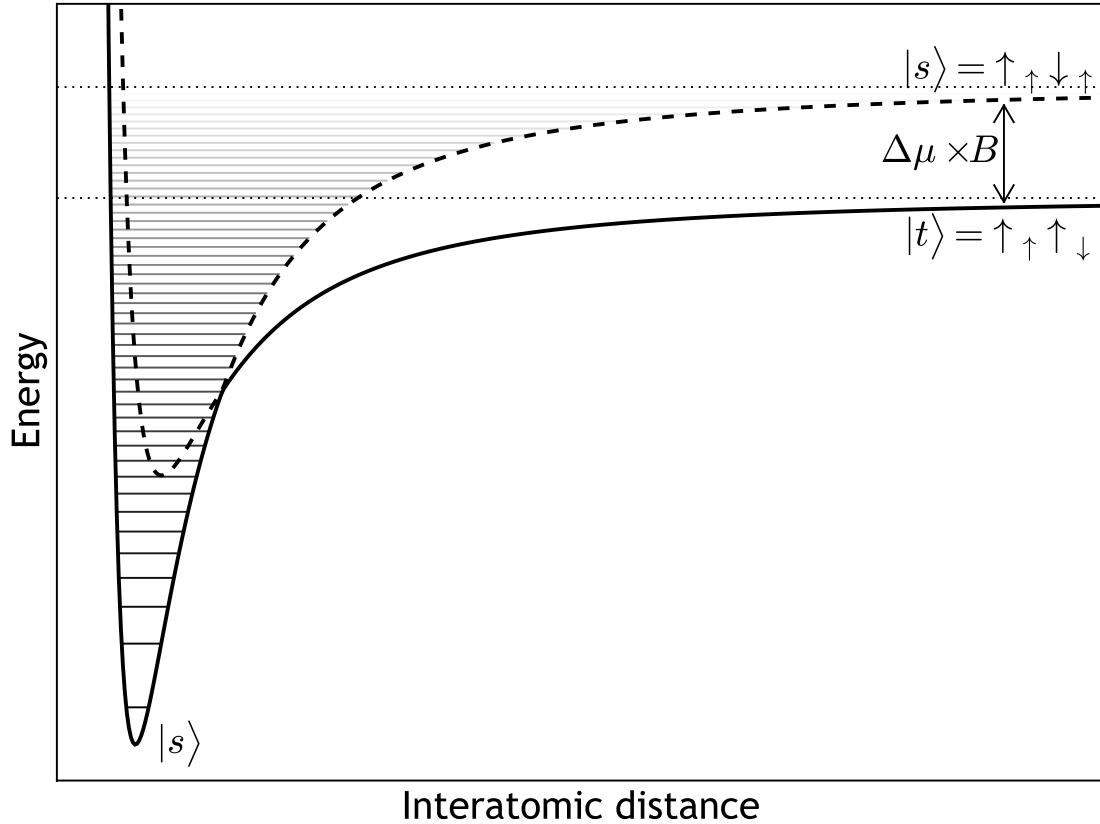


FIGURE G.1: A singlet state will have many bound states, denoted by gradually fading horizontal lines above. Feshbach resonance is the coincidence of the binding energy of a one of those states to the asymptotic potential energy of the atoms in the unbound triplet state $|t\rangle$. The terms ‘singlet’ and ‘triplet’ do not refer to the total angular momentum F but only the electronic part S . The subscripted arrows above are nuclear spins, B is an external magnetic field, and $\Delta\mu$ is the magnetic moment difference between the two states.

Feshbach resonance is a remarkable tool in atomic physics; by changing an external magnetic field, inter-atomic interactions can be tuned over a wide range, from strongly attractive through non-interacting all the way to strongly repulsive. Consider a pair of atoms with a single electron in its valence shell ($S = 1/2$) and nuclear spin $I = 1/2$. This will have four hyperfine states, $|F = 0, m_F = 0\rangle$ and $|F = 1, m_F = 0, \pm 1\rangle$, which will be non-degenerate in the presence of a magnetic field B . Two such atoms will form a bound

molecule only when the electronic wavefunction is a singlet $|s\rangle$, i.e., the atoms are in the $|m_s = +1/2\rangle$ and $|m_s = -1/2\rangle$ states (dashed line in figure G.1). On the other hand, if the electronic wavefunction is a triplet $|t\rangle$, let's say $|m_s = +1/2\rangle$ and $|m_s = +1/2\rangle$, they will not form a molecule (solid line in figure G.1). Plotted against the inter-atomic distance, the singlet state will have a deeper potential well than the triplet state, whereas when the atoms are far apart, their energies in the presence of a B field will be different since the electronic magnetic moment is almost 2,000 times higher than the nuclear magnetic moment.

States $|s\rangle$ and $|t\rangle$ are related by an electronic and a nuclear spin flip. The coupling between I and S can be written

$$\mathbf{I} \cdot \mathbf{S} = \frac{1}{2} [\mathbf{I}_+ \mathbf{S}_- + \mathbf{I}_- \mathbf{S}_+] + \mathbf{I}_z \mathbf{S}_z$$

which mixes the two states, creating an avoided level crossing as shown in figure G.1. Thus when two atoms, initially in the triplet state, approach each other, there is a finite probability for them to flip two spins and end up in the singlet state, following the solid curve in the figure. If the initial potential energy in $|t\rangle$ is equal to a bound state energy in $|s\rangle$, then this probability is very high, and a “Rabi flop” between the two states takes a very long time. The system is said to be *on resonance*.

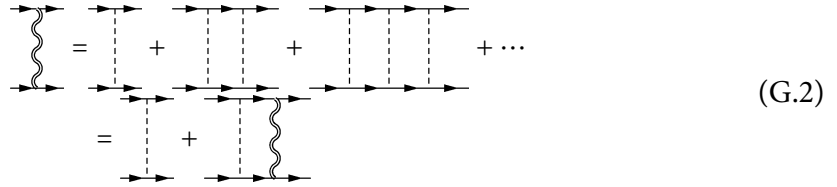
On resonance, two free atoms spend a lot of time close to each other in a “bound” molecular state (with $E_b = 0$), increasing the effect of their interaction. If, on the other hand, the system is slightly detuned from resonance, the “Rabi flops” are more frequent, and interaction effects decrease. In effect, tuning the system close to a Feshbach resonance is a way of controlling the interaction energy between atoms. In the limit of a dilute gas of atoms, the interaction energy of the gas, the two-body scattering length and the proximity to a Feshbach resonance can be connected using a simple two-particle scattering Hamiltonian.

G.1 Scattering theory

Consider a Hamiltonian with only two-particle point interactions between fermions¹

$$\mathcal{H} = \sum_{\mathbf{k},\sigma} \epsilon_{\mathbf{k}} \Psi_{\mathbf{k},\sigma}^\dagger \Psi_{\mathbf{k},\sigma} + U \sum_{\mathbf{k},\mathbf{p},\mathbf{q}} \Psi_{\frac{\mathbf{k}+\mathbf{p},\uparrow}^{\dagger}} \Psi_{\frac{\mathbf{k}-\mathbf{p},\downarrow}^{\dagger}} \Psi_{\frac{\mathbf{k}-\mathbf{q},\downarrow}^{\dagger}} \Psi_{\frac{\mathbf{k}+\mathbf{q},\uparrow}^{\dagger}} \quad (\text{G.1})$$

Since this Hamiltonian conserves total momentum, the total momenta for the two-particle initial and final states must be equal. Let's say this total momentum is \mathbf{q} . Diagrammatically, a two-particle scattering matrix can be drawn for this potential:



where the double wiggly line is for the scattering matrix between $\Psi_{\mathbf{p}+\mathbf{q}/2,\uparrow}^\dagger \Psi_{-\mathbf{p}+\mathbf{q}/2,\downarrow}^\dagger |\text{vac}\rangle$ and $\Psi_{\mathbf{p}'+\mathbf{q}/2,\uparrow}^\dagger \Psi_{-\mathbf{p}'+\mathbf{q}/2,\downarrow}^\dagger |\text{vac}\rangle$, the dashed line is U , and the thin solid lines are fermion propagators. If the total energy of the incoming particles (as well as the outgoing particles) be ω then the above diagram can be summarized in the Dyson equation

$$\begin{aligned} & T\left(\frac{\mathbf{q}}{2} + \mathbf{p}, \frac{\mathbf{q}}{2} - \mathbf{p}, \frac{\mathbf{q}}{2} + \mathbf{p}', \frac{\mathbf{q}}{2} - \mathbf{p}'; \omega\right) \\ &= U \left[1 + \sum_{\mathbf{k},\nu} G_\uparrow\left(\frac{\mathbf{q}}{2} + \mathbf{k}, \frac{\omega}{2} + \nu\right) G_\downarrow\left(\frac{\mathbf{q}}{2} - \mathbf{k}, \frac{\omega}{2} - \nu\right) T\left(\frac{\mathbf{q}}{2} + \mathbf{k}, \frac{\mathbf{q}}{2} - \mathbf{k}, \frac{\mathbf{q}}{2} + \mathbf{p}', \frac{\mathbf{q}}{2} - \mathbf{p}'; \omega\right) \right] \end{aligned} \quad (\text{G.3})$$

where $G_{\uparrow,\downarrow}^{-1}(\mathbf{p}, \omega) = \omega - \epsilon_{\mathbf{p}} + i\varepsilon$. In terms of the two-particle propagator $G_2(\mathbf{q}, \omega)$ defined by

$$G_2(\mathbf{q}, \omega) = \sum_{\mathbf{k},\nu} G_\uparrow\left(\frac{\mathbf{q}}{2} + \mathbf{k}, \frac{\omega}{2} + \nu\right) G_\downarrow\left(\frac{\mathbf{q}}{2} - \mathbf{k}, \frac{\omega}{2} - \nu\right) \quad (\text{G.4})$$

the scattering matrix (which depends only on \mathbf{q} and ω as well) is given by

$$T(\mathbf{q}, \omega) = \frac{1}{\frac{1}{U} - G_2(\mathbf{q}, \omega)} \quad (\text{G.5})$$

¹Point interaction between similar spins is forbidden by Pauli exclusion. If these were Bosons, we could have all sorts of scattering between different spins. While that theory is not more complicated in principle, we work out the Fermion case for a concrete example.

G_2 can be evaluated using some contour integration:

$$\begin{aligned} G_2(\mathbf{q}, \omega) &= -V \int \frac{d^3\mathbf{k}}{(2\pi)^3} \int_{-\infty}^{\infty} \frac{dv}{2\pi} \frac{1}{v - \left(\epsilon_{\frac{\mathbf{q}}{2}+\mathbf{k}} - \frac{\omega}{2} - i\varepsilon\right)} \frac{1}{v - \left(\frac{\omega}{2} - \epsilon_{\frac{\mathbf{q}}{2}-\mathbf{k}} + i\varepsilon\right)} \\ &= -V \int \frac{d^3\mathbf{k}}{(2\pi)^3} \frac{1}{\omega - \epsilon_{\frac{\mathbf{q}}{2}-\mathbf{k}} - \epsilon_{\frac{\mathbf{q}}{2}+\mathbf{k}} + 2i\varepsilon} \end{aligned} \quad (\text{G.6})$$

This integral is divergent due to the contribution from large \mathbf{k} , so we subtract the divergence and define

$$G_2(\mathbf{q}, \omega) = -V \int \frac{d^3\mathbf{k}}{(2\pi)^3} \left[\frac{1}{\omega - \epsilon_{\frac{\mathbf{q}}{2}-\mathbf{k}} - \epsilon_{\frac{\mathbf{q}}{2}+\mathbf{k}} + 2i\varepsilon} + \frac{1}{2\epsilon_{\mathbf{k}}} \right] \quad (\text{G.7})$$

and this ‘‘convergence term’’ gets added to $1/U$ as well, and we call the whole thing the *renormalized* U which is physically relevant. Doing another contour integral, we get

$$G_2(\mathbf{q}, \omega) = -\frac{imV}{8\pi} \sqrt{4m\omega - \mathbf{q}^2} \quad (\text{G.8})$$

Now suppose the incoming particles have momenta $\frac{\mathbf{q}}{2} + \mathbf{k}$ and $\frac{\mathbf{q}}{2} - \mathbf{k}$. Then $\omega = (\mathbf{q}^2 + 4\mathbf{k}^2)/4m$, and we see that the scattering matrix only depends on the relative momentum:

$$T(\mathbf{k}) = \frac{1}{\frac{1}{U} + i\frac{mV\mathbf{k}}{4\pi}} \quad (\text{G.9})$$

Now the s-wave phase shift δ_0 is related to the on-shell scattering matrix by

$$\frac{e^{i\delta_0}}{k} \sin \delta_0 \propto T(k) \quad \Rightarrow \quad \tan \delta_0 = -\frac{mVUk}{4\pi} \quad (\text{G.10})$$

The s-wave scattering length a is given by

$$\lim_{k \rightarrow 0} k \cot \delta_0 = -\frac{1}{a} = -\frac{4\pi}{mVU} \quad \Rightarrow \quad a = \frac{mVU}{4\pi} \quad (\text{G.11})$$

This connects a macroscopically measurable scattering length a with a microscopic parameter U . Further, we know that bound states appear as poles of $T(\mathbf{q} = 0, \omega = -E_b)$:

$$\frac{mV}{4\pi a} - \frac{mV}{8\pi} \sqrt{4mE_b} = 0 \quad \Rightarrow \quad E_b = \frac{1}{ma^2} \quad (\text{G.12})$$

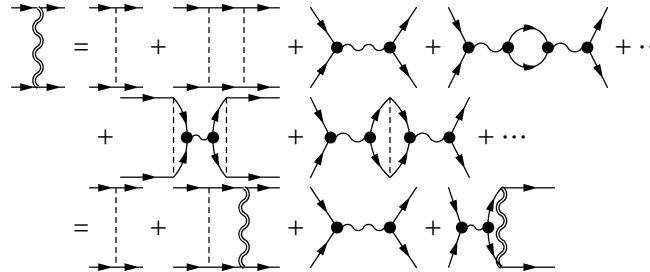
which also says that a bound state first appears when $a \rightarrow \infty$. Since we know that a bound state appears at a Feshbach resonance, the condition for Feshbach resonance is therefore $a = \infty$. Next we will see how this can be achieved using a magnetic field.

G.2 Effect of a magnetic field

In the presence of a magnetic field B , the up and down spins will have different energies. Further, near a resonance, we should have a bosonic bound state (denoted by the operator ϕ) with twice the mass of the fermionic particles, and a coupling between the two states with strength g [228]:

$$\begin{aligned} \mathcal{H} = & \sum_{\mathbf{k},\sigma} \epsilon_{\mathbf{k}} \psi_{\mathbf{k},\sigma}^\dagger \psi_{\mathbf{k},\sigma} + \sum_{\mathbf{k}} \left(\frac{1}{2} \epsilon_{\mathbf{k}} + 2\nu \right) \phi_{\mathbf{k}}^\dagger \phi_{\mathbf{k}} + U \sum_{\mathbf{k},\mathbf{p},\mathbf{q}} \psi_{\frac{\mathbf{k}}{2}+\mathbf{p},\uparrow}^\dagger \psi_{\frac{\mathbf{k}}{2}-\mathbf{p},\downarrow}^\dagger \psi_{\frac{\mathbf{k}}{2}-\mathbf{q},\downarrow} \psi_{\frac{\mathbf{k}}{2}+\mathbf{q},\uparrow} \\ & + g \sum_{\mathbf{k},\mathbf{p}} \left[\phi_{\mathbf{k}}^\dagger \psi_{\frac{\mathbf{k}}{2}+\mathbf{p},\uparrow} \psi_{\frac{\mathbf{k}}{2}-\mathbf{p},\downarrow} + \psi_{\frac{\mathbf{k}}{2}-\mathbf{p},\downarrow}^\dagger \psi_{\frac{\mathbf{k}}{2}+\mathbf{p},\uparrow}^\dagger \phi_{\mathbf{k}} \right] \end{aligned} \quad (\text{G.13})$$

where 2ν is the energy detuning between the bosonic pair and two free fermions². The scattering matrix will now have extra terms corresponding to formation and dissociation of pairs:



$$(\text{G.14})$$

where the double wiggly line is the full T-matrix, the single wiggly line is a boson line corresponding to ϕ , the dashed straight line is the interaction U , the dots correspond to g , and the solid straight lines are fermion lines for ψ . The resulting Dyson equation is

$$\begin{aligned} & T \left(\frac{\mathbf{q}}{2} + \mathbf{p}, \frac{\mathbf{q}}{2} - \mathbf{p}, \frac{\mathbf{q}}{2} + \mathbf{p}', \frac{\mathbf{q}}{2} - \mathbf{p}'; \omega \right) \\ & = [U + g^2 G_b(\mathbf{q}, \omega)] \times \left[1 + \sum_{\mathbf{k}, \omega'} G_\uparrow \left(\frac{\mathbf{q}}{2} + \mathbf{k}, \frac{\omega}{2} + \omega' \right) G_\downarrow \left(\frac{\mathbf{q}}{2} - \mathbf{k}, \frac{\omega}{2} - \omega' \right) \times \right. \\ & \left. T \left(\frac{\mathbf{q}}{2} + \mathbf{k}, \frac{\mathbf{q}}{2} - \mathbf{k}, \frac{\mathbf{q}}{2} + \mathbf{p}', \frac{\mathbf{q}}{2} - \mathbf{p}'; \omega \right) \right] \end{aligned} \quad (\text{G.15})$$

²Note that the bosonic pair is actually inert to a magnetic field, and in fact the fermionic energies should be shifted, for example $\epsilon_{\mathbf{k},\uparrow} = \epsilon_{\mathbf{k}} - \mu(B - B_0)$ and $\epsilon_{\mathbf{k},\downarrow} = \epsilon_{\mathbf{k}} + \mu(B - B_0)$. A canonical transformation is typically performed to shift the effect of the magnetic field on to the Bosonic part [229, 230] for handling convenience that will become apparent below.

where G_b is the propagator for the bosonic pair. In structure, this is very similar to equation (G.3), and again T depends only on the total energy ω and total momentum \mathbf{q} . The only difference is that U is shifted:

$$U \rightarrow U + \frac{g^2}{\omega - \epsilon_{\mathbf{q}}/2 - 2\nu + i\varepsilon} \quad (\text{G.16})$$

so that the scattering matrix is

$$T(\mathbf{q}, \omega) = \frac{1}{\frac{1}{U + g^2 G_b(\mathbf{q}, \omega)} - G_2(\mathbf{q}, \omega)} \quad (\text{G.17})$$

Again, using $\omega = (\mathbf{q}^2 + 4\mathbf{k}^2)/4m$ we get

$$a = -\lim_{k \rightarrow 0} \frac{\tan \delta_0}{k} = \frac{mV}{4\pi} \left[U - \frac{g^2}{2\nu} \right] \quad (\text{G.18})$$

If we call $mVU/4\pi = a_{\text{bg}}$, as in the scattering length in the absence of a resonance ($g = 0$), and note that the detuning $2\nu \propto B - B_0$ where B_0 is the field on resonance, we can write

$$a = a_{\text{bg}} \left(1 + \frac{\Delta B}{B - B_0} \right) \quad (\text{G.19})$$

where the characteristic width of a resonance ΔB depends on things such as g , a_{bg} , m , etc. This tells us that a Feshbach resonance ($a \rightarrow \infty$, $E_b = 0$) can be induced by tuning an external magnetic field. The binding energy is again found by looking for the pole of $T(0, -E_b)$. This will in general have three solutions, and the physical one will go to zero as $\nu \rightarrow 0$. While the full solution is messy, two of its limits are well-defined: for $\nu \rightarrow 0$, the resonance term g will dominate U , whereas far away from resonance, U is more important than g (see, e.g. [33] or [231]).

$$E_b \xrightarrow{\nu \rightarrow 0} (B - B_0)^2 \times \text{const.} \quad E_b \xrightarrow{\nu \rightarrow \infty} \Delta\mu(B - B) \quad (\text{G.20})$$

The binding energy is not linear in $B - B_0$ close to the resonance because a molecule is dressed up by fluctuations that take it to a dissociated pair and back. To finally relate a Feshbach resonance to the strength of interactions, we note that the interaction energy

per unit volume in terms of the particle density n is [32]

$$E_{\text{int}} \sim \frac{6an^2}{m} \quad (\text{G.21})$$

which means that by tuning an external magnetic field, experimentalists can tune the interaction energy relative to the kinetic energy ($\sim 6n^{5/3}/m$ per unit volume), taking it all the way from strongly attractive ($an^{1/3} \ll -1$) to strongly repulsive ($an^{1/3} \gg 1$) and everything in between. This is dramatically different from other condensed matter systems; we cannot, for example, just change the electron-electron interaction at the heart of superconductivity. As we shall see in the rest of this thesis, this tunable interaction has allowed us to use systems with Feshbach resonances to probe regimes previously considered unreachable.

APPENDIX H
EVALUATION OF THE SELF ENERGY

The summation over Matsubara frequencies in (3.14) can be converted into a contour integral with an extra Fermi function in the integrand. The sum can be written as a special case of a more general Matsubara sum

$$\frac{1}{\beta} \sum_{i\omega_n} h(i\omega_n)$$

where the fermionic Matsubara frequencies are $\omega_n = (2n + 1)\pi/\beta$. Note that the Fermi-Dirac function $f(z) = (e^{\beta z} + 1)^{-1}$ has poles at precisely $z_n = i\omega_n$ (blue circles in figure H.1), with residue $-1/\beta$ at every pole. Hence, the above sum can be written

$$\frac{1}{\beta} \sum_{i\omega_n} h(i\omega_n) = - \sum_n h(z_n) \text{Res}_{z \rightarrow z_n} f(z) \quad (\text{H.1})$$

If all the poles and branch cuts (red stars and thick orange lines, respectively, in figure H.1) of the function $h(z)$ are on the real axis,¹ then this sum is

$$- \sum_n \text{Res}_{z \rightarrow z_n} f(z) h(z) = \frac{1}{2\pi i} \oint_{C'} dz f(z) h(z) \quad (\text{H.2})$$

where C' is the dashed blue contour in figure H.1. Since the function $f(z)$ goes to zero exponentially for large $|z|$ away from the imaginary axis, the dashed blue contour C' can be deformed into the dotted red contour C'' . Further, since $f(z)$ does not have a pole on the real axis, contour C'' can be deformed into the solid green contour C in figure H.1 to include the origin. Hence a Matsubara sum turns into a contour integral

$$\frac{1}{\beta} \sum_{i\omega_n} h(i\omega_n) = \frac{1}{2\pi i} \oint_C dz f(z) h(z) \quad (\text{H.3})$$

This contour integral will only pick up the poles and branch cuts of $h(z)$ on the real axis. If the Matsubara sum is over bosonic frequencies, the Fermi-Dirac function is replaced by the Bose-Einstein function.

¹For $r > r_c$, i.e., when the normal fluid is stable, all the poles of $\tilde{\Theta}(q, z)$ are real. Also, all the poles of the Fermion Green's function in (3.14) are obviously real too. So our h satisfies this constraint.

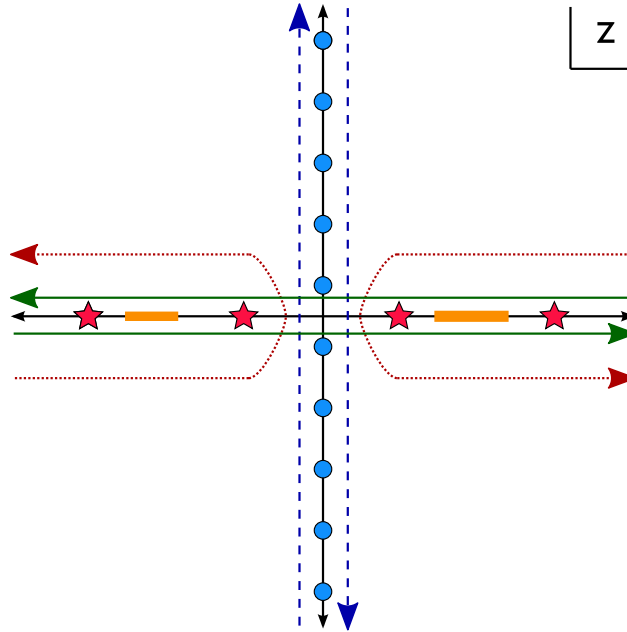


FIGURE H.1: If the poles (red stars) and branch cuts (thick orange lines) of $h(z)$ are all on the real axis, then we can sum $h(z)$ over $z_n = i\omega_n$ (blue circles) by integrating $h(z)f(z)$ along the dashed blue contour. That contour is equivalent to the dotted red contour, which can be deformed into the solid green contour.

To use this recipe for summing (3.14), we have to integrate the summand of (3.14) times a Fermi-Dirac function over the straight line contours (solid blue and dashed green) of figure H.2. But at $T = 0$, $f(z) = 1$ for $\Re(z) < 0$ and $f(z) = 0$ for $\Re(z) > 0$, so only the solid blue contour contributes in figure H.2 and the green dashed contour does not contribute. Unless there is a pole at the origin, we can close the blue contour through the origin.

In eq. (3.14) we shift the momentum so that the sum of momenta is an argument of $G_{-\sigma}$, and then we can do the angular integral. We also restrict ourselves to unitarity, where $(a_s k_F^\dagger)^{-1} \rightarrow 0$ in eq. (3.10). Again expressing everything in terms of dimensionless

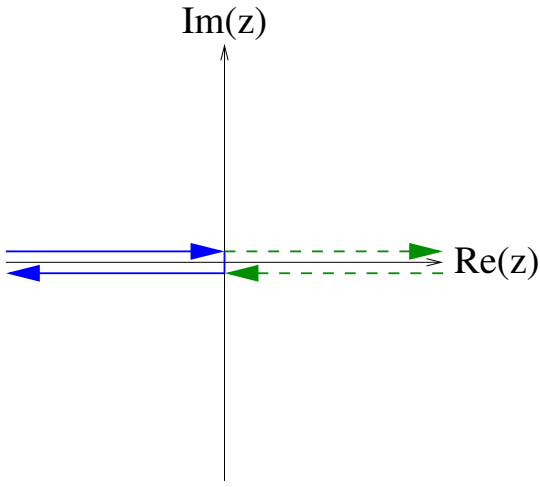


FIGURE H.2: The contour over which to evaluate (3.14). The green dashed part does not contribute because $f(z) \rightarrow 0$ at $T \rightarrow 0$.

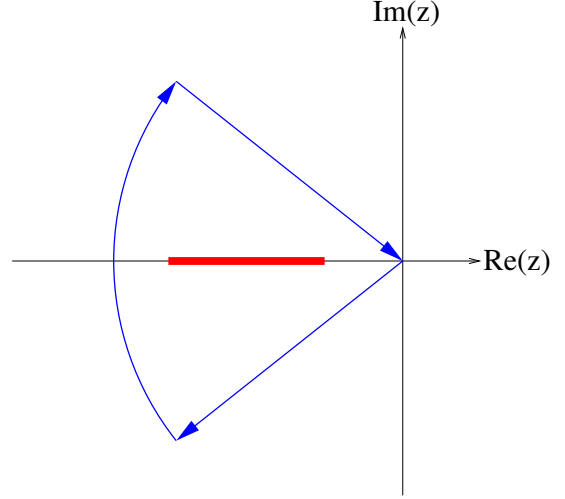


FIGURE H.3: The modified contour for evaluating (H.4). The thick red line is where the branch cut and poles are.

variables (k is scaled by k_F^\dagger), we get

$$\begin{aligned} \frac{m}{(k_F^\dagger)^2} \Sigma_\downarrow(k, 0) &= \frac{i}{2\pi^2} \int_0^\infty q dq \oint_{\mathbb{C}} \frac{dz}{\tilde{\Theta}(q, z)} \frac{1}{k} \log \left[\frac{(2z+1)^2 - (k-q)^2}{(2z+1)^2 - (k+q)^2} \right] \\ \frac{m}{(k_F^\dagger)^2} \Sigma_\uparrow(k, 0) &= \frac{i}{2\pi^2} \int_0^\infty q dq \oint_{\mathbb{C}} \frac{dz}{\tilde{\Theta}(q, z)} \frac{1}{k} \log \left[\frac{(2z+r^2)^2 - (k-q)^2}{(2z+r^2)^2 - (k+q)^2} \right] \end{aligned} \quad (\text{H.4})$$

where \mathbb{C} is the solid blue contour in figure H.2. At $r = r_c$, $\tilde{\Theta}(q, z)$ has a pole for a certain q at $z = 0$ according to the modified Thouless criterion of (3.13). For $r < r_c$, the pole is on the positive real axis, and the blue contour can be closed through the origin. The location of the branch cuts and poles of the integrands in (H.4) are shown in figure H.3 by a thick red line. Except for the pole from (3.13) (which does not count), all singularities are on the negative real axis, and the singularity farthest to the left is the branch cut from the logarithm. This branch cut starts at

$$z_{\min} = \frac{1}{4}q^2 - \frac{1}{2}(1+r^2) \quad (\text{H.5})$$

There may be a pole for $\Re(z) < 0$ as well, but that lies on the red line as well. The end of the branch cut is to the left of the origin; we can therefore deform the solid blue contour of

figure H.2 into the pie-shaped blue contour of figure H.3. We numerically integrate over this pie-shaped contour, finding that the integrands are well-behaved. This should be contrasted with the contour in figure H.2, over which the integrand is highly oscillatory. The self energies of the two species at their respective Fermi surfaces are given by $\Sigma_{\downarrow}(r)$ and $\Sigma_{\uparrow}(1)$ from eqs. (H.4). The results are shown in figure 3.1 in the main text.

BIBLIOGRAPHY

- [1] P. W. Anderson, *Science* **177**, 393 (1972).
- [2] G. B. Partridge, *et al.*, *Physical Review Letters* **97**, 190407 (2006).
- [3] Y. il Shin, C. H. Schunck, A. Schirotzek, W. Ketterle, *Nature* **451**, 689 (2008).
- [4] D. Gurnett, A. Bhattacharjee, *Introduction to Plasma Physics: With Space and Laboratory Applications* (Cambridge University Press, 2005).
- [5] K. Gavroglu, *Fritz London: A Scientific Biography* (Cambridge University Press, 2005).
- [6] A. Pais, *Subtle Is the Lord: The Science and the Life of Albert Einstein* (Oxford University Press, 2005).
- [7] A. Griffin, *Bose-Einstein Condensation in Atomic Gases* (IOS Press, Amsterdam, 1999), chap. A Brief History of Our Understanding of BEC: From Bose to Beliaev.
- [8] O. Penrose, L. Onsager, *Physical Review* **104**, 576 (1956).
- [9] N. Bogoliubov, *J. Phys. USSR* **11**, 23 (1947).
- [10] L. Landau, *Physical Review* **75**, 884 (1949).
- [11] J. Bardeen, L. N. Cooper, J. R. Schrieffer, *Physical Review* **108**, 1175 (1957).
- [12] L. Gorkov, *Sov. Phys. JETP* **7**, 505 (1958).
- [13] P. Nozières, S. Schmitt-Rink, *Journal of Low Temperature Physics* **59**, 195 (1985).
- [14] M. Randeria, *Bose-Einstein Condensation* (Cambridge University Press, 1996), chap. Crossover from BCS Theory to Bose-Einstein Condensation, p. 355.
- [15] D. D. Osheroff, R. C. Richardson, D. M. Lee, *Physical Review Letters* **28**, 885 (1972).
- [16] A. J. Leggett, *Physical Review Letters* **29**, 1227 (1972).
- [17] A. Larkin, Y. Ovchinnikov, *Sov. Phys. JETP* **20**, 762 (1965).
- [18] P. Fulde, R. A. Ferrell, *Physical Review* **135**, A550 (1964).
- [19] M. Anderson, J. Ensher, M. Matthews, C. Wieman, E. Cornell, *Science* **269**, 198 (1995).
- [20] K. Davis, *et al.*, *Physical Review Letters* **75**, 3969 (1995).
- [21] C. Bradley, C. Sackett, J. Tollett, R. Hulet, *Physical Review Letters* **75**, 1687 (1995).
- [22] S. Jochim, *et al.*, *Science* **302**, 2101 (2003).

- [23] C. A. Regal, M. Greiner, D. S. Jin, *Physical Review Letters* **92**, 040403 (2004).
- [24] C. A. Sá de Melo, *Physics Today* pp. 45–51 (2008).
- [25] P. Rodgers, *Physics World* **18**, 8 (2005).
- [26] H. J. Metcalf, *Laser Cooling and Trapping*, Graduate Texts in Contemporary Physics (Springer, 2007).
- [27] L. Pollack, S. Buchman, T. J. Greytak, *Physical Review B* **45**, 2993 (1992).
- [28] D. G. Fried, *et al.*, *Physical Review Letters* **81**, 3811 (1998).
- [29] T. Hänsch, A. Schawlow, *Optics Communications* **13**, 68 (1975).
- [30] S. Chu, L. Hollberg, J. Bjorkholm, A. Cable, A. Ashkin, *Physical Review Letters* **55**, 48 (1985).
- [31] C. Cohen-Tannoudji, W. Phillips, *Physics Today* **October**, 33 (1990).
- [32] G. Baym, C. Pethick, *Physical Review Letters* **76**, 6 (1996).
- [33] R. A. Duine, H. T. C. Stoof, *Journal of Optics B: Quantum and Semiclassical Optics* **5**, S212 (2003).
- [34] C. Bradley, C. Sackett, R. Hulet, *Physical Review Letters* **78**, 985 (1997).
- [35] S. Cornish, N. Claussen, J. Roberts, E. Cornell, C. E. Wieman, *Physical Review Letters* **85**, 1795 (2000).
- [36] G. Modugno, *et al.*, *Science* **294**, 1320 (2001).
- [37] A. Robert, *et al.*, *Science* **292**, 461 (2001).
- [38] F. Pereira Dos Santos, *et al.*, *Physical Review Letters* **86**, 3459 (2001).
- [39] T. Weber, J. Herbig, M. Mark, H.-C. Nagerl, R. Grimm, *Science* **299**, 232 (2003).
- [40] Y. Takasu, *et al.*, *Physical Review Letters* **91**, 040404 (2003).
- [41] A. Griesmaier, J. Werner, S. Hensler, J. Stuhler, T. Pfau, *Physical Review Letters* **94**, 160401 (2005).
- [42] D. H. J. O'Dell, S. Giovanazzi, C. Eberlein, *Physical Review Letters* **92**, 250401 (2004).
- [43] L. Santos, G. V. Shlyapnikov, P. Zoller, M. Lewenstein, *Physical Review Letters* **85**, 1791 (2000).
- [44] K. Góral, L. Santos, *Physical Review A* **66**, 023613 (2002).

- [45] S. Giovanazzi, A. Görlitz, T. Pfau, *Physical Review Letters* **89**, 130401 (2002).
- [46] J. Werner, *et al.*, *Physical Review Letters* **94**, 183201 (2005).
- [47] E. A. Donley, N. R. Claussen, S. T. Thompson, C. E. Wieman, *Nature* **417**, 529 (2002).
- [48] E. A. Donley, *et al.*, *Nature* **412**, 295 (2001).
- [49] N. Claussen, E. Donley, S. Thompson, C. Wieman, *Physical Review Letters* **89**, 010401 (2002).
- [50] E. A. Burt, *et al.*, *Physical Review Letters* **79**, 337 (1997).
- [51] E. J. Yarmchuk, M. J. V. Gordon, R. E. Packard, *Physical Review Letters* **43**, 214 (1979).
- [52] U. Essmann, H. Träuble, *Physics Letters A* **24**, 526 (1967).
- [53] J. R. Abo-Shaeer, C. Raman, J. M. Vogels, W. Ketterle, *Science* **292**, 476 (2001).
- [54] K. W. Madison, F. Chevy, V. Bretin, J. Dalibard, *Physical Review Letters* **86**, 4443 (2001).
- [55] P. Krüger, Z. Hadzibabic, J. Dalibard, *Physical Review Letters* **99**, 040402 (2007).
- [56] Z. Hadzibabic, P. Krüger, M. Cheneau, B. Battelier, J. Dalibard, *Nature* **441**, 1118 (2006).
- [57] S. Burger, *et al.*, *Physical Review Letters* **83**, 5198 (1999).
- [58] J. Denschlag, *et al.*, *Science* **287**, 97 (2000).
- [59] D. M. Stamper-Kurn, H.-J. Miesner, S. Inouye, M. R. Andrews, W. Ketterle, *Physical Review Letters* **81**, 500 (1998).
- [60] C. Orzel, A. K. Tuchman, M. L. Fenselau, M. Yasuda, M. A. Kasevich, *Science* **291**, 2386 (2001).
- [61] T. Kinoshita, T. Wenger, D. S. Weiss, *Science* **305**, 1125 (2004).
- [62] E. W. Hagley, *et al.*, *Science* **283**, 1706 (1999).
- [63] M. Greiner, O. Mandel, T. Esslinger, T. W. Hänsch, I. Bloch, *Nature* **415**, 39 (2002).
- [64] J. Billy, *et al.*, *Nature* **453**, 891 (2008).
- [65] G. Roati, *et al.*, *Nature* **453**, 895 (2008).
- [66] J. R. Anglin, W. Ketterle, *Nature* **416**, 211 (2002).

- [67] K. Huang, *Statistical Mechanics* (John Wiley & Sons, Singapore, 2000), second edn.
- [68] A. Truscott, K. Strecker, W. McAlexander, G. Partridge, R. Hulet, *Science* **291**, 2570 (2001).
- [69] B. DeMarco, D. Jin, *Science* **285**, 1703 (1999).
- [70] A. Derevianko, W. R. Johnson, M. S. Safronova, J. F. Babb, *Physical Review Letters* **82**, 3589 (1999).
- [71] G. Ferrari, *Physical Review A* **59**, R4125 (1999).
- [72] K. M. O'Hara, M. E. Gehm, S. R. Granade, S. Bali, J. E. Thomas, *Physical Review Letters* **85**, 2092 (2000).
- [73] F. Schreck, *et al.*, *Physical Review A* **64**, 011402(R) (2001).
- [74] G. Partridge, W. Li, R. Kamar, Y. Liao, R. Hulet, *Science* **311**, 503 (2006).
- [75] B. DeMarco, S. B. Papp, D. S. Jin, *Physical Review Letters* **86**, 5409 (2001).
- [76] B. DeMarco, D. S. Jin, *Physical Review Letters* **88**, 040405 (2002).
- [77] E. Wille, *et al.*, *Physical Review Letters* **100**, 053201 (2008).
- [78] C. A. Regal, C. Ticknor, J. L. Bohn, D. S. Jin, *Physical Review Letters* **90**, 053201 (2003).
- [79] J. Zhang, *et al.*, *Physical Review A* **70**, 030702 (2004).
- [80] C. H. Schunck, Y. il Shin, A. Schirotzek, W. Ketterle, *Nature* **454**, 739 (2008).
- [81] T. Stöferle, H. Moritz, K. Günter, M. Köhl, T. Esslinger, *Physical Review Letters* **96**, 030401 (2006).
- [82] J. K. Chin, *et al.*, *Nature* **443**, 961 (2006).
- [83] A. Leggett, *Modern trends in the theory of condensed matter*, Lecture Notes in Physics (Springer-Verlag, Heidelberg, 1980), chap. Diatomic molecules and Cooper pairs, pp. 13–27.
- [84] A. J. Leggett, *Le Journal de Physique Colloques* **41**, C7 (1980).
- [85] W. Meissner, R. Ochsenfeld, *Naturwissenschaften* **21**, 787 (1933).
- [86] W. S. Corak, B. B. Goodman, C. B. Satterthwaite, A. Wexler, *Physical Review* **96**, 1442 (1954).
- [87] W. S. Corak, B. B. Goodman, C. B. Satterthwaite, A. Wexler, *Physical Review* **102**, 656 (1956).

- [88] R. E. Glover, M. Tinkham, *Physical Review* **104**, 844 (1956).
- [89] R. E. Glover, M. Tinkham, *Physical Review* **108**, 243 (1957).
- [90] W. L. McMillan, *Physical Review* **167**, 331 (1968).
- [91] E. Maxwell, *Physical Review* **78**, 477 (1950).
- [92] C. A. Reynolds, B. Serin, W. H. Wright, L. B. Nesbitt, *Physical Review* **78**, 487 (1950).
- [93] I. Giaever, H. R. Hart, K. Megerle, *Physical Review* **126**, 941 (1962).
- [94] R. C. Jaklevic, J. Lambe, J. E. Mercereau, A. H. Silver, *Physical Review* **140**, A1628 (1965).
- [95] R. E. Eck, D. J. Scalapino, B. N. Taylor, *Physical Review Letters* **13**, 15 (1964).
- [96] N. Osakabe, *et al.*, *Physical Review A* **34**, 815 (1986).
- [97] D. D. Osheroff, W. J. Gully, R. C. Richardson, D. M. Lee, *Physical Review Letters* **29**, 920 (1972).
- [98] J. G. Bednorz, K. A. Müller, M. Takashige, *Science* **236**, 73 (1987).
- [99] J. Bednorz, M. Takashige, K. Müller, *Materials Research Bulletin* **22**, 819 (1987).
- [100] J. G. Bednorz, M. Takashige, K. A. Müller, *EPL (Europhysics Letters)* **3**, 379 (1987).
- [101] K. A. Müller, M. Takashige, J. G. Bednorz, *Physical Review Letters* **58**, 1143 (1987).
- [102] G. H. Dieke, E. S. Robinson, *Phys. Rev.* **80**, 1 (1950).
- [103] M. R. Schafroth, *Phys. Rev.* **96**, 1442 (1954).
- [104] M. R. Schafroth, *Phys. Rev.* **96**, 1149 (1954).
- [105] C. A. R. Sá de Melo, M. Randeria, J. R. Engelbrecht, *Physical Review Letters* **71**, 3202 (1993).
- [106] K. E. Strecker, G. B. Partridge, R. G. Hulet, *Physical Review Letters* **91**, 080406 (2003).
- [107] J. Cubizolles, T. Bourdel, S. J. J. M. F. Kokkelmans, G. V. Shlyapnikov, C. Salomon, *Physical Review Letters* **91**, 240401 (2003).
- [108] S. Jochim, *et al.*, *Physical Review Letters* **91**, 240402 (2003).
- [109] C. A. Regal, C. Ticknor, J. L. Bohn, D. S. Jin, *Nature* **424**, 47 (2003).
- [110] M. W. Zwierlein, *et al.*, *Phys. Rev. Lett.* **91**, 250401 (2003).

- [111] M. Greiner, C. A. Regal, D. S. Jin, *Nature* **426**, 537 (2003).
- [112] K. O'Hara, S. Hemmer, M. Gehm, S. Granade, J. Thomas, *Science* **298**, 2179 (2002).
- [113] J. Kinast, S. L. Hemmer, M. E. Gehm, A. Turlapov, J. E. Thomas, *Phys. Rev. Lett.* **92**, 150402 (2004).
- [114] M. Bartenstein, *et al.*, *Phys. Rev. Lett.* **92**, 203201 (2004).
- [115] J. Kinast, *et al.*, *Science* **307**, 1296 (2005).
- [116] C. Chin, *et al.*, *Science* **305**, 1128 (2004).
- [117] M. W. Zwierlein, *et al.*, *Phys. Rev. Lett.* **92**, 120403 (2004).
- [118] M. W. Zwierlein, C. H. Schunck, C. A. Stan, S. M. F. Raupach, W. Ketterle, *Phys. Rev. Lett.* **94**, 180401 (2005).
- [119] M. W. Zwierlein, J. R. Abo-Shaeer, A. Schirotzek, C. H. Schunck, W. Ketterle, *Nature* **435**, 1047 (2005).
- [120] Y. P. Chen, *et al.*, *Physical Review A (Atomic, Molecular, and Optical Physics)* **77**, 033632 (2008).
- [121] T. N. D. Silva, E. J. Mueller, *Physical Review A (Atomic, Molecular, and Optical Physics)* **73**, 051602 (2006).
- [122] B. S. Chandrasekhar, *Applied Physics Letters* **1**, 7 (1962).
- [123] A. Clogston, *Physical Review Letters* **9**, 266 (1962).
- [124] F. Chevy, *Physical Review A* **74**, 063628 (2006).
- [125] M. Zwierlein, A. Schirotzek, C. Schunck, W. Ketterle, *Science* **311**, 492 (2006).
- [126] Y. Shin, M. Zwierlein, C. Schunck, A. Schirotzek, W. Ketterle, *Physical Review Letters* **97**, 030401 (2006).
- [127] R. Hulet, Private communication (2009).
- [128] Y. il Shin, A. Schirotzek, C. H. Schunck, W. Ketterle, *Physical Review Letters* **101**, 070404 (2008).
- [129] C. Klempt, *et al.*, *Physical Review A (Atomic, Molecular, and Optical Physics)* **76**, 020701 (2007).
- [130] G. Roati, F. Riboli, G. Modugno, M. Inguscio, *Physical Review Letters* **89**, 150403 (2002).
- [131] M. L. Olsen, J. D. Perreault, T. D. Cumby, D. S. Jin, *arXiv:cond-mat/0810.1965* (2008).

- [132] Y. Shin, C. H. Schunck, A. Schirotzek, W. Ketterle, *Physical Review Letters* **99**, 090403 (2007).
- [133] J. W. Loram, K. A. Mirza, J. R. Cooper, W. Y. Liang, *Phys. Rev. Lett.* **71**, 1740 (1993).
- [134] A. Yazdani, B. A. Jones, C. P. Lutz, M. F. Crommie, D. M. Eigler, *Science* **275**, 1767 (1997).
- [135] Y. Kohsaka, *et al.*, *Science* **315**, 1380 (2007).
- [136] H.-B. Yang, *et al.*, *Nature* **456**, 77 (2008).
- [137] Y. He, C.-C. Chien, Q. Chen, K. Levin, *Physical Review A* **77**, 011602 (2008).
- [138] K. Levin, Q. Chen, *Physica C: Superconductivity* **460-462**, 347 (2007).
- [139] G. M. Bruun, H. Smith, *Physical Review A (Atomic, Molecular, and Optical Physics)* **75**, 043612 (2007).
- [140] S. Basu, E. J. Mueller, *Physical Review A (Atomic, Molecular, and Optical Physics)* **78**, 053603 (2008).
- [141] H. Feshbach, *Annals of Physics* **5**, 357 (1958).
- [142] S. Inouye, *et al.*, *Nature* **392**, 151 (1998).
- [143] T. Bourdel, *et al.*, *Physical Review Letters* **93**, 050401 (2004).
- [144] M. Romans, R. Duine, S. Sachdev, H. Stoof, *Physical Review Letters* **93**, 020405 (2004).
- [145] L. Radzihovsky, J. Park, P. Weichman, *Physical Review Letters* **92**, 160402 (2004).
- [146] Y.-W. Lee, Y.-L. Lee, *Physical Review B* **70**, 224506 (2004).
- [147] K. Xu, *et al.*, *Physical Review Letters* **91**, 210402 (2003).
- [148] G. E. Cragg, A. K. Kerman, *Physical Review Letters* **94**, 190402 (2005).
- [149] E. Timmermans, P. Tommasini, M. Hussein, A. Kerman, *Physics Reports* **315**, 199 (1999).
- [150] R. Duine, H. Stoof, *Physical Review A* **68**, 013602 (2003).
- [151] E. J. Mueller, G. Baym, *Physical Review A* **62**, 053605 (2000).
- [152] T. Mukaiyama, J. Abo-Shaeer, K. Xu, J. Chin, W. Ketterle, *Physical Review Letters* **92**, 180402 (2004).
- [153] D. Petrov, *Physical Review Letters* **93**, 143201 (2004).

- [154] E. Braaten, H.-W. Hammer, *Physical Review Letters* **87**, 160407 (2001).
- [155] D. Heinzen, R. Wynar, P. Drummond, K. Kheruntsyan, *Physical Review Letters* **84**, 5029 (2000).
- [156] S. K. Baur, S. Basu, E. J. Mueller, T. N. D. Silva, *arXiv:cond-mat/0901.2945* (2009).
- [157] M. Zwierlein, C. Schunck, A. Schirotzek, W. Ketterle, *Nature* **442**, 54 (2006).
- [158] N. Prokof'ev, B. Svistunov, *Physical Review B (Condensed Matter and Materials Physics)* **77**, 020408 (2008).
- [159] N. V. Prokof'ev, B. V. Svistunov, *Physical Review B (Condensed Matter and Materials Physics)* **77**, 125101 (2008).
- [160] J. Carlson, S.-Y. Chang, V. R. Pandharipande, K. E. Schmidt, *Physical Review Letters* **91**, 050401 (2003).
- [161] A. Perali, P. Pieri, G. Strinati, *Physical Review Letters* **93**, 100404 (2004).
- [162] P. Pieri, L. Pisani, G. Strinati, *Physical Review B* **70**, 094508 (2004).
- [163] B. R. Patton, The effect of fluctuations in superconducting alloys above the transition temperature, Ph.D. thesis, Cornell University (1971).
- [164] Q. Chen, Y. He, C.-C. Chien, K. Levin, *Physical Review B (Condensed Matter and Materials Physics)* **75**, 014521 (2007).
- [165] R. Combescot, A. Recati, C. Lobo, F. Chevy, *Physical Review Letters* **98**, 180402 (2007).
- [166] R. Combescot, S. Giraud, *Physical Review Letters* **101**, 050404 (2008).
- [167] H. Heiselberg, *Physical Review A* **63**, 043606 (2001).
- [168] G. M. Bruun, *Physical Review A* **70**, 053602 (2004).
- [169] T.-L. Ho, *Physical Review Letters* **92**, 090402 (2004).
- [170] G. E. Astrakharchik, J. Boronat, J. Casulleras, Giorgini, S., *Physical Review Letters* **93**, 200404 (2004).
- [171] S. Y. Chang, V. R. Pandharipande, J. Carlson, K. E. Schmidt, *Physical Review A* **70**, 043602 (2004).
- [172] J. Carlson, S. Reddy, *Physical Review Letters* **95**, 060401 (2005).
- [173] C. Lobo, A. Recati, S. Giorgini, S. Stringari, *Physical Review Letters* **97**, 200403 (2006).

- [174] T. N. D. Silva, E. J. Mueller, *Physical Review Letters* **97**, 070402 (2006).
- [175] M. Haque, H. T. C. Stoof, *Physical Review Letters* **98**, 260406 (2007).
- [176] Y. Ohashi, A. Griffin, *Physical Review A* **67**, 063612 (2003).
- [177] R. Casalbuoni, G. Nardulli, *Reviews of Modern Physics* **76**, 263 (2004).
- [178] M. Parish, F. Marchetti, A. Lamacraft, B. Simons, *Nature Physics* **3**, 124 (2007).
- [179] J. S. Dugdale, *Entropy And Its Physical Meaning* (CRC, 1996), second edn.
- [180] D. S. Petrov, C. Salomon, G. V. Shlyapnikov, *Physical Review Letters* **93**, 090404 (2004).
- [181] D. S. Petrov, C. Salomon, G. V. Shlyapnikov, *Physical Review A* **71**, 012708 (2005).
- [182] J. O. Andersen, *Reviews of Modern Physics* **76**, 599 (2004).
- [183] M. Bartenstein, *et al.*, *Physical Review Letters* **94**, 103201 (2005).
- [184] S. Gupta, *et al.*, *Science* **300**, 1723 (2003).
- [185] J. Goldwin, *et al.*, *Physical Review A* **70**, 021601 (2004).
- [186] J. Goldwin, S. Inouye, M. L. Olsen, D. S. Jin, *Physical Review A* **71**, 043408 (2005).
- [187] X. Du, Y. Zhang, J. Thomas, *arXiv:cond-mat/0903.1804* (2009).
- [188] D. S. Petrov, *Physical Review A* **67**, 010703 (2003).
- [189] C. A. Regal, M. Greiner, D. S. Jin, *Physical Review Letters* **92**, 083201 (2004).
- [190] S. Basu, E. J. Mueller, *Physical Review Letters* **101**, 060405 (2008).
- [191] P. F. Bernath, *Spectra of Atoms and Molecules* (Oxford University Press, USA, 2005).
- [192] M. Greiner, C. A. Regal, D. S. Jin, *Physical Review Letters* **94**, 070403 (2005).
- [193] C. H. Schunck, Y. Shin, A. Schirotzek, M. W. Zwierlein, W. Ketterle, *Science* **316**, 867 (2007).
- [194] J. Kinnunen, M. Rodriguez, P. Törma, *Science* **305**, 1131 (2004).
- [195] Y. Ohashi, A. Griffin, *Physical Review A* **72**, 013601 (2005).
- [196] P. Massignan, G. M. Bruun, H. T. C. Stoof, *Physical Review A (Atomic, Molecular, and Optical Physics)* **77**, 031601 (2008).
- [197] E. J. Mueller, *Physical Review A (Atomic, Molecular, and Optical Physics)* **78**, 045601 (2008).

- [198] M. A. Kasevich, E. Riis, S. Chu, R. G. DeVoe, *Physical Review Letters* **63**, 612 (1989).
- [199] M. Combescot, P. Nozières, *Journal de Physique* **32**, 913 (1971).
- [200] Y. He, Q. Chen, K. Levin, *Physical Review A* **72**, 011602 (2005).
- [201] Z. Yu, G. Baym, *Physical Review A* **73**, 063601 (2006).
- [202] G. Baym, C. J. Pethick, Z. Yu, M. W. Zwierlein, *Physical Review Letters* **99**, 190407 (2007).
- [203] M. Punk, W. Zwerger, *Physical Review Letters* **99**, 170404 (2007).
- [204] A. Perali, P. Pieri, G. C. Strinati, *Physical Review Letters* **100**, 010402 (2008).
- [205] C. Chin, P. S. Julienne, *Physical Review A* **71**, 012713 (2005).
- [206] R. B. Diener, R. Sensarma, M. Randeria, *Physical Review A* **77**, 023626 (2008).
- [207] C. J. Pethick, H. T. C. Stoof, *Physical Review A* **64**, 013618 (2001).
- [208] S. Chu, *Scientific American February*, 71 (1992).
- [209] J. Dalibard, S. Reynaud, C. Cohen-Tannoudji, *Journal of Physics B* **17**, 4577 (1984).
- [210] J. Dalibard, C. Cohen-Tannoudji, *Journal of the Optical Society of America B* **2**, 1707 (1985).
- [211] J. Reichel, *et al.*, *Physical Review Letters* **75**, 4575 (1995).
- [212] F. Bardou, J. Bouchaud, O. Emile, A. Aspect, C. Cohen-Tannoudji, *Physical Review Letters* **72**, 203 (1994).
- [213] C. Monroe, *et al.*, *Physical Review Letters* **75**, 4011 (1995).
- [214] D. Sesko, C. Fan, C. Wieman, *Journal of the Optical Society of America B* **5**, 1225 (1988).
- [215] P. Lett, R. Watts, C. Westbrook, W. Phillips, *Physical Review Letters* **61**, 169 (1988).
- [216] Y. Shevy, D. Weiss, P. Ungar, S. Chu, *Physical Review Letters* **62**, 1118 (1989).
- [217] J. Dalibard, C. Cohen-Tannoudji, *Journal of the Optical Society of America B* **6**, 2023 (1989).
- [218] M. Kasevich, S. Chu, *Physical Review Letters* **69**, 1741 (1992).
- [219] N. Davidson, H.-J. Lee, M. Kasevich, S. Chu, *Physical Review Letters* **72**, 3158 (1994).
- [220] A. Kerman, V. Vuletić, C. Chin, S. Chu, *Physical Review Letters* **84**, 439 (2000).

- [221] N. Newbury, C. Wieman, *American Journal of Physics* **64**, 18 (1996).
- [222] W. Ketterle, N. van Druten, *Evaporative cooling of trapped atoms* (Academic Press, San Diego, CA 92101, 1996), vol. 37 of *Advances in atomic, molecular, and optical physics*, p. 181.
- [223] A. Leanhardt, *et al.*, *Science* **301**, 1513 (2003).
- [224] V. Vuletić, S. Chu, *Physical Review Letters* **84**, 3787 (2000).
- [225] V. Vuletić, H. Chan, A. Black, *Physical Review A* **64**, 033405 (2001).
- [226] I. Bloch, M. Greiner, O. Mandel, T. Hänsch, T. Esslinger, *Physical Review A* **64**, 021402(R) (2001).
- [227] P. Chaikin, T. Lubensky, *Principles of condensed matter physics* (Cambridge University Press, 1995).
- [228] Y. Ohashi, A. Griffin, *Physical Review Letters* **89**, 130402 (2002).
- [229] M. Holland, S. J. J. M. F. Kokkelmans, M. L. Chiofalo, R. Walser, *Physical Review Letters* **87**, 120406 (2001).
- [230] M. L. Chiofalo, S. J. J. M. F. Kokkelmans, J. N. Milstein, M. J. Holland, *Physical Review Letters* **88**, 090402 (2002).
- [231] C. Chin, *arXiv:cond-mat/0506313* (2005).